Nuclear Science ISBN 92-64-02311-9

Speciation, Techniques and Facilities for Radioactive Materials at Synchrotron Light Sources

Workshop Proceedings
Berkeley, California, USA
14-16 September 2004

NEA No. 6046

NUCLEAR ENERGY AGENCY
ORGANISATION FOR ECONOMIC CO-OPERATION AND DEVELOPMENT

ORGANISATION FOR ECONOMIC CO-OPERATION AND DEVELOPMENT

The OECD is a unique forum where the governments of 30 democracies work together to address the economic, social and environmental challenges of globalisation. The OECD is also at the forefront of efforts to understand and to help governments respond to new developments and concerns, such as corporate governance, the information economy and the challenges of an ageing population. The Organisation provides a setting where governments can compare policy experiences, seek answers to common problems, identify good practice and work to co-ordinate domestic and international policies.

The OECD member countries are: Australia, Austria, Belgium, Canada, the Czech Republic, Denmark, Finland, France, Germany, Greece, Hungary, Iceland, Ireland, Italy, Japan, Korea, Luxembourg, Mexico, the Netherlands, New Zealand, Norway, Poland, Portugal, the Slovak Republic, Spain, Sweden, Switzerland, Turkey, the United Kingdom and the United States. The Commission of the European Communities takes part in the work of the OECD.

OECD Publishing disseminates widely the results of the Organisation's statistics gathering and research on economic, social and environmental issues, as well as the conventions, guidelines and standards agreed by its members.

* * *

This work is published on the responsibility of the Secretary-General of the OECD. The opinions expressed and arguments employed herein do not necessarily reflect the official views of the Organisation or of the governments of its member countries.

NUCLEAR ENERGY AGENCY

The OECD Nuclear Energy Agency (NEA) was established on 1st February 1958 under the name of the OEEC European Nuclear Energy Agency. It received its present designation on 20th April 1972, when Japan became its first non-European full member. NEA membership today consists of 28 OECD member countries: Australia, Austria, Belgium, Canada, the Czech Republic, Denmark, Finland, France, Germany, Greece, Hungary, Iceland, Ireland, Italy, Japan, Luxembourg, Mexico, the Netherlands, Norway, Portugal, Republic of Korea, the Slovak Republic, Spain, Sweden, Switzerland, Turkey, the United Kingdom and the United States. The Commission of the European Communities also takes part in the work of the Agency.

The mission of the NEA is:

- to assist its member countries in maintaining and further developing, through international co-operation, the scientific, technological and legal bases required for a safe, environmentally friendly and economical use of nuclear energy for peaceful purposes, as well as
- to provide authoritative assessments and to forge common understandings on key issues, as input to government decisions on nuclear energy policy and to broader OECD policy analyses in areas such as energy and sustainable development.

Specific areas of competence of the NEA include safety and regulation of nuclear activities, radioactive waste management, radiological protection, nuclear science, economic and technical analyses of the nuclear fuel cycle, nuclear law and liability, and public information. The NEA Data Bank provides nuclear data and computer program services for participating countries.

In these and related tasks, the NEA works in close collaboration with the International Atomic Energy Agency in Vienna, with which it has a Co-operation Agreement, as well as with other international organisations in the nuclear field.

FOREWORD

The third NEA Workshop on Speciation, Techniques and Facilities for Radioactive Materials at Synchrotron Light Sources (Actinide-XAS-2004) was held in Berkeley, California, USA on 14-16 September 2004. The workshop focused on the application of synchrotron radiation techniques to radionuclide/actinide sciences. More than fifty participants from eight countries discussed the progress made in this field since the second workshop in this series four years earlier (Actinide-XAS-2000). The following general topics were addressed:

- Radionuclides in the environment;
- Nuclear waste forms and remediation;
- Separations science;
- General actinide chemistry;
- Electronic and magnetic properties.

Thirty-one oral presentations, most of which were solicited talks, as well as thirteen papers presented in a poster session, contributed to the workshop programme which was organised according to the overall scientific themes of:

- Recent progress in synchrotron radiation techniques for investigating radionuclides;
- Applications and results in the fields of radionuclide/actinide chemistry and physics obtained by synchrotron radiation techniques and complementary methodologies;
- Present and future synchrotron radiation facilities for radionuclide investigations.

These proceedings contain all of the abstracts and some of the full papers presented at the workshop. The editors, Dr. Shuh and Dr. Reich, and anonymous referees reviewed the full papers. The organising committee wishes to thank these reviewers.

Actinide-XAS-2004 was hosted by the Lawrence Berkeley National Laboratory (LBNL). The sponsors of this meeting were LBNL, the US Department of Energy and the OECD Nuclear Energy Agency (NEA). The University of Mainz, the *Commissariat à l'énergie atomique* (CEA), the FZ-Rossendorf Research Centre and the Stanford Synchrotron Radiation Laboratory (SSRL) are also acknowledged for their contributions to Actinide-XAS-2004.

TABLE OF CONTENTS

* The abstracts of the papers unavailable in their entirety at the time of publication have been grouped here.

EXECUTIVE SUMMARY

It has been four years since the second Euroconference and NEA Workshop on Speciation, Techniques and Facilities for Radioactive Materials at Synchrotron Light Sources, Actinide-XAS-2000, took place at the European Synchrotron Radiation Facility in Grenoble. This second workshop followed two years after the inaugural workshop, Actinide-XAS-1998, at the same venue. Actinide-XAS-2004 is the first of the Actinide-XAS workshops to be held outside of Europe and is indicative of the truly international nature of synchrotron radiation, especially in the field of actinide/radionuclide chemistry and physics. The number and sophistication of synchrotron radiation experiments with radioactive materials continues to grow at a significant rate, usually limited only by availability of suitable beamline facilities, on-site health and safety support to safely conduct the research at the light sources, and lastly by the resources of the experimenters themselves. Oftentimes it is nearly impossible to obtain the information provided by synchrotron radiation investigations by other means for radioactive materials. The incessant drive to employ synchrotron radiation probes to materials containing actinides and radionuclides is testimony to the valuable molecular scale information that can be acquired utilising one of the suite of synchrotron radiation techniques. This is coupled to the ability to probe a wide range of complex sample materials and leads to applications throughout all of the scientific disciplines involved in actinide/radionuclide science. Synchrotron radiation techniques have also proven to be invaluable as a complementary technique to laboratory-based investigations of radionuclides and actinides. In fact, synchrotron radiation has now permeated the actinide/radionuclide chemistry and physics communities to such an extent that most large research groups employ synchrotron radiation efforts and/or collaborate with a synchrotron radiation group and/or beamline user facility. Synchrotron radiation experiments have made critical contributions over the past decade to the improved understanding of the fundamental knowledge of radionuclide speciation that is essential to predict behaviour in the environment; establish a rational basis for risk assessments for long-term nuclear waste storage; to develop new, more effective and cost efficient remediation methods; and finally for the development and implementation of new separations technologies. Similarly, synchrotron radiation techniques continue to provide a unique and evolving set of tools that have been exploited by the general chemistry and physics communities to explore the fundamental properties of the radionuclides/actinides.

The result of the continuing intense interest, the rapid evolution of the field and the extreme value to the scientific community of the previous two Actinide-XAS forums, led to Actinide-XAS-2004 which was held 14-16 September 2004 in Berkeley, California, USA. The workshop kept with tradition and focused on the progress and developments in the field since the last meeting, XAS-2000, as well as examining the potential of this field into the future. There were more than fifty participants, some of whom were veterans of the first two workshops, along with a host of new scientists, from five European countries, the USA, Japan and Russia. Actinide-XAS-2004 continued the tradition of emphasising active participation from graduate students, post-graduate fellows and newcomers to the field.

The scientific meeting was organised into a two-and-a-half-day workshop-style event based on the previously successful Actinide-XAS forums. There were 3 main workshop themes subdivided into 10 smaller scientifically-focused workshop sessions. More than 30 oral presentations were delivered, and there was an evening poster session combined with a reception featuring vintage California wines that at least rivalled those from the first two Actinide-XAS workshops.

The first day commenced with the session on co-ordination chemistry and separations, which was followed by sessions on solid state, emerging techniques and methods and VUV/soft X-ray science. C. Den Auwer opened the workshop by showing how the exotic properties of the actinides could be elucidated and understood by use of XAS. His focus was on actinide complexation with an emphasis on the nature of the cation site within two domains of structural complexity. The first simpler example examined small adducts with U and Np, and the second sought to use this basic knowledge to understand complexation of the same actinides in the serum transferrin complex. T. Yaita described the complementary use of synchrotron approaches, EXAFS and NEXAFS, to characterise the electronic structure and structural parameters of actinide complexes so that a rational design method could be employed for the development of improved separation ligands for trivalent actinides and lanthanides. W. Lukens then showed how the use of XAS led to the identification of a troublesome Tc complex present in some of the waste tanks at the Hanford Reservation. J. Wong gave the first solid state presentation explaining how high resolution inelastic X-ray scattering revealed the phonon dispersions in δ-Pu-Ga, a long-missing piece of critical information bearing on the properties of actinide metals. Along similar lines, E.J. Nelson related how XAS was employed to verify the local structure of several actinide metals and to characterise the first charge-density wave observed in α-U.

In the emerging techniques and methods session, L. Soderholm illustrated the utility of high-energy (> 80 keV) X-ray scattering (HES) for probing actinide metal-ion solution structure and described how new information from this technique was going to substantially improve the current understanding of actinide solution chemistry. The results from these studies demonstrate the complementary nature of HES to EXAFS; however, HES provides valuable full correlation information beyond the distance capable with EXAFS. A. Rossberg then outlined how Monte Carlo Transformation Analysis (MCTA) could be utilised in conjunction with EXAFS to characterise the individual structural parameters of several actinide species present simultaneously, as is frequently encountered in actinide samples of environmental relevance. The final presentation in this session was given by G.A. Waychunas, who portrayed how surface complexation studies using grazing-incidence XAS could benefit from the complementary use of Crystal Truncation Rod (CTR) analysis which can reveal the precise nature of a mineral surface in equilibrium with a reactive solution.

R. Denning shifted the focus of the workshop to lower energy in the VUV/soft X-ray session by narrating a *tour de force* of how polarised oxygen XAS and emission spectroscopies were used to gain an understanding of the covalent nature of the uranyl ion molecular orbitals in $Cs_2UO_2Cl_4$. Combining these results with existing results from higher energy polarised XAS, the complete experimental order of the important metal-centred valence orbitals was determined. A new concept of delocalisation versus spin-orbit splitting in the actinide 5f states was presented by J.G. Tobin who based the new picture on results combined from EELS collected with a TEM, XAS and theoretical simulations. K. Ivanov closed the session, and the first day of oral presentations at the workshop, describing how resonant X-ray emission spectroscopy was used to confirm earlier interpretations of the electronic structure of UO_3 obtained by photoelectron spectroscopy.

The second day started with a session on the chemistry of uranium. R. Reeder detailed how EXAFS and luminescence spectroscopy were used to characterise the mechanism of adsorption and co-precipitation of U(VI) on calcite. Multiple U(VI) species were found at the calcite surface under different surface loadings and a key tris-carbonato-like surface complex was identified. From this knowledge, the site selective incorporation of U(VI) on the $(10\bar{1}4)$ calcite surface can be explained. This was followed by J. Catalano describing the results of U speciation investigations of contaminated Hanford sediments and CTR studies of U sorption at iron mineral surfaces. C. Hennig explained the capabilities of a new spectro-electrochemical cell designed for use with actinides and showed the first results from U(IV)-U(VI) complexation systems with different ligands. S. Kelly related how XAS has

been used to address several pertinent topics in uranium chemistry including radioactive dating issues, U redox in differing geochemical environments, and specifically in calcium carbonate systems.

M. Denecke gave the first presentation in the microXAS session and described how this technique could address a complex environmental problem involving U and As on which regular XAS could not provide insight. This detailed study provided both elemental and species-specific correlations as part of the effort to characterise the operative mechanisms. M. Vespa presented the results of microXAS investigations of Ni and Co incorporated in hardened cement pastes and found that the behaviour of the two divalent metals ions is greatly different upon cement hydration.

The second solid state session began with a comprehensive talk given by S. Conradson on the local structure and speciation of oxy-hydroxides of the actinides. Similarities and differences between actinide species in a range of conditions were highlighted. Special attention was given to the aspects of collective behaviour leading to the unusual structures and chemical properties. E. Weschke presented the details and results of several resonant magnetic soft X-ray scattering experiments from lanthanides that have direct bearing on similar experiments that could be performed with actinides. The last talk in this session, given by M. Daniel, presented results substantiating that another mechanism leading to the anomalous specific heat must be present in ^{115}Ce as disorder could be ruled out and some initial XAS results from a ^{115}Pu compound.

The last session of the day was on actinide sorption. T. Reich gave the first talk relating the implications of the EXAFS results of U(VI) sorption on kaolinite. The results, which also included photoelectron spectrscopy data, showed that sorbed U species were monomeric in the absence of CO_2, whereas in the presence of atmospheric CO_2, the results supported the formation of ternary carbonato complexes at the surface. The final presentation of the second day was given by R.E. Wilson who discussed results from Np and Pu sorption experiments on oxide materials. He also delineated the experimental difficulties encountered when studying these systems with intense X-ray beams.

The final day of Actinide-XAS-2004 focused on the theme of present and future synchrotron facilities for radionuclide investigations, and was split into two sessions. The first session highlighted facilities' reports from new beamlines under construction and fully dedicated beamline facilities for research with radioactive materials. B. Sitaud presented the scientific motivation for the MARS beamline facility at SOLEIL, the technical capabilities of the beamline and safety features, as well as detailing the optical characteristics of the most recently planned beamline dedicated to the study of radioactive materials. R. Dähn described the experimental capabilities and anticipated scientific programme of the Micro-XAS Beamline dedicated to the Environmental Sciences at the SLS with respect to the use of radionuclides. H. Shiwaku detailed the recent results obtained with lanthanides/actinides at SPring-8 and presented the plans for new actinide beamline facilities. M. Denecke presented the capabilities, status and first commissioning measurements from the nearly-operational radiochemical beamline at ANKA.

The final session of the workshop was devoted to facilities updates from: ALS (D.K. Shuh) APS (L. Soderholm) NSLS (R. Reeder) and SSRL (J. Rogers). In conjunction with the facilities reports and updates, but after the conclusion of the workshop, several participants were given tours of the ALS at LBNL or were transported to SSRL which is located about sixty minutes from LBNL.

The three days of the Actinide-XAS-2004 were, as in the tradition of the previous Actinide-XAS workshops, a most stimulating scientific meeting with a unique atmosphere for the discussion of current and future science with radioactive materials at synchrotron radiation sources. The Actinide-XAS-2004 workshop was once again conducive to the interaction of young scientists with more experienced experts in the field, which is valuable to both. The increasing capabilities and opportunities for synchrotron radiation investigations of radionuclides were clearly evident. The number of recent results and their

impact in the field was impressive. The breadth of science and number of synchrotron techniques employed by researchers in this field continues to grow, as do the contributions to the understanding of the fundamental properties of radionuclides/actinides across several scientific disciplines.

A conclusion reached at the workshop was that the conference should continue to be convened in approximate two-year intervals, avoiding overlap with less specialised conferences that have a strong emphasis on synchrotron radiation. A more formal mechanism for determining the location of the next meeting was instituted using the current organising committee and all thought that rotation of the workshop location was in the best interest of the scientific community. It was decided that the next Actinide-XAS workshop, Actinide-XAS-2006, will be hosted by the Institute of Nuclear Waste Disposal (INE) at the Research Center Karlsruhe, Germany, the site of ANKA.

Co-ordination Chemistry and Separations

Chair: N.M. Edelstein

ACTINIDES IN MOLECULES: EXOTIC PROPERTIES PROBED BY X-RAY ABSORPTION SPECTROSCOPY

C. Den Auwer[1], S.D. Conradson[2], Ph. Guilbaud[1], D. Guillaumont[1], I. Llorens[1], Ph. Moisy[1], D.K. Shuh[3], E. Simoni[4], P.L. Solari[5], C. Vidaud[6]

[1]CEA Marcoule DEN/DRCP/SCPS, 30207 Bagnols-sur-Cèze Cedex, France

[2]Los Alamos National Laboratory, MST Division, Los Alamos, NM 87545, USA

[3]LBNL, Cyclotron Road, MS 70A-115070A University of California, Berkeley, CA 94720, USA

[4]Université Paris Sud, IPN, F-91405 Orsay Cedex, France

[5]ESRF, BM20, F-38043 Grenoble Cedex 9, France

[6]CEA Marcoule DSV/DIEP/SBTN, F-30207 Bagnols-sur-Cèze Cedex, France

Abstract

The chemistry of the actinide family is surprisingly rich. In order to better understand the affinity of specific chelates as in the case of ionic selective recognition or uptake by specific biomolecules, it is essential to better understand the intramolecular interactions. Although this has long been done for widely investigated transition metals, very few studies have been devoted to complexation mechanisms of radionuclides by active chelation sites. In this field, X-ray absorption spectroscopy has been extensively used as a structural and electronic metal cation probe. The two examples that are presented here explore two domains of structural complexity: on the one hand small hydrate and hydroxide adducts of uranyl and neptunyl have been probed in order to extract physical chemical information on the actinide cation; on the other hand large complex systems as uranyl uptake by serum transferrin have been investigated in order to characterise the cation binding site.

Introduction

The chemistry of the actinides is surprisingly rich because of their large atomic numbers (from Z = 90 for Th) and the relative availability of their valence electrons. For industrial, environmental and public health purposes, this chemistry has been the subject of considerable efforts since the 50s. Aqueous redox chemistry, ionic selective recognition, uptake by specific biomolecules or compartment of the geosphere are some of the major field of investigation. Nevertheless, general understanding of intramolecular interactions engaged in molecular actinide species, in other words physical chemical mechanisms that drive the affinity of chelating ligands for actinide cations still needs to be deepened. Although this process has long been undertaken for widely investigated transition metals, far fewer studies have been devoted to complexation mechanisms of actinides by specific chelation sites. As a result, the intramolecular interactions of actinide elements with smart chelates designed for co-ordination chemistry or bioinorganic chemistry are relatively unknown. For instance, the stability of the uranyl cation (UO_2^{2+} under atmospheric conditions and its ubiquity in the geosphere defines it as a major potential contaminant. Although many studies have been focussing on the complexation mechanisms of uranyl by organic or mineral systems as humic acids, clays or minerals [1-6], fewer have focussed on the sub-molecular level understanding of uptake by major active functional groups.

Both EXAFS and XANES regimes of X-ray absorption spectroscopy have been extensively used as a structural and electronic metal cation probe. Combination with more traditional spectroscopic techniques as spectrophotometry is an ideal tool for the understanding of the chelation mechanism. Our group has been involved in the structural and electronic investigation of molecular adducts of actinide elements from small clusters (less than 10 atoms) to large macromolecules (for instance transferrin, 80 kDa). In this paper, we review some of our work on uranium and neptunium in various molecular species. Uranium and neptunium at the stable oxidation state (VI) exhibit the well known bipyramidal polyhedron because of the transdioxo structure of U,Np(VI) O_2^{2+} .

Although significant structural information on the co-ordination polyhedron can be obtained from L_{III} absorption edge because of the importance of shape resonances, the very short core hole life time (about 7 eV for U) broadens the edge signal resulting in very little extractable electronic information. In most studies, a systematic investigation of the relative L_{III} edge position and width results in a qualitative comparison of the metal environment and its influence on the cation effective charge as well as the influence of the ligands [7]. Studies involving lower energy transitions are scarce because of the technical difficulties related to the handling of radioactive compounds with low energy photons [8–10]. However the multiple-edge approach has been proved fruitful for transition metals compounds (at both K and L edges) in order to extract properties such as electronic delocalisation or resulting magnetism. Figure 1 compares, as an example, the XANES spectra of uranyl nitrate ($UO_2(NO_3)_2 \cdot 6H_2O$) at various edges: L_{III} (corresponding to a $2p \rightarrow 6d$ dipolar transition tabulated at 17 166 eV), M_{III} (corresponding to a $3p \rightarrow 6d$ dipolar transition tabulated at 4 303 eV), M_V (corresponding to a $3d \rightarrow 5f$ dipolar transition tabulated at 3 552 eV) and $O_{IV,V}$ (corresponding to a $5d \rightarrow 5f$ dipolar transition tabulated at 102.8 and 94.2 eV, respectively). Although most of these edges can be partially or totally interpreted and simulated, some edge features still lack a spectroscopic interpretation.

In the following of this paper, the authors try to combine structural (EXAFS) and electronic (XANES) investigation of the actinide cations involved in molecular structures. In both cases, contributions from simulation codes and theoretical calculations are underlined as well as the

Figure 1. L_{III}, M_{III}, M_V, $O_{IV,V}$ X-ray absorption edges of uranium in uranyl nitrate

Note that for a better comparison the absorbance has not been normalised to the absorption edge

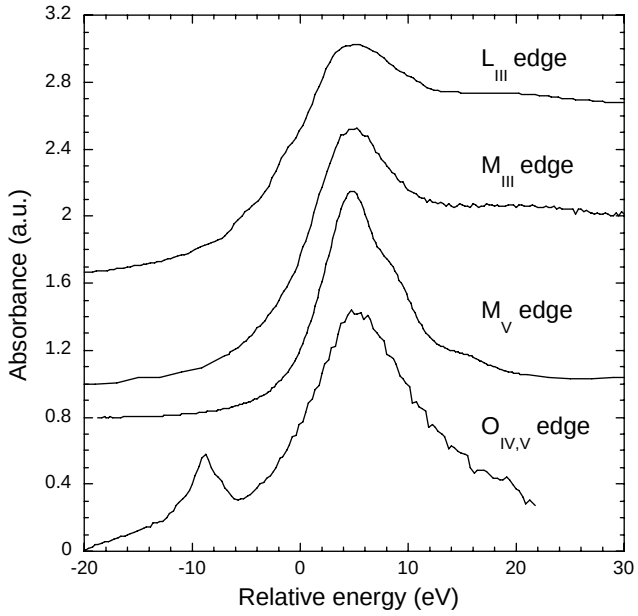

limitations of the models and techniques used to date. The paper describes in a first part the XANES investigation of uranyl and neptunyl hydrates and hydroxides in aqueous solution. In a second part, preliminary results on the chelation of uranyl by a metalloprotein (transferrin) is presented.

Uranyl and neptunyl hydrates in aqueous solution

The information included in the XANES spectrum has been used for long as a structural probe around the central actinide cation [11]. Conversely, the *ab initio* calculation of XANES spectra must be based on a model cluster that defines the best structural model of the compound under investigation. The optimisation of this model is at the starting point of obtaining reliable calculated spectra. Two components can be schematically considered in the definition of a model cluster. The first one, according to the multiple scattering approach, defines the adequate position of the scattering atoms in space and the inclusion of enough atoms in the calculation. The second component deals with the potential calculation of each scattering atom and the difficulty of dealing with a finite cluster size. The first component is in most cases easily optimised starting with an X-ray or neutron diffraction structure in the solid state, although light scattering atoms as hydrogen ones are usually difficult to localise by X-ray diffraction. However inclusion of hydrogen atoms as significant contributors has been discussed by Merkling, *et al*. and references herein [12] and has generally been found to be negligible. In the case of species in solution, the model cluster should represent, at best, an average of all the possible conformations. It can be based on assumptions driven from solid state structures or from molecular structures obtained by either theoretical chemistry or other spectroscopic techniques. Inclusion of dynamical effects in the solution or solvent effects derived from computer simulations have been reported mainly for transition metals [12] and such procedure for actinide cations is more seldom. The second component often depends on the structural approximations (inclusion of hydrogen atoms, cluster size and border effects, global charge bared by the molecule if needed) as well as the model of potential used for the calculation. Figure 2 presents the schematic skeleton of the uranyl and

Figure 2. Schematic skeletons of uranyl and neptunyl hydrates and hydroxides

Both actinides are at formal oxidation state VI

$[MO_2(H_2O)_5]^{2+}$ (M=U,Np)

$[UO_2(H_2O)_5]^{2+}$: 2 O @ 1.75 Å; 5 O @ 2.42 Å [15]

$[NpO_2(H_2O)_5]^{2+}$: 2 O @ 1.75 Å; 5 O @ 2.42 Å [16]

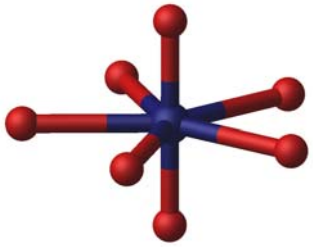

$[MO_2(OH)_4]^{2-}$ (M=Np)

$[NpO_2(OH)_4]^{2-}$: 2 O @ 1.82 Å; 4 O @ 2.21 Å [17]

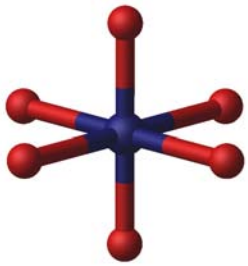

neptunyl hydrates and hydroxides in aqueous solution. In order to account for the solvent part beyond the first co-ordination sphere, an approach combining MD calculations and XANES calculations with Feff8.2 code [13] has been performed [14] for these systems in aqueous solution, leading to a sampling for both the first sphere hydrogen atoms and the surrounding water molecules around the actinyl molecular skeleton (the term "molecular skeleton" $(MO_2)O_5$ or $(MO_2)O_4$ (M = U, Np) referring to the first co-ordination sphere structure excluding the hydrogen atoms). Note that in the following of the text the so-called first co-ordination sphere includes the two axial oxygen atoms and the four or five equatorial molecules (H_2O, OH^-) that are directly linked to the metallic cation. The so-called second co-ordination sphere includes the water molecules directly hydrogen bonded to the first co-ordination sphere.

Since the evaluation of first sphere hydrogen atoms and solvent structure effects for the two cations is essential, simulations have been performed with frozen and optimised skeletons allowing either first sphere (water or hydroxide) molecules and all further water molecules to move during the simulation or only first sphere (water or hydroxide) hydrogen atoms and all further water molecules to move. Six molecular structures have been taken as instantaneous snapshots at regular time intervals during the MD simulations. These structures include the cation, its first co-ordination sphere and all the water molecules having at least one atom included within 6 Å around the cation. XANES calculations with inclusion of various scatters beyond the molecular skeleton show that scattering contributions beyond the first co-ordination sphere as well as scattering contributions from the hydrogen atoms of the first co-ordination sphere are negligible. However, inclusion of at least two co-ordination spheres seems necessary to obtain a set of reliable atomic potentials for the molecular skeleton. Figure 3(a) compares two sets of calculations based on the frozen and optimised skeleton options. With the optimised skeleton, the variations of the white line intensity and position are, as expected, far larger. It corroborates the general assessment about the importance of the first co-ordination sphere in the build up of the edge spectrum. The optimised skeleton option creates a series of snapshots with significant distortion of the first co-ordination spheres between each snapshot. The net result is a small dumping of the average white line intensity with respect to the frozen skeleton option. This difference should become negligible as a larger number of snapshots are taken into account in the calculation of the average. Nevertheless, their similarity shows that the overall influence of the method used for the computer simulations (frozen skeleton) is negligible when enough conformations (here six snapshots) are taken into account.

Figure 3(b) shows the L_{III} edges of neptunyl in both acidic ($[NpO_2(H_2O)_5]^{2+}$) and basic ($[NpO_2(OH)_4]^{2-}$) aqueous solutions [14]. The structural distortion of the molecular skeleton from acidic to basic media corresponds to an elongation of 0.07 Å of the axial distances and a contraction of

Figure 3

(a) Comparison between the edge calculations based on MD with frozen skeleton and optimised skeleton

Frozen: — ---- 50 ps; — — — 75 ps; -------- 100 ps; - - - - 125 ps; ——— 150 ps; — - —- — 175 ps
Optimised: — ---- 50ps; — — — 75ps; -------- 100ps; ——— 150ps; — - —- — 175ps

For both cases, the means (dashes with squares = frozen; plain line = optimised) are also compared

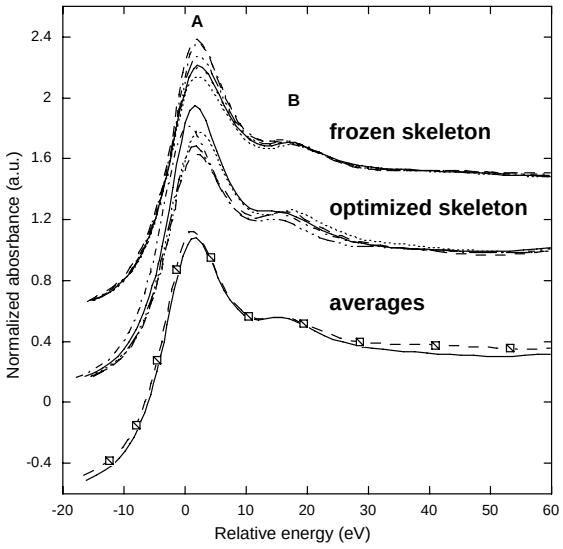

(b) Experimental (dots) and calculated (plain line) L_{III} edge spectra of $[NpO_2(H_2O)_5]^{2+}$ and $[NpO_2(OH)_4]^{2-}$

Both calculations are based on one MD snapshot (100 ps)

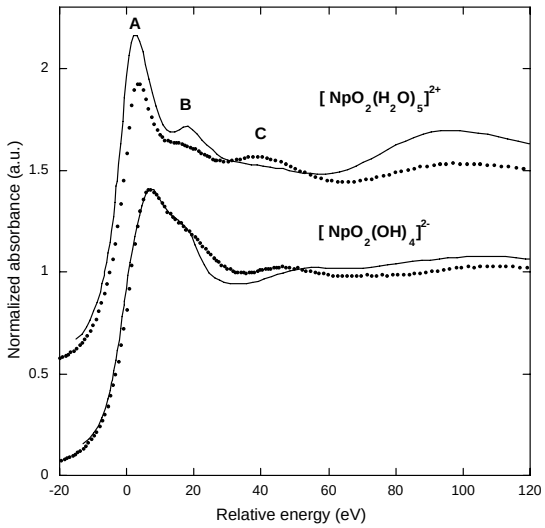

0.21 Å of the equatorial distances [17]. Comparison of the corresponding experimental L_{III} edges shows that this deformation leads to dramatic changes in the edge spectrum: strong differences in the intensity of A, shifts of B and C in the spectrum of $[NpO_2(H_2O)_5]^{2+}$ compared to $[NpO_2(OH)_4]^{2-}$. These differences are well reproduced with both calculations using a cluster obtained from one MD snapshot (after 100 ps). Note that the same Feff8.2 parameters have been used here as for the calculation of the spectrum of $[UO_2(H_2O)_5]^{2+}$.

Uranyl uptake by serumtransferrin

Recently, our group has undertaken the investigation of uranyl, neptunium(IV) and plutonium(IV) uptake by transferrin (Tf) [18-20], a metalloproteins that is responsible in advanced eukaryote cell of 15-20% (with haemosiderin) of iron transport. Transferrin is a regulator of Fe(III) carriage in blood [21]. It is a glycoprotein of 670 amino acids (81 000 Da) with a tertiary structure made of two equivalent lobes (C and N) with one possible complexation site each (Figure 4). The iron metal binding site is made of a distorted octahedron with two tyrosyl phenolates, one histidyl imidazole and one aspartate carboxyl. The requirement of a synergistic anion carbonate has been confirmed. This anion could co-ordinate to iron in a bidentate mode. It can bind a wide variety of d-block transition metals, as well as actinides and lanthanides. For instance Taylor, *et al.* have suggested that the protein is able to stabilise the tetravalent state and form stable M^{4+}-Tf complexes [22]. This is why transferrin contamination by actinide cations is a critical issue of nuclear human toxicology. Pu(IV) as well as most of the transition metal cations reported to be complexed by transferrin are assumed to be located in the iron site [23].

Figure 4. Structure of the serum human transferrin, N terminal lobe (PDB 1B3E) [24]

Uranyl is the ubiquitous stable form of uranium at oxidation VI. Its uptake by serum apotransferrin has been shown by spectrophotometric studies [25]. In Figures 5(a) and 5(b), both XANES and EXAFS (Fourier transform, R + Φ) spectra of aqueous uranyl and uranyl-Tf complex are presented. Given the energy resolution of the uranium L_{III} edge, there is no significant difference between the aqua form of uranyl ($[UO_2(H_2O)_5]^{2+}$) and the chelated form by apotransferrin, indicating that the oxo ion is not significantly affected by the protein chelation. On the other hand the Fourier transform of the EXAFS spectra exhibit significant differences in the equatorial shell. A two-shell fit suggests that the two axial oxygen atoms are positioned at 1.77 Å and five oxygen,nitrogen atoms are located in the equatorial plane at 2.37 Å. This corresponds to a lengthening of 0.05 Å compared to the aqueous form

Simulations with molecular mechanics are presently being carried out in order to better define the possible uranyl co-ordination site in transferrin. A putative co-ordination mode within the iron bonding site is currently being tested [26]. The localisation of uranyl in this site would be in agreement with the short equatorial distances given the strong base character of the possible chelation groups: tyrosine, aspartate (and to a less extent histidine). Note also that the presence of a synergistic anion (here carbonate) is mandatory for lobe complexation.

Figure 5

(a) L_{III} edge XANES spectra of uranium in aqueous (perchlorate) solution and chelated by apotransferrin at physiological pH

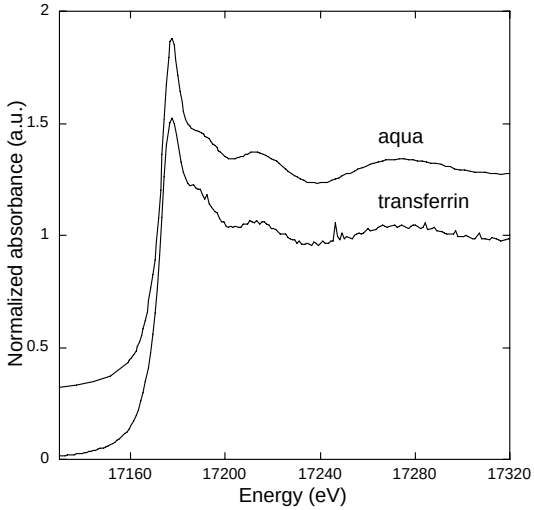

(b) Fourier transform of the L_{III} edge EXAFS spectra of uranium in aqueous (perchlorate) solution and chelated by apotransferrin at physiological pH

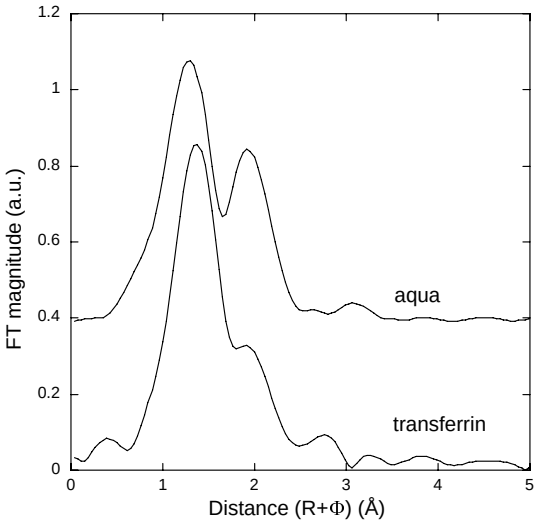

Conclusion

Although the L_{III} X-ray absorption edges of actinyl compounds have been intensively investigated, comprehensive understanding of the underlying electronic phenomena is still partial. The two examples presented in this paper explore two domains of structural complexity: on one hand small adducts (less that 10 atoms) have been investigated in order to extract physical chemical information on the actinide cation; on the other hand large complex systems (more than 100 atoms) for which the determination of the co-ordination site is the first step towards the physical chemical properties of the actinide cation. From that point of view, combined XAS data in a multi edge analysis with theoretical chemistry codes as molecular dynamics or quantum chemistry is essential.

Experimental

Data acquisition was carried out at ESRF (Grenoble, France) on BM20, SSRL (Stanford, USA) on BL11-2 (J. Bargar and J. Rogers) and ALS (Berkeley, USA) on BL8.0.1. Data extraction was done with EXAFS98 code [27] and data fitting with the Artemis code [28].

Sample preparation is described in the referenced articles.

Acknowledgements

This research was mainly carried out at the European Synchrotron Radiation Facility, at the Stanford Synchrotron Radiation Laboratory (a national user facility operated by Stanford University on behalf of the US Department of Energy, Office of Basic Energy Sciences) and at the Advanced Light Source (a national user facility which and a division of the Lawrence Berkeley National Laboratory). The authors are particularly grateful to the beamline scientists and health physicists at SSRL supported by the Seaborg Institute at LANL.

This work has been financially supported by CEA/DEN (France) PRACTIS-PARIS (France) the Nuclear-Toxicology programme CEA/DEN/MRTRA (France) and by DOE OBES Division of Chemical Sciences under Contract W-7405 (USA).

REFERENCES

[1] Günther, A., G. Bernhard, G. Geipel, T. Reich, A. Rossberg, H. Nitsche, *Radiochim. Acta*, 91, 319 (2003).

[2] Hennig, C., P.J. Panak, T. Reich, A. Roßberg, J. Raff, S. Selenska-Pobell, W. Matz, J.J. Bucher, G. Bernhard, H. Nitsche, *Radiochim. Acta*, 89, 625 (2001).

[3] Denecke, M.A., S. Pompe, T. Reich, H. Moll, M. Bubner, K.H. Heise, R. Nicolai, H. Nitsche, *Radiochim. Acta*, 79, 151 (1997).

[4] Denecke, M.A., J. Rothe, K. Dardenne, P. Lindqvist-Reis, *Phys. Chem. Chem. Phys.*, 5, 939 (2003).

[5] Walter, M., T. Arnold, T. Reich, G. Bernhard, *Environ. Sci. Technol*., 37, 2898 (2003).

[6] Merroun, M., C. Hennig, A. Rossberg, T. Reich, S. Selenska-Pobell, *Radiochim. Acta*, 91, 583 (2003).

[7] Conradson, S.D., *et al., Inorg. Chem.*, 43, 116 (2004).

[8] Kalkowski, G., G. Kaindl, W.D. Brewer, W. Krone, *Phys. Rev. B* 35, 2667 (1987).

[9] Petiau, J., G. Calas, D. Petitmaire, A. Bianconi, M. Benfatto, A. Marcelli, *Phys. Rev. B* 34, 7350 (1986).

[10] Denning, R.G., J.C. Green, T.E. Hutchings, C. Dallera, A. Tagliaferri, K. Giarda, N.B. Brookes, L. Braicovich, *J. Chem. Phys*., 117, 8008 (2002).

[11] Ankudinov, A.L., S.D. Conradson, J. Mustre de Leon, J.J. Rehr, *Phys. Rev. B* 57, 7518 (1998).

[12] Merkling, P.J., A. Muñoz-Páez and E. Sánchez Marcos, *J. Am. Chem. Soc*., 124, 10911 (2002).

[13] Conradson, S.D., *Appl. Spectroscopy*, 52, 252 (1998).

[14] Den Auwer, C., D. Guillaumont, P. Guilbaud, S.D. Conradson, J.J. Rehr, A. Ankudinov, E. Simoni, *New J. Chem.*, 28, 929 (2004).

[15] Den Auwer, C., R. Drot, E. Simoni, S.D. Conradson, M. Gailhanou and J. Mustre de Leon, *New J. Chem.*, 27, 648 (2003).

[16] Reich, T., G. Bernhard, G. Geipel, H. Funke, C. Hennig, A. Rossberg, W. Matz, N. Schell and H. Nitsche, *Radiochimica Acta*, 88, 633 (2000).

[17] Williams, C.W., J.-P. Blaudeau, J.C. Sullivan, M.R. Antonio, B. Bursten and L. Soderholm, *J. Am. Chem. Soc*., 123, 4346 (2001).

[18] Durbin, P.W., B. Kullgren, J. Xu, K.N. Raymond, P.G. Allen, J.J. Bucher, N.M. Edelstein, D.K Shuh, *Health Phys.*, 75, 34 (1998).

[19] Neu, M.P., C.E. Ruggiero, A.J. Francis, in *Advances in Plutonium Chemistry 1967-2000* [Darleane Hoffman, American Nuclear Society, La Grange Park, Il, (2002)] and D.M. Taylor, in *Handbook of Heavy Metals in the Environment* [B. Sarkar, New York, 4, (2002)].

[20] Sun, H., H. Li, P.J. Sadler, *Chem. Rev.*, 99, 2817 (1999).

[21] See for instance P. Aisen, *Metal Ions Biol. Sys.*, 35, 585 (1998).

[22] Taylor, D.M., *J. Alloys Comp.*, 271, 6 (1998).

[23] Harris, W.R. in *Structure and Bonding* (Springer Verlag, Heidelberg), 92, 121 (1998).

[24] Bewley, M.C., B.M. Tam, J. Grewal, S. He, S. Shewry, M.E. Murphy, A.B. Mason, R.C. Woodworth, E.N. Baker, *Biochemistry*, 38, 2535 (1999).

[25] Vidaud, C., E. Quemeneur, unpublished data.

[26] Llorens, I., C. Den Auwer, Ph. Moisy, E. Ansoborlo, C. Vidaud, H. Funke, *Chem. Bio. Chem.*, submitted.

[27] Michalowicz, A., *J. Phys. IV C2*, 7, 235 (1997).

[28] Newville, M., *J. Synchrotron Rad.* 8, 322 (2001).

VUV and Soft X-ray Science

Chair: T. Reich

X-RAY ABSORPTION AND PHOTOELECTRON SPECTROSCOPY OF Pu AT THE ADVANCED LIGHT SOURCE: SAMPLE QUALITY ANALYSIS

J.G. Tobin[1], **B. Chung**[1], **J. Terry**[2,+], **R.K. Schulze**[2], **J.D. Farr**[2], **K. Heinzelman**[3], **E. Rotenberg**[3], **D.K. Shuh**[3]
[1]Lawrence Livermore National Laboratory, Livermore CA, USA
[2]Los Alamos National Laboratory, Los Alamos NM, USA
[3]Lawrence Berkeley National Laboratory, Berkeley, CA, USA
[+]Present address: IIT, Chicago, IL, USA

Abstract

X-ray absorption spectroscopy (XAS) and photoelectron spectroscopy (PES) have been performed upon highly radioactive samples, particularly plutonium, at the Advanced Light Source in Berkeley, CA, USA. First results from alpha and delta plutonium are reported as well as a detailed analysis of sample quality.

Introduction

Photoelectron spectroscopy and X-ray absorption have been used to investigate the electronic structure of alpha and delta Pu [1-3]. It is generally believed that alpha is more free-electronlike and delta is possibly a correlated electronic system, although the details of this remain clouded [4-10]. One result of our first studies is that we believe that minimisation of sample oxidation is a key to successful experimentation. Here, we will discuss in detail the analysis of the quality of the Pu samples used in the synchrotron radiation based studies at the Advanced Light Source in Berkeley, CA.

Experimental

The first experiments were performed at the Spectromicroscopy Facility (Beamline 7.0) at the Advanced Light Source in Berkeley, CA [11]. The Pu samples were taken from a specially purified batch of Pu metal. The plutonium was zone refined and vacuum distilled while magnetically levitated [12]. The product of the purification process was α-Pu containing a total of 170 ppm impurities. A portion of the refined metal was alloyed with gallium to form the δ-phase (fcc symmetry). The sample surfaces were prepared by repeated room temperature, sputter-annealing cycles to minimise the amount of oxygen and other impurities dissolved in the sample or at grain boundaries, in a specially designed chamber attached to the sample introduction and analysis systems on Beamline 7.0. The transfer, preparation and analysis chambers ensured that the Pu metal samples were always under very good vacuum, in order to minimise any surface contaminants that could adversely affect the soft X-ray measurements.

Sample quality analysis

The issue of sample quality revolves primarily around the level of surface oxidation. Oxygen has three levels: O 1s (BE = -529 eV), O 2s (BE = -23 eV) and O 2p (BE = -5 eV). Each level has cross-sections which can change dramatically with photon energy, as can the cross-sections of the Pu levels.

The cross-section calculations of Yeh and Lindau [13] for oxygen and plutonium referenced below. Unfortunately, their respective calculations do *not* include the effects of the 5d-5f resonance in Pu [1]. Experimental results will be presented which demonstrate the tremendous intensity variations in the regime of the resonance, as well as the Cooper Minimum. To avoid the problem of quantification in this regime, most of the quantitative analysis will focus on other, more well-behaved, photon energy regimes.

To facilitate the analysis, several key questions are posed, listed at the top of each subsection.

Is it possible to distinguish between the phases in situ in the photoemission experiments? YES.

We see a number of spectroscopic differences between the alpha and delta phases, particularly with techniques or regimes that favour bulk sensitivity. Using total electron yield in X-ray absorption (Figure 1, left) we observe a distinct shift between the alpha and delta phases. We will return to the significance of this shift below. The mean free path for total yield has been estimated to be on the order of 22 angstroms [14]. Core level photoemission also provides a mechanism for distinguishing the alpha and delta phases. In Figure 1 (right) there are distinct differences between the alpha and delta 4f line-shapes, in agreement with a substantial body of previous work by Naegele, *et al*. [15], Gouder, *et al*. [16] and others [17–19]. Again, because of the fairly high kinetic energy of the electrons (about 400 eV) there is a fair amount of bulk sensitivity here. Because our samples of Pu are polycrystalline, low-energy electron diffraction (LEED) is not an option.

Figure 1. X-ray absorption ($O_{4,5}$, 5d -> 5f transition, left) and Pu 4f core level (right) spectroscopy

In the XAS figure, the red is data from α-Pu and the black is from δ-Pu. The PES spectra were collected with a photon energy of 850 eV. Note that two large components are visible in each spectrum, a sharp feature at low binding energy and a broad feature at higher binding energy.

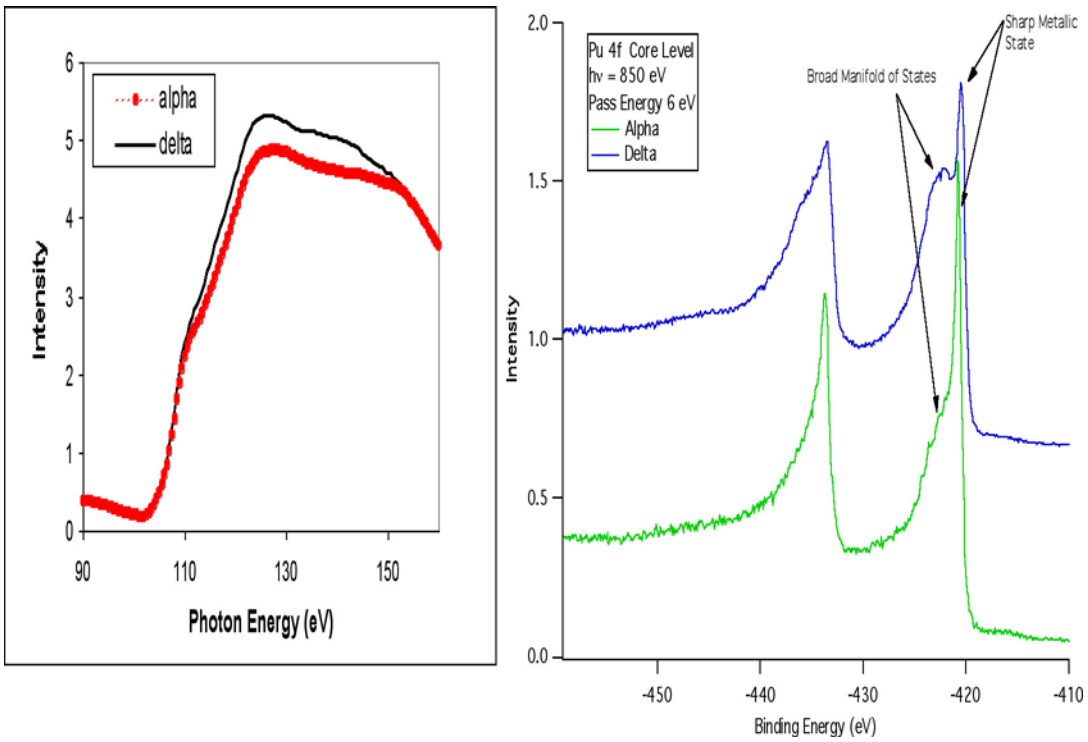

Can the in situ identifications be linked directly to diffraction based identifications of the phases? YES.

Experiments have also been performed in a high energy electron microscope [2]. Here, a variant of high energy electron energy loss spectroscopy (HE-EELS) is utilised. Under the conditions of the microscope (a primary beam energy of 300 000 eV) the electron energy loss is essentially operating in the electric dipole limit and therefore very much like X-ray absorption. Here again, that shift between the alpha and delta phases can be seen (Figure 2, left). It is also obvious that the HE-EELS of Pu is unlike that of either U or Th. The shifts seen in HE-EELS and synchrotron radiation X-ray absorption allows to link the samples in the two experiments directly. This in turn allows to link to the micro-diffraction results, which are shown in Figure 2. The micrograph shows different regions of alpha and delta in a mixed phase polycrystalline sample. The diffraction results for the alpha and delta phases show that they have the correct symmetry and allow easy differentiation of the two phases. Thus, despite the fact that the Pu samples are polycrystalline, micro-diffractive identification and phase specific interrogation of the individual phases are possible. Moreover, the HE-EELS and X-ray absorption results allow to directly link the core level spectra to specific diffraction patterns and phases.

Figure 2. Electron energy loss spectroscopy (EELS, left) and electron diffraction (right) of alpha and delta Pu [2]

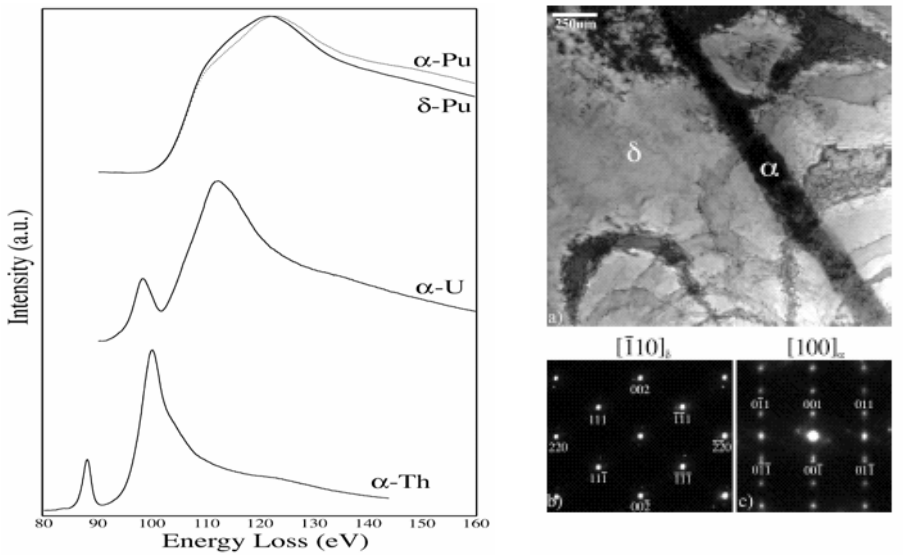

How do our 4f core level spectra compare to those of known oxides?

The 4f core level spectra of Courteix, *et al*. [20] for a series of oxidation levels and using MgKα excitation (hν = 1 254 eV) are displayed in Figure 3. Similar core level spectra can be found in Ref. [21]. Spectrum *a* is for nominally clean delta –Pu. Spectra *b*, *c* and *d* are for increasing oxidation levels, with spectrum *d* corresponding to PuO_2. It is immediately obvious that the 4f spectra from our delta samples are qualitatively different than the spectra from the PuO_2. Thus we can establish the bound that our Pu samples are not remotely similar to PuO_2. Courteix, *et al*. also conveniently supply O 1s spectra, calibrated relative to the Pu 4f peaks. We shall return to this later, but looking ahead, we will see that the O 1s intensities in our spectra at hν = 1 250 eV are very much smaller.

Figure 3. Pu 4f and O 1s core level spectra for a series of oxidation levels and using MgKα excitation (hν = 1254 eV) [20]

Spectrum a is for nominally clean delta – Pu. Spectra b,c and d are for increasing oxidation levels, with spectrum d corresponding to PuO_2

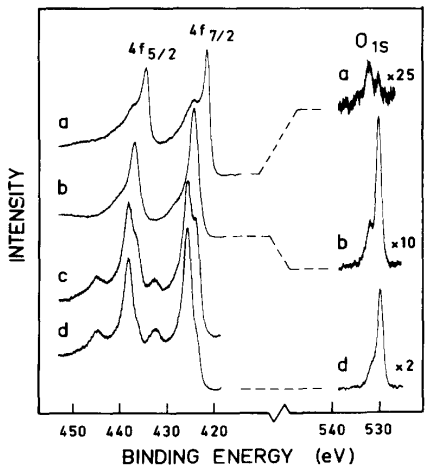

How do our valence band spectra at a photon energy corresponding to a MgK α source (1 254 eV) compare to those of known oxides?

Obviously, our spectrum in Figure 4(a) is very similar to that of Baptist, *et al*. in Figure 4(c) and very dissimilar to that of Courteix, *et al*., in Figure 4(b). Note especially the absence of the O 2p and O 2s peaks from our spectra. Again, this is an indication that the oxidation of our samples is fairly limited.

Figure 4. PES valence band spectrum, taken with hν = 1 254 eV photons

For reference, here are some pertinent peak energies:
Pu 5f BE = 0 eV, Pu $6p_{3/2}$ BE = 16 eV, Pu $6p_{1/2}$ BE = 29 eV, O 2p BE = 5 eV and O 2s BE = 23 eV

(a) Author results

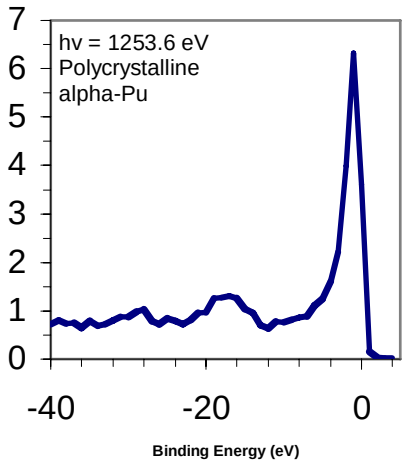

(b) *Courteix, et al. [20]*

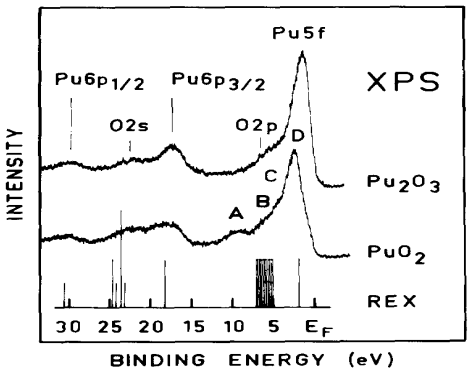

(c) *Baptist, et al. [17]*

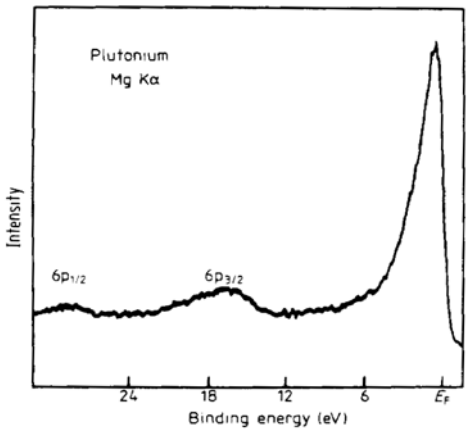

What is the result of a quantitative analysis of the O 1s intensity?

First, it is immediately obvious that we have only a very small O 1s intensity versus that of the Pu-oxides in Figure 3. In our hν = 1 250 eV spectrum, the O 1s peak can not be seen above the noise. In the PuO_2 spectrum in Figure 3, the O 1s peak is approximately 1/3 the height of the Pu 4f peaks. This suggests that we have orders of magnitude less oxygen that the PuO_2 sample. To enhance the O 1s cross-section, we also performed the same measurements at hν = 860 eV. At this photon energy,

Figure 5. Wide scan PES of δ-Pu, including a blow-up of the oxygen 1s region

The oxygen peak (binding energy of -530 eV) is much more easily observed at 860 eV than at 1 250 eV

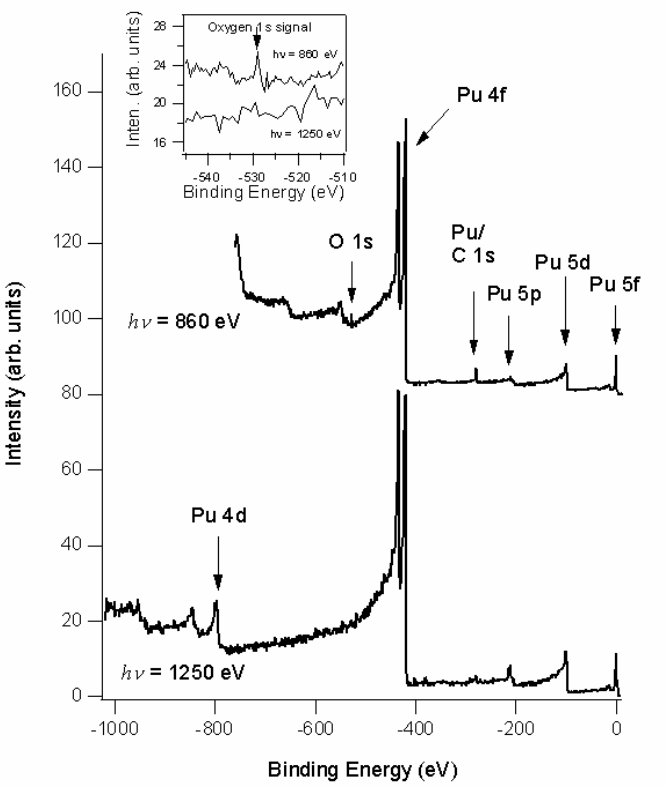

we can see the O 1s (BE = -530 eV). By measuring the relative intensities of the O 1s and Pu 4f peaks and then correcting for their cross-sections [13] we can come up with an O/Pu concentration ratio of 0.06 ± 0.06 or $6\% \pm 6\%$. The weakness of the O 1s feature and uncertainties in the cross-section calculations cause the large error bar here.

It should be noted that measurements based upon using the O 1s peak are highly preferable to those using the peaks of the O 2p and O 2s states. This is because 1) the 2p and 2s states are close enough to the valence regime to be affected by changes in bonding and 2) the normalisation for the measurements in this regime is usually the valence band or 5f peaks, the intensity of which may also change with chemical state, emission angle, photon energy, kinetic energy, etc. Finally, although in the region labelled as C 1s, the peak at BE = 280 eV is actually Pu-derived [17].

Why does the O 2p look so big in the spectra at the Cooper Minimum and the 5f anti-resonance?

Obviously, we have some oxygen on the Pu samples. By going to where the Pu 5f cross-section is very small, it is possible for us to accentuate the oxygen-based features such as the O 2p peak at BE = -6 eV. Two places where the 5f cross-section is the smallest are: the anti-resonance at hν = 102 eV (see Figure 7) and the Cooper Minimum at hν = 220 eV [13]. At the Cooper Minimum, the Pu 5f cross-section is about 1/500 of its maximum value.

Figure 6. Valence band PES of alpha and delta Pu at hν = 220 eV

This is at the Cooper Minimum. The O 2p is at BE = -6eV, with a secondary peak at BE = -10 eV. The Pu 5f states are near BE = -1 eV and the Fermi Level (0 eV).

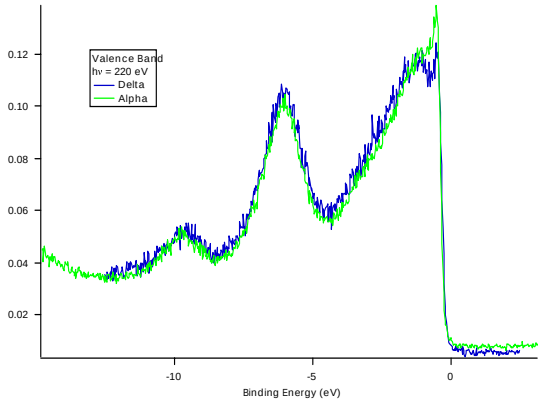

Figure 7. Resonant PES of Pu

Resonant Photoemission or ResPes is a type of spectroscopic interrogation of the valence electronic structure. A large data set is shown here, for single crystallite delta. The plots show the intensity variations (z axis) versus the binding energy of the states (the negative numbers in eV; zero is the Fermi energy) and photon energy (between 90 eV and 160 eV). Note low intensity at the anti-resonance at hν = 102 eV.

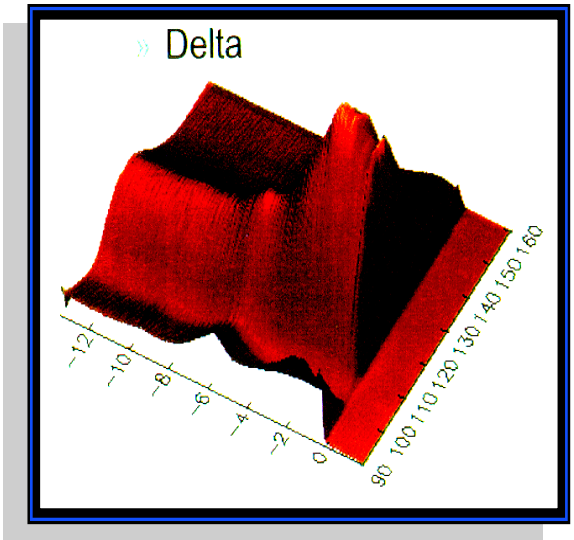

Why are the valence band spectra for the alpha and delta samples so similar? Shouldn't they be more different?

Havela, Gouder, Wastin, and Rebizant [19] have shown that a delta-like reconstruction forms on alpha Pu if the temperature is room temperature or above. Our gentle annealings (T about 373 K) were sufficient to cause the reconstruction on our alpha samples.

Figure 8. PES valence band spectra of alpha and delta Pu at hν = 125 eV

Note the small O 2p peak BE = 5.5 eV. Again, the Pu 5f states are near BE = -1 eV and the Fermi Level (0 eV)

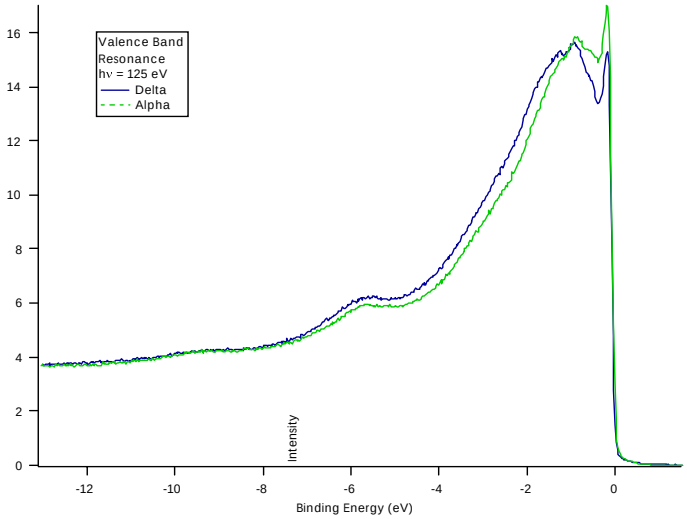

Figure 9. PES valence band spectra

Taken from Havela, et al. [19]. The photon energy was 40.8 eV (He II).

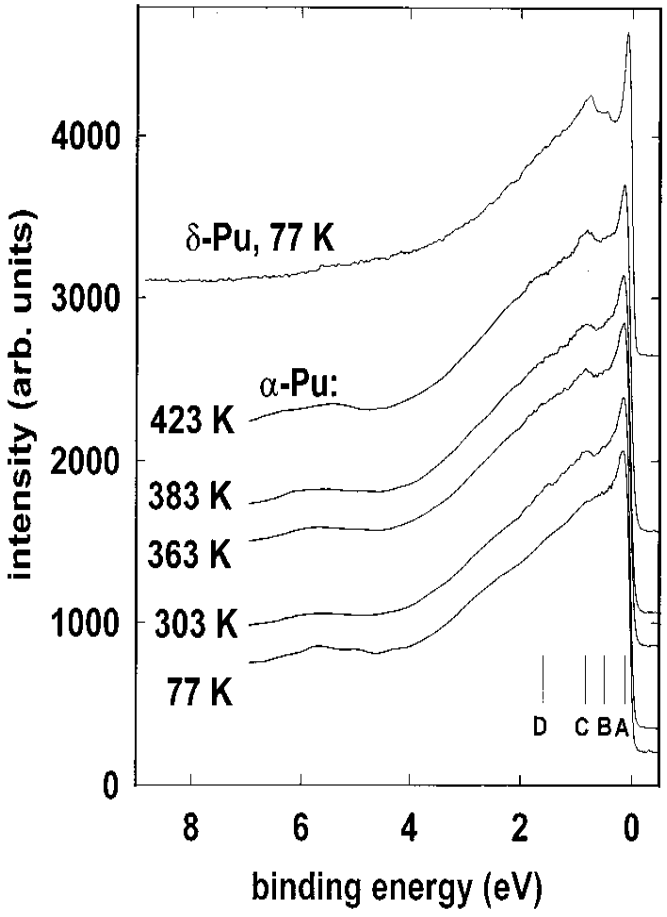

Are there cleaner Pu samples than we produced?

Yes, both the Havela, *et al*. results in Figure 9 and the Butterfield, *et al*. [22] results in Figure 10 below are cleaner. Our samples are not quite as clean as theirs, but we are in the right "ball-park".

Figure 10. PES of the valence band region of Pu

Taken from Butterfield, et al. [22]. The O 2p peak is at BE = -5.5 eV and the Pu 5f states are near BE = -1 eV and the Fermi Level (0 eV).

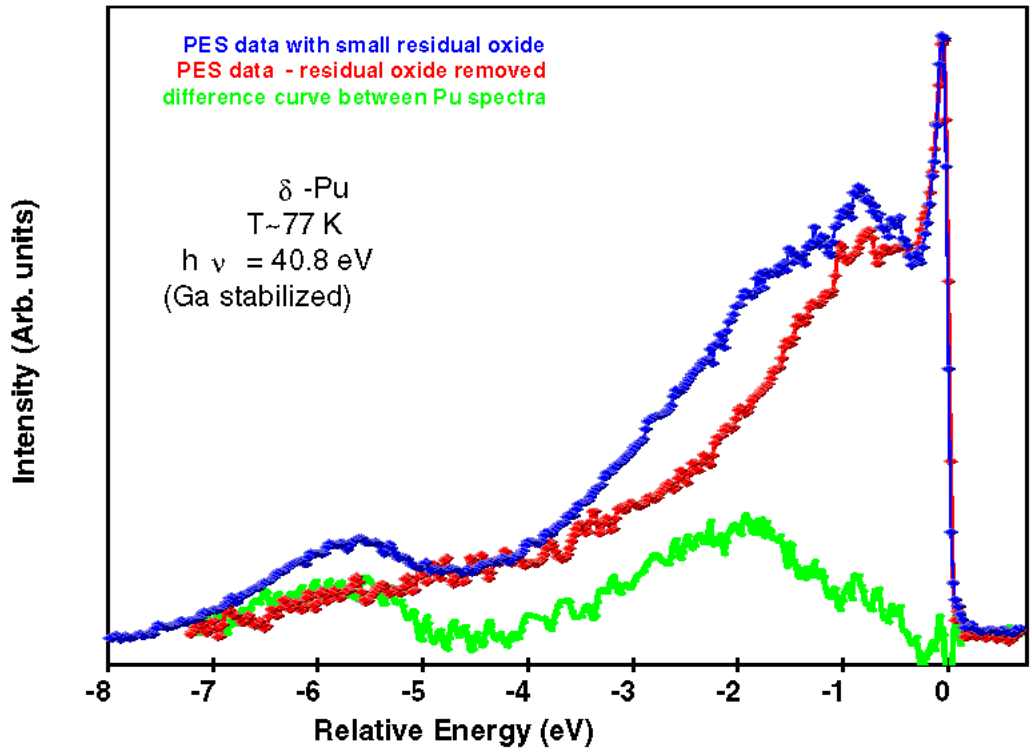

Conclusions

It is possible to distinguish the different phases of Pu (alpha and delta) in our experiments. While some surface oxygen contamination is present, the level is fairly low and roughly comparable to the cleanest samples reported to date.

Acknowledgements

This work was performed under the auspices of the US Department of Energy by the University of California Lawrence Livermore National Laboratory under contract No. W-7405-Eng-48. This work was also performed in conjunction with LANL (Contract No. W-7405- ENG-36) and LBNL (Contract No. DE-AC03-76SF00098). The Spectromicroscopy Facility (Beamline 7.0) and the Advanced Light Source were built and are supported by the DOE Office of Basic Energy Research. The authors wish to thank Jason Lashley and Michael Blau for synthesis of the Pu samples.

REFERENCES

[1] Tobin, J.G., B.W. Chung, R.K. Schulze, J. Terry, J.D. Farr, D.K. Shuh, K. Heinzelman, E. Rotenberg, G.D. Waddill and G. Van der Laan, *Phys. Rev. B*, 68, 1155109 (2003).

[2] Moore, K.T., M.A. Wall, A.J. Schwartz, B.W. Chung, D.K. Shuh, R.K. Schulze and J.G. Tobin, *Phys. Rev. Lett.*, 90, 196404 (2003).

[3] van der Laan, G., K.T. Moore, J.G. Tobin, B.W. Chung, M.A. Wall and A.J. Schwartz, *Phys. Rev. Lett.*, 93, 097401 (2004).

[4] Kutepov, A.L. and S.G. Kutepova, *J. Phys.: Cond. Mat*., 15, 2607 (2003); A.L. Kutepov, Private Communication, UCRL-TR-200654.

[5] Sadigh, B., P. Soderlind and W.G. Wolfer, *Phys. Rev. B*, 68, 241101 (2003).

[6] Penicaud, M., *J. Phys.: Cond. Mat*., 9, 6341 (1997).

[7] Savrasov, S.Y. and G. Kotliar, *Phys. Rev. Lett*., 84, 3670 (2000); S.Y. Savrasov, G. Kotliar and E. Abrahams, *Nature*, 410, 793 (2001).

[8] Soderlind, P., *et al*., *Phys. Rev. B*, 55 (1997); P. Soderlind, *Adv. In Phys*., 47, 956 (1998).

[9] Wills, J.M., O. Eriksson, A. Delin, P.H. Andersson, J.J. Joyce, T. Durakiewicz, M.T. Butterfield, A.J. Arko, D.P. Moore and L.A. Morales, *Cond-Mat*/0307767; J.J. Joyce, J.M. Wills, T. Durakiewicz, M.T. Butterfield, E. Guziewicz, J.L. Sarrao, L.A. Morales and A.J. Arko, *Phys. Rev. Lett*., 91, 176401 (2003) and references therein.

[10] Soderlind, P., A. Landa and B. Sadigh, *Phys. Rev. B*, 66, 205109 (2002); P. Soderlind and B. Sadigh, *Phys. Rev. Lett*., 92, 185702 (2004).

[11] Denlinger, J.D., E. Rotenberg, A. Warwick, G. Visser, J. Nordgren, J.H. Guo, P. Skytt, S.D. Kevan, K.S. McCutcheon, D.K. Shuh, J. Bucher, N. Edelstein, J.G. Tobin and B.P. Tonner, *Rev. Sci. Instrum*., 66, 1342 (1995).

[12] Lashley, J.C., *J. Nucl. Matl*., 274, 315 (1999).

[13] Yeh, J.J. and I. Lindau, *At. Data Nucl. Data Tables*, 32, 1 (1985).

[14] Bedrossian, P., *et al*., MRS Proceedings, 437, 79 (1996).

[15] Naegele, J.R., *J. Nucl. Matl*., 166, 59 (1989).

[16] Gouder, T., *et al*., *J. Alloys Cmpds*., 271-273, 841 (1998); *J. El. Spect. Rel. Phen*., 101-105, 419 (2000).

[17] Baptist, R., D. Courteix, J. Chayrouse and L. Heintz, *J. Phys. F (Metal Phys.)*, 12, 2103 (1982).

[18] Cox, L.E., *Phys. Rev. B*, 37, 8480 (1988).

[19] Havela, L., *et al*., *Phys. Rev. B*, 65, 235118 (2002) and references therein.

[20] Courteix, D., J. Chayrouse, L. Heintz and R. Baptist, *Solid State Commun*., 39, 209 (1981).

[21] Veal, B., *et al*., *Phys. Rev. B*, 15, 2929 (1977).

[22] Butterfield, M., T. Durakiewicz, E. Guziewicz, J.J. Joyce, D.P. Moore, A.J. Arko and L.A. Morales, *Mat. Res. Soc. Proc*., 802, 81 (2004).

Uranium Chemistry

Chair: L. Soderholm

IN SITU SPECIATION OF ACTINIDES IN SOLUTION WITH A NEWLY DEVELOPED SPECTRO-ELECTROCHEMICAL CELL

C. Hennig[1,2], **J. Tutschku**[1], **A. Rossberg**[1,2], **A.C. Scheinost**[1,2], **G. Bernhard**[1]
[1]Forschungszentrum Rossendorf, Institute of Radiochemistry
P.O. Box 510119, D-01314 Dresden, Germany
[2]The Rossendorf Beamline at ESRF, P.O. Box 220, F-38043 Grenoble, France

Abstract

An electrochemical cell was developed for *in situ* investigations of radioactive materials using X-ray absorption spectroscopy. Due to the specific safety requirements for handling of radioactive materials the electrochemical cell had to be gas tight. The spectro-electrochemical cell comprises two safety compartments and a special electrode arrangement in order to avoid any gas release.

Introduction

Natural aquatic and terrestrial environments exert large variations in redox state due to oxygen diffusion on one hand and microbial processes on the other hand [1,2]. Actinides with their large number of oxidation states are especially susceptible to these redox changes, forming a large number of aqueous complexes which may greatly differ by solubility and mobility. These complexes are often difficult to investigate due to their thermodynamic metastability. Therefore, we developed a new spectro-electrochemical cell, which allows to study the structure and speciation of aqueous actinide complexes *in situ* by X-ray absorption spectroscopy (XAS) while applying and maintaining a constant potential. First U L_{III}-edge X-ray absorption spectra have been obtained from aqueous solutions of U(VI) and U(IV) [3].

Design of the cell

While *in situ* investigations by combining electrochemical cells with XAS are not new [4], the prevention of any gas-releasing electrode reaction according to the special safety regulations for actinides required a new electrochemical approach. We used an Ag metal electrode as anode, where Ag is oxidised to Ag^+ and precipitates as AgCl. In order to avoid a high polarisation of the cell, no diaphragm was used. The cell itself consists of a double confinement (Figure 1) following the safety regulations for the use of radioactive samples at the ESRF. The cell body and the X-ray windows are machined from one piece of chemically resistant material, which is closed by air-tight cover plates. Two X-ray windows are arranged 20 mm apart from each other to allow sufficient X-ray transmission. Each cover plate contains up to six gas-tight connectors for cables and electrodes. The liquid volume of the cell is 10 mL. To realise a good homogenisation of the electrolyte, an adjustable magnetic stirrer was used, combined with a specific shaped chamber in order to guarantee a nearly laminar liquid flow in the cell.

As reference was used the Ag/AgCl potential. As working electrode (catode) we employed a Pt gauze. Using the U(VI)/U(IV) couple as example, the formal reaction at the catode is given by:

$$UO_2^{2+} + 4H^+ + 2e^- \rightarrow U^{4+} + 2H_2O \quad (1)$$

The reaction at the anode is the oxidation of silver and its precipitation as silver chloride:

$$2Ag + 2Cl^- \rightarrow 2AgCl\downarrow + 2e^- \quad (2)$$

The reduction of 0.01 M U(VI) to U(IV) at the catode is related with a transfer of two electrons. As compensating reaction at the anode 0.02 M Cl^- is needed enabling the precipitation of AgCl. X-ray absorption spectroscopy is element selective and shows only near-order effects in the close environment of the excited element. Therefore, the presence of Ag does not disturb the X-ray absorption measurements.

The redox potential is influenced by the pH value of the solution, by the activity coefficient and by geometrical arrangement of the electrodes. Therefore, the actual redox potential is determined prior electrolysis by cyclic voltammetry and is applied for the electrolysis. To gain more information on the reduction process a pH and an Eh electrode are situated in the cell. A thermocouple is used for temperature control.

Figure 1. Drawing of the spectro-electrochemical cell

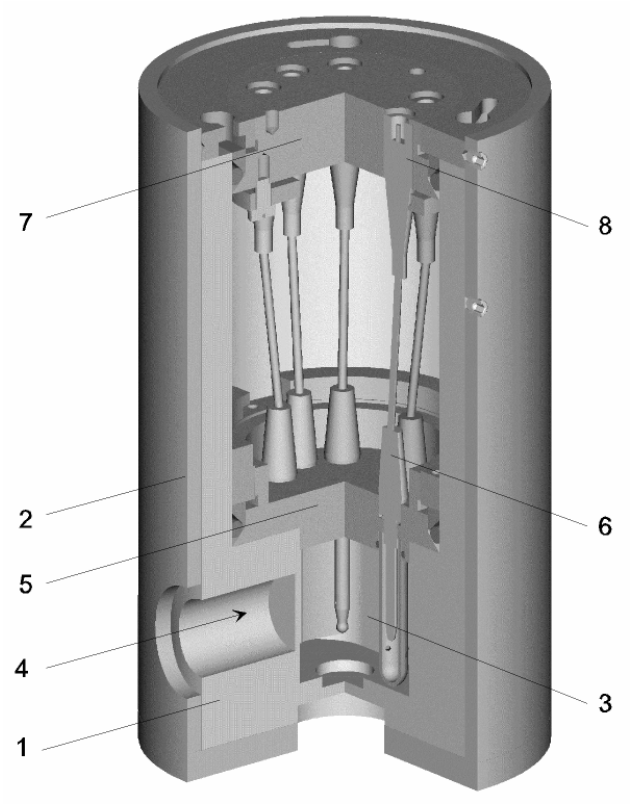

1 – Cell body of chemically resistant material
2 – Stainless steel housing
3 – Space for the sample solution
4 – X-ray window
5 – Inner cover plate (first compartement)
6 – Electrode
7 – Outer cover plate (second compartement)
8 – Electrical connector

***In situ* XANES measurements**

Prior preparation of the XANES experiment, independent UV-Vis measurements of the solutions are performed in order to verify that uranium was completely reduced (not shown here). In order to validate the complete reduction of U(VI) to U(IV) during the electrolysis procedure at the synchrotron, U L_{III}-edge XANES spectra are measured (Figure 2, left side). One XANES spectra spectrum was obtained each 30 minutes without interrupting the redox procedure. At the beginning of the experiment, the XANES spectrum indicates only the hexavalent oxidation state of uranium. After reduction, only U(IV) species are identified. A quantitative analysis of the uranium redox species are performed by factor analysis of the XANES spectra (Figure 2, right side).

The reduction of UO_2^{2+} to U^{4+} occur in two one-electron steps, with UO_2^{+} as the intermediate. The first step ($UO_2^{2+}$to UO_2^{+}) involves a simple electron transfer and is expected to be fast, while the second step (UO_2^{+} to U^{4+}) involves the breaking of U = O bonds and is expected to be slow. However, the intermediate state, UO_2^{+}, was not detected with the XANES measurements. The pentavalent oxidation state of uranium was also not detected by cyclic voltammogrametry.

Figure 2. *In situ* XANES measurmenents and species distribution in the solution

Left: U L_{III}-edge XANES spectra obtained during the reduction of 0.01M U(VI) at 0.2 M formic acid. The reduction was performed at constant potential of -350 mV vs. Ag/AgCl. Right: Distibution of U(VI):U(IV) species.

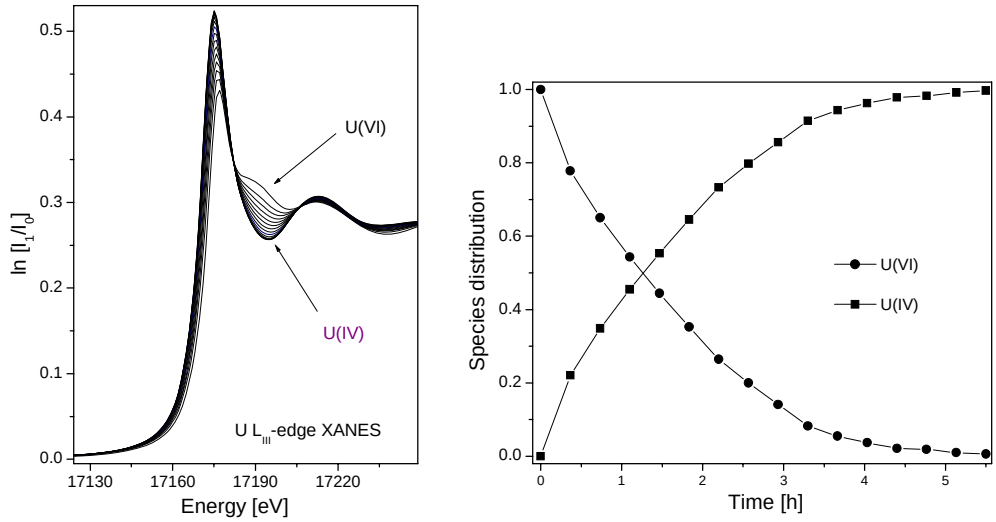

Acknowledgements

We thank D. Rettig and T. Reich for technical development of a first version and furthermore J. Claussner and D. Falkenberg for their support of the final development of the spectro-electrochemical cell. The EXAFS measurements were performed at the Rossendorf Beamline/ESRF [5].

REFERENCES

[1] Lovley, D.R., J.P. Phillips, Y.A. Gorby, E.R. Landa, *Nature*, 350, 413 (1991).

[2] Fredrickson, J.K., J.M. Zachara, D.W. Kennedy, M.C Duff, Y.A. Gorby, S.W. Li, K.M. Krupka, *Geochim. Cosmochim. Acta*, 64, 3085 (2000).

[3] Hennig, C., J. Tutschku, A. Rossberg, G. Bernhard, A.C. Scheinost, *Inorg. Chem.*, 44, 6655 (2005).

[4] Antonio, M.R., L. Soderholm, C.W. Williams, J-P. Blaudeau, B.E. Bursten, *Radiochim.* Acta, 89, 17 (2001).

[5] Matz, W., N. Schell, G. Bernhard, F. Prokert, T. Reich, J. Claussner, W. Oehme, R. Schlenk, S. Dienel, H. Funke, F. Eichhorn, M. Betzl, D. Pröhl, U. Strauch, G. Hüttig, H. Krug, W. Neumann, V. Brendler, P. Reichel, M.A. Denecke, H. Nitsche, *J. Synchrotron Rad.*, 6, 1076 (1999).

MicroXAS

Chair: A. Scheinost

MICRO-FOCUSED XRF, XAFS AND XRD INVESTIGATIONS OF U AND As SPECIATION IN LIGNITE-RICH CLAYEY SEDIMENT BORE CORES FROM RUPRECHTOV, CZECH REPUBLIC

M.A. Denecke[1], K. Janssens[2], A. Somogyi[3], K. Proost[2], J. Rothe[1], R. Simon[1], U. Noseck[4]
[1]Forschungszentrum Karlsruhe
PO Box 3640, D-76021 Karlsruhe, Germany
[2]Centre for Micro- and Trace Analysis, Department of Chemistry, University of Antwerp
Universiteitsplein 1, B-2610 Antwerp, Belgium
[3]European Synchrotron Radiation Facility
ID-22, B.P. 220, F-38043 Grenoble Cedex, France
[4]Gesellschaft für Anlagen- und Reaktorsicherheit (GRS) mbH
Theodor-Heuss-Str. 4, D-38122 Braunschweig, Germany

Abstract

Investigations using micro-focused synchrotron radiation techniques on a bore core section of a U-rich tertiary sediment from Ruprechtov, Czech Republic, are performed in order to assess mechanisms leading to immobilisation of the U during diagenesis. Information on such so-called natural analogues is important for long-term safety assessment of disposal of high-level radioactive waste in repositories in deep geological formations. Various (reflective and refractive) micro-focusing optics are used for performing local analyses: two polycapillary half-lenses in a confocal geometry (at HASYLAB) new planar SU-8 compound refractive lenses (at ANKA) developed and fabricated at ANKA, and Kirkpatrick-Baez mirrors (at ESRF). The confocal set-up is used to improve the depth selectivity of the analytical methods and, hence, visualise the distribution of elements in three dimensions in areas in and surrounding hot spots.

Introduction

The establishment of reliable prognoses and performance assessment (PA) of proposed waste disposal sites and strategies for high-level, heat producing nuclear waste requires basic understanding of processes determinant in the behaviour of radionuclides in or in contact with the waste form, the technological barrier of a repository, the deep geological formation and the surrounding environment. Requisite to this understanding is structural information and characterisation of nuclide speciation on a molecular scale, in a broad range of milieus. Nuclide speciation determines transport properties (mobilisation/immobilisation) reactivity, bioavailability and, hence, potential human and environmental risk. The number of factors defining the speciation of a radionuclide in the environment is immense, the compartments/substrates where reactions take place are heterogeneous, and the complexity of the problem is enormous. To further complicate matters, PA of proposed nuclear waste repositories must simulate conditions and the evolution of conditions over a time span covering the lifetime of the long-lived nuclides, which approaches a geological time scale.

This work intends to illustrate how the application of sophisticated X-ray spectroscopic techniques to investigate the speciation of uranium (U) in U-rich tertiary sediment from a natural analogue site from Ruprechtov, Czech Republic [1] help tackle these complex challenges. The application of synchrotron radiation-based X-ray techniques for radionuclide speciation investigations in molecular environmental science has experienced a boom over the past decade. The reasons for this increased activity are manifold, but one source is the increasing sophistication of the available tools, including advances in focusing methods. Studies of so-called natural analogue sites such as the Ruprechtov site attempt to gain information on a geological time scale important for assessing long-term repository safety. The Ruprechtov site has been chosen due to its geochemical and geological conditions being similar to sediments covering host rocks for deep geological waste repositories. We investigate U-rich sediment bore core sections from Ruprechtov using micro-focused synchrotron radiation to assess mechanisms leading to immobilisation of the U during diagenesis. Various X-ray imaging (reflective and refractive) micro-focusing optics are used: two polycapillary half-lenses in a confocal geometry, new planar compound refractive lenses (CRL) and Kirkpatrick-Baez mirrors. The μ range focused beam allows measuring X-ray absorption near edge (XANES) spectra from selected areas of interest in a heterogeneous sample. Scanning the beam focus over the sample while registering emitted fluorescence radiation allows imaging of elemental distributions. Performing such scans at differing, selected energies around an element absorption edge allows imaging the distribution of that element's oxidation state. The confocal set-up (Figure 1) is used to probe micro-volumes below the sample surface, thereby providing added depth information [2,3]. Tomographic cross-sections are obtained, which visualise the distribution of elements in three dimensions.

Figure 1. Schematic representation of the confocal set-up

By x,y scanning the sample and moving the sample through the focal volume stacks of tomographic cross-sections are obtained

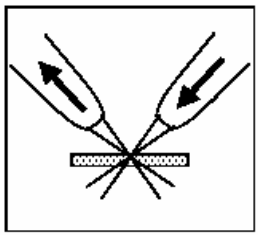

The Ruprechtov site and the bore core sample

The Ruprechtov natural analogue site is in the north-west Czech Republic. It exhibits depths with anomalously high U enrichment mainly in a lignite/clay horizon. The horizon is found between an over-burden of pyroclastic sediment, composed mainly of argillised volcanogenic sediment of the oligocene and miocene age, and an underlying low-permeable kaolin horizon some 60 m thick. Both a bulk section of an U-rich sediment bore core (Figure 2) obtained at approximately 34.5 m depth and a thin section of a bore core obtained from a neighbouring bore-hole at a similar depth (Figure 3) are investigated. The geochemical conditions at this depth are reducing (Eh -280 mV). The U in the sediment is tetravalent. The minerals ningyoite ($CaU[PO_4]_2$) tristramite $(Ca,U,Fe)(PO_4,SO_4)(2H_2O)$ uraninite ($UO_{2.X}$) and U-bearing monazite have been identified in bore core samples from the same depth [4].

Figure 2. Approximately 19.5 mm diameter bore core sample embedded in Plexiglas (left) and its autoradiographic image (right)

Quantification of uranium "hot spots" in the autoradiogram shows they contain ~150 μg ^{238}U/g material

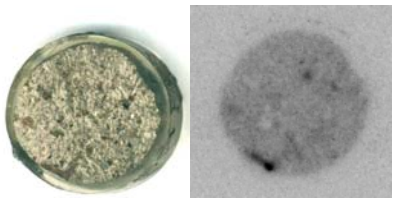

Figure 3. Core thin section with pencil markings as dark grey lines (~50 nm thick) mounted on a 25 × 45 mm^2 glass slide and its autoradiographic image (right)

The hot spot contains ~350 μg ^{238}U/g material

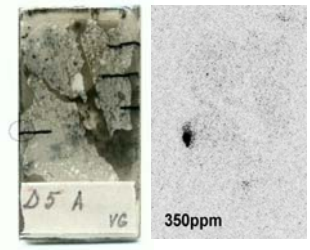

Experimental section

Measurements on the bulk bore core sample are performed using the confocal set-up. Two polycapillaries are used at the Beamline L at the Hamburger Synchrotronstrahlungslabor (HASYLAB) with monochromatic beam. The confocal set-up with a planar CRL as the primary focusing optic and a polycapillary as collimating optic is used at the Fluo-Topo Beamline at the Ångstrømquelle Karlsruhe (ANKA) using a band pass of wavelengths reflected off a multi-layer pair. The focal size is ~20 μm and depth resolution around 25 μm using two polycapillaries. With the CRL, the focal spot is about 2 μm × 5 μm (V × H) and the depth resolution ~16 μm. Measurements on the thin-section sample are made at ID22, European Synchrotron Radiation Facility (ESRF) using a Kirkpatrick-Baez mirror system to focus the monochromatic beam.

The energy of the monochromatic beam is calibrated against the white line (WL) in the XANES spectrum of a As_2O_3 reference sample for As K-edge measurements, defined as 11.867 keV. Element distribution images are created by scaling the fluorescence intensity for each image pixel to shades of black, grey and white. This is done by assigning the pixel with the largest fluorescence intensity signal the colour black, the pixel with the lowest intensity white, and scaling the remaining pixel intensities on a relative linear scale.

Results and discussion

Gross area scans and inspection of X-ray fluorescence at randomly selected sample U hot spots using the two polycapillary confocal set-up indicate that U is generally found near arsenic and iron. The distributions of these three elements in a 300 μm^2 area at varying depths from near the surface down to -225 μm below the surface using an excitation energy of the incident beam (E_{excite}) of 21 keV are shown in Figure 4. In the map recorded at -180 μm (Figure 4, top) a framboid Fe(II) nodule is evident near the centre of the image. A U hot spot is located just to the left of this nodule, as is an area of high As concentration. Both As and U appear to show low or no fluorescence intensity in the direct location of the Fe nodule. Another region of high U intensity is at the lower left hand part of the -180 μm image. The Fe nodule at the centre of the -180 μm image is reduced in size in the next image, 30 μm closer to the surface (Figure 4, -150 μm) indicating we are now viewing a cross-section near that nodule's top. Also evident at -150 μm are two more Fe nodules at the top right and lower part of the Fe distribution map. As in the -180 μm image, we observe high U Lα intensity at the lower left hand part of the image at -150 μm depth. It is now evident that this high U intensity region borders a Fe nodule, lying just to the right, and an emerging lignite inclusion near the surface, which is seen as a black formation in the optical micrograph and visible in the element distributions as an area void of nearly any U, As, Fe XRF signals. The As Kα intensity in the -150 μm image appears to border the pixels with high Fe concentration. If we follow the nodule Fe Kα signal, clearly seen in the lower right quadrant of the -150 μm image, from -180 μm up to -60 μm and compare it to the development of the As Kα fluorescence, we gain the impression that As appears to cover – or envelope – the Fe nodule. This particular nodule is not yet entirely evident in the -180 μm image, at the lowest depth imaged. At -180 μm, the As signal is seen concentrated on or directly bordering the pixels, where, in the next image 30 μm closer to the surface (i.e. at -150 μm) the nodule is seen. As we scan at depths 30 μm and 60 μm closer to the surface (the -120 μm and -90 μm images) the pixels with high As counts seem to "close" over the nodule, as the successive recorded images encompass the upper hemisphere of the Fe nodule with smaller cross-section diameters. In the final image of the series, -60 μm below the surface, the As exhibits high intensity above the pixels where the Fe nodule is located below. If we follow the U distribution in this same series, the U fluorescence appears near, but not on top of As or Fe.

To identify the As species, a number of As K XANES spectra are recorded at various locations in the bore core high in As content at depths varying from near the surface to more than -200 μm below. The measured XANES are depicted in Figure 5. Included in Figure 5 are the energy positions of the WL for As in the 0, III and V valence states (11.864 keV, 11.867 keV and 11.870 keV, respectively) measured at HASYLAB [5]. When we compare the energy position of the WL of these spectra with that expected for As in different valence states, we find that spectra A, B, C, E, F and H have WL corresponding to As(V) and spectra D and G that for As(0). Spectra B and E clearly exhibit a XANES feature just to the low energy side of the WL, with its position also corresponding to As(0). In spectra A and C this feature is reduced to a shoulder, indicating a lower As(0):As(V) ratio at the particular bore core volume sampled. Spectra I and J have WLs with energies for As(0) and As(V) of near equal intensity. Because both As oxidation states are found below the sample surface, the presence of As(V) in the spectra can be safely ruled out to be an artefact resulting from surface oxidation. In addition,

Figure 4. Elemental distribution maps for Fe, As and U recorded at indicated depths below the surface (between -180 μm and -60 μm; 20 × 20 μm^2 step size) of a 300 × 300 μm^2 section of the sample studied marked in the optical photograph (left)

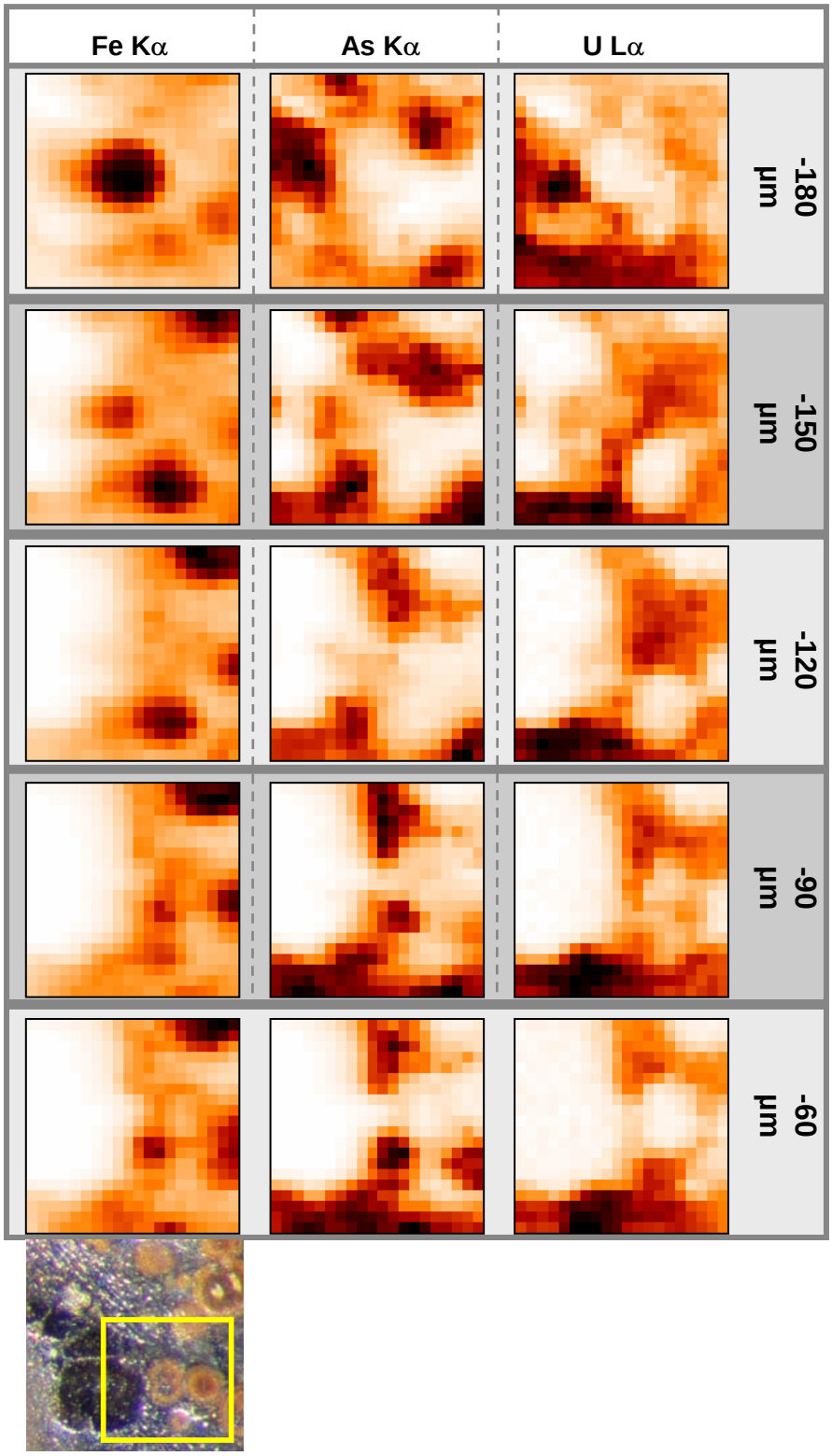

Figure 5. As K μ-XANES recorded at various positions and depths below the surface of the bore core section

Vertical lines denote energy positions expected for As(0) (dotted) As(III) (dashed) and As(V) (continuous)

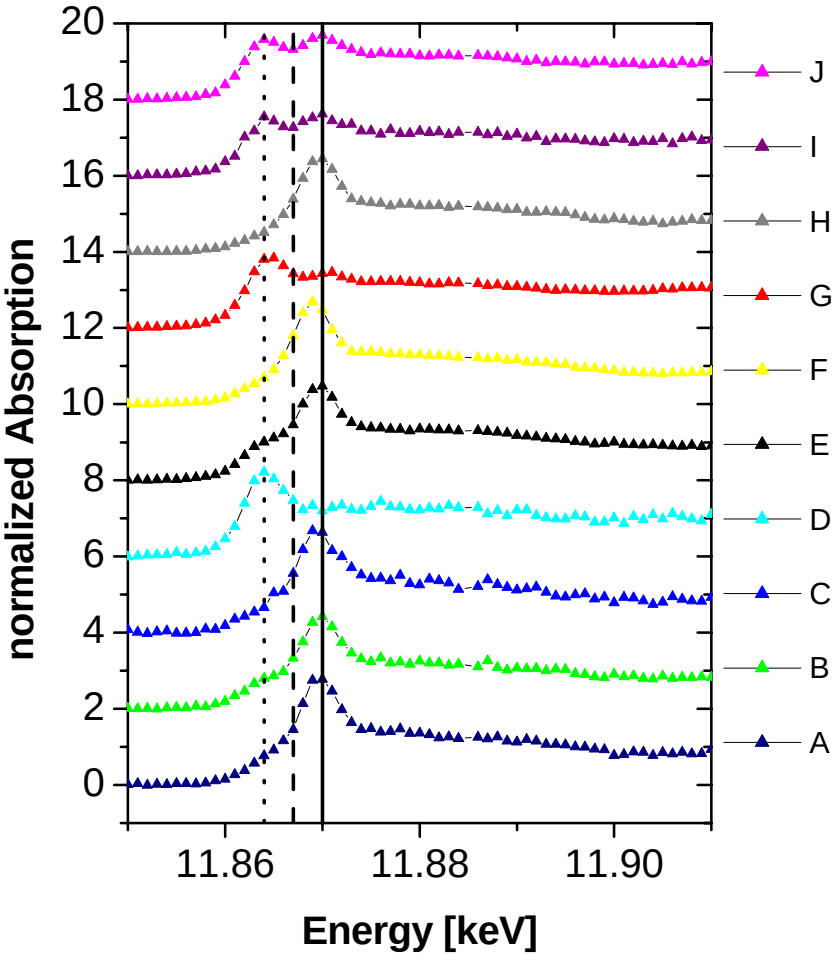

repeated measurement of the same sample area after hours of irradiation revealed no significant XANES amplitude variations (compare spectra F with H and I with J). The As oxidation state mixture observed in the bore core is not a result of any photo-reduction of the X-ray beam.

Because dissolved arsenate and arsenite are known to partition to iron sulphide, forming orpiment or arsenopyrite [6,7], because the position of the lower energy XANES peak in the spectra shown in Figure 5 corresponds to that reported for arsenopyrite [8], and because As in the distribution images in Figure 4 appears to envelop the Fe nodules, we record the Fe, As and U distributions in the bulk sample and in a thin section sample with a much higher spatial resolution (approximately a ten-fold and five-fold smaller beam in the vertical and horizontal dimensions, respectively). Results for the bulk sample using a CRL and confocal geometry are shown in Figure 6 and results for the thin-section using a KB mirror system in Figure 7. Because we observe As present in different oxidation states (Figure 5) the As distribution in the thin-section sample is recorded at varying E_{excite}, in order to obtain oxidation state distribution maps for As. The results are also shown in Figure 7 (left).

Figure 6. Confocal μ-XRF maps of a 120 × 120 μm^2 section (2 × 4 μm^2 step size) -60 μm^2 below the surface

Circles indicate U hot-spots. Dashed lines indicate As-rich rim around Fe(II)-nodule. The microscopic image shows the area studied.

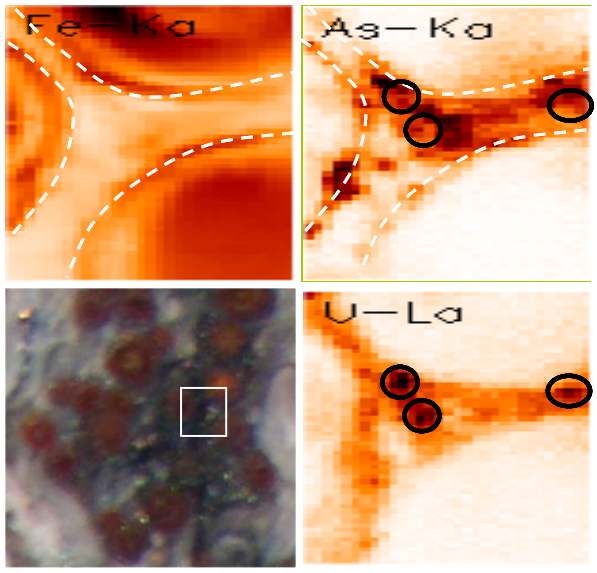

Figure 7. μ-XRF maps of a 150 × 150 μm^2 section (2 × 4 μm^2 step size) of the thin-section sample

Images marked Fe, As and U are recorded with E_{excite} = 18 keV, that marked As(0) with E_{excite} = 11.861 keV, and that marked As(V) is the difference between an image recorded at 11.87 keV and the As(0) image

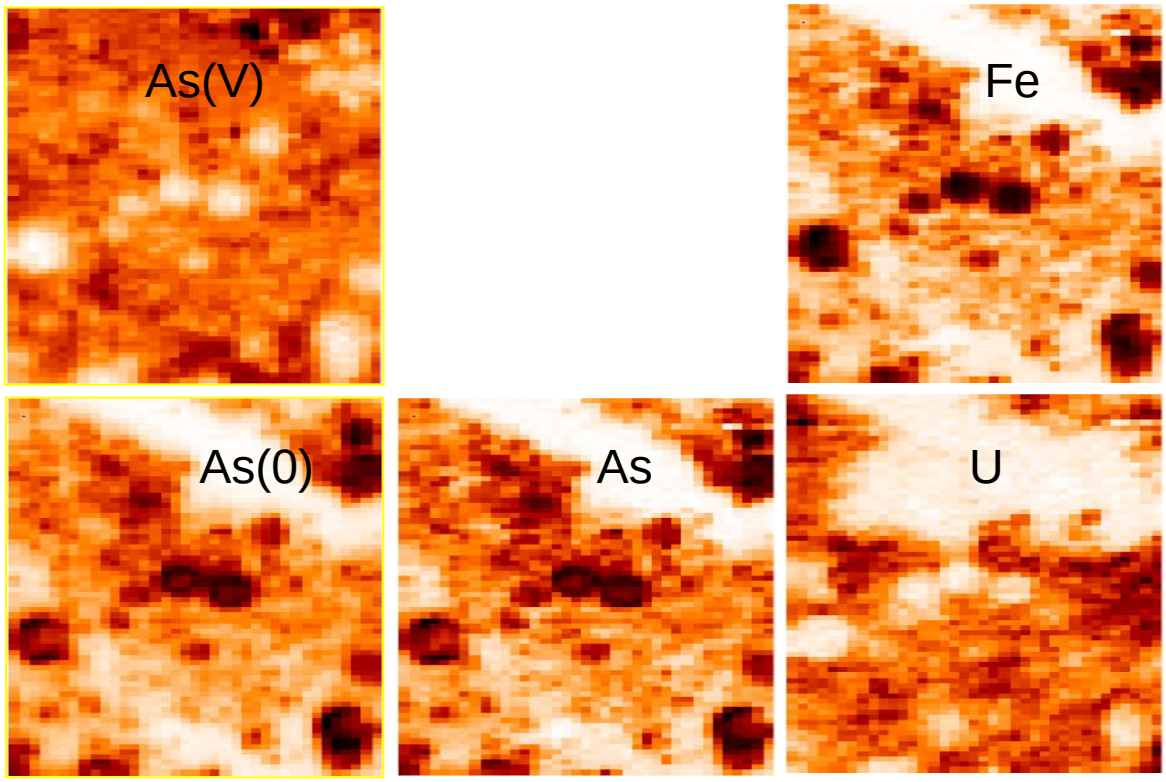

In Figure 6, we observe a qualitative, general inverse relationship between the Fe fluorescence signal and those observed for As and U. Correlations extracted from elemental maps around U hot spots (not shown) reveal that U is consistently in close association with As. However, areas rich in As almost invariably do not overlap U hot spots; they are immediately adjacent. Also, as a direct result of the high lateral resolution using the CRL, it is possible to discern an As-rich boundary layer surrounding the Fe nodules in Figure 6. The framboid Fe nodules in the thin section (Figure 7) are only a fraction of the size of those in the bulk sample. However, the general observation of low fluorescence intensity for U in pixels with high Fe intensity is also valid for the images recorded with E_{excite} 18 keV. Similar to the high resolved images of the bulk sample, the thin section areas rich in As are also immediately adjacent to the Fe nodules. The As(0) distribution in Figure 7 is obtained from the As Kα fluorescence recorded using E_{excite} 11.861 keV, which is on the rising edge for As(0) but 9 eV below the WL of As(V). The As(V) distribution is obtained as the difference between As Kα fluorescence recorded using E_{excite} set to the As(V) WL energy (11.870 keV) and that registered using E_{excite} 11.861 keV, i.e. map at 11.87 keV minus the As(0) map. Upon comparison of the As(0) distribution with that for As(V) we find that As(0) appears concentrated in pixels where the total As signal is observed to be high. In contrast, the As(V) is in areas void of Fe and As(0).

Element correlation plots of the measured intensities in each pixel of the images shown in Figure 7 for As Kα versus Fe Kα as well as As Kα in the As(V) distribution versus U Lα are shown in Figure 8. We find the normalised As Kα signal for As(0) to be proportional to the Fe Kα, whereas for As(V) it decreases in a non-linear manner with increasing Fe Kα intensity. An As(0)-Fe proportionality indicates that As(0) is associated with the same phase as Fe. We conclude from these observations, together with the fact that the corresponding XANES energy is same as for arsenopyrite, that it is likely arsenopyrite is associated with the Fe nodules. The slope of the As(0)-Fe correlation plot tends to decrease at high As Kα counts. We contribute this as a result of the arsenic coating Fe nodules, visualised in the distribution images. We recognise that As(V) is a minority species in the sediment because the As(0)-Fe correlation hardly differs from the total As (i.e. As image recorded at 18 keV) versus Fe correlation. In addition, a complicated correlation between As(V) and U (Figure 8, bottom) is observed. There is a near baseline correlation, which indicates that some As(V) is associated with merely trace but constant amounts of U. The rest of the correlation is highly scattered, but we find no U, which is not associated with As(V).

Figure 8. Inter-element diagrams from data shown in Figure 7 for normalised As Kα versus Fe Kα intensities in each pixel for the three As distribution images [As, As(0), As(V)] and the Fe image and for the As(V) map versus normalised U Lα intensities (right)

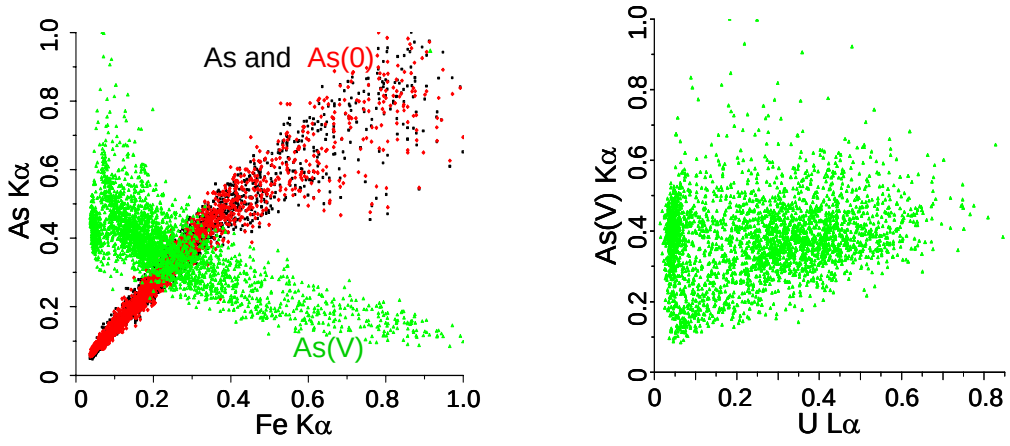

Conclusion

From element and oxidation state distribution maps combined with XANES results, we find arsenopyrite associated with framboid Fe pyrite nodules in the U-rich sediment studied. The arsenopyrite appears as a coating on the nodules. We find no evidence for any gradient of an $As_{1-x}Fe_x$ type. In addition, As(V) is also found in the samples in the presence of As(0) including volumes probed below the surface. The As(V) is found to be associated with U. These observations allow us to formulate a hypothesis for the mechanism of U immobilisation during diagenesis of the sediment. We propose that mobile groundwater-dissolved U(VI) was reduced on arsenopyrite in the sediment, leading to precipitation of less-soluble U(IV) thereby forming As(V). The arsenopyrite must have formed after framboid Fe nodules, as they are found as coatings on the surface.

Acknowledgements

We thank J. Römer for the autoradiograhic measurements and the ANKA, HASYLAB and ESRF facilities for beamtime.

REFERENCES

[1] Noseck,, U., Th. Brasser, P. Raijlich, M. Hercik, A. Laciok, A. *Radiochim. Acta* (accepted).

[2] Janssens, K., K. Proost, G. Falkenberg, *Spectrochimica Acta*, 59, 1637 (2004).

[3] Smit, Z., K. Janssens, K. Proost, I. Langus, *Nuclear Instruments and Methods in Physics Research B*, 219-220, 35 (2004).

[4] Noseck, U., Th. Brasser, A. Laciok, M. Hercik, F. Woller, in *Uranium in the Aquatic Chemistry*, Springer (B. Merkel, *et al*., Eds.), Berlin, Heidelberg (2002).

[5] Denecke, M.A., H. Friedrich, T. Reich, G. Bernhard, T. Kniess, D. Rettig, T. Zorn, H. Nitsche, *HASYLAB Annual Report 1996*, pp. 751.

[6] Bostick, B.C., S. Fendorf, *Geochim. Cosmochim. Acta*, 67, 909 (2003).

[7] Moore, J.N., W.H. Ficklin, C. Johns, *Environ. Sci. Technol*., 22, 432 (1988).

[8] Colleen, M.H., M.J. La Force, S. Fendorf, S. Sutton, *Environ. Sci. Technol*., 36, 1988 (2002).

Actinide Sorption

Chair: S. Lequien

EXAFS STUDY OF URANIUM(VI) SORPTION ON KAOLINITE

Tobias Reich, Samer Amayri, Jakob Drebert
Institute of Nuclear Chemistry
Johannes Gutenberg-Universität Mainz
Germany

Sergei Boulyga
Institute of Inorganic Chemistry and Analytical Chemistry
Johannes Gutenberg-Universität Mainz
Germany

Abstract

We studied the sorption of U(VI) onto the reference kaolinite KGa-1b both by batch experiments and EXAFS measurements. Sorption samples were prepared at total U concentrations ranging from 1 μmol/L to 20 μmol/L, 4 g/L kaolinite, pH 3 to 10, presence and absence of ambient CO_2, and 60-h equilibration. The U-O_{ax}, U-O_{eq} and U-Al/Si distances measured by EXAFS suggest that U(VI) was bonded in an inner-sphere fashion. In the presence of atmospheric CO_2, the average U-O_{eq} distance increased from 2.32 to 2.38 Å when the pH was increased from 5.0 to 8.5. This could point to the formation of ternary U(VI)-carbonato complexes on kaolinite. The short U-Al/Si distance of approximately 2.7 Å can be rationalised by co-ordination of U atoms to [SiO_4] tetrahedra. There was no evidence for U neighbours in the EXAFS spectra, suggesting that the adsorbed U(VI) complexes were predominantly monomeric.

Introduction

Sorption of uranium on clay minerals such as kaolinite strongly affects the fate and mobility of uranium in the geosphere. Several groups have studied the sorption of U(VI) on kaolinite in batch experiments [1-3]. Sekine, *et al*. [1] investigated the sorption of 1 μM U(VI) on kaolinite in the pH range of 3.0-10.0 at ambient CO_2. The U(VI) sorption strongly increased above pH 4 and reached 100% in the pH range from 6 to 8. Above pH 8, the amount of U(VI) sorbed onto kaolinite decreased due to the formation of U(VI) carbonato species in aqueous solution. Redden, *et al*. [2] and Sekine, *et al*. [1] performed U(VI) sorption experiments on kaolinite in closed systems without CO_2. Their experiments with 10 and 1 μM U(VI) showed that 100% of the uranium is sorbed onto kaolinite in the pH range 6 to 10.

Thompson, *et al.* [4] performed EXAFS measurements on U(VI) sorption on kaolinite as a function of pH in the presence and absence of CO_2. The solid to liquid ratio was 0.5 g kaolinite/L. The amount of uranium sorbed from 20 μM U(VI) solution was in the range of 6 000-10 000 ppm. The EXAFS spectra of all samples showed a splitting of the equatorial oxygen shell of uranium with U-O_{eq} distances of 2.29 and 2.47 Å, indicating the formation of inner-sphere sorption complexes. A weak feature in the Fourier transform of the U L_3-edge EXAFS at approximately 3.0 Å was interpreted as U-Si/Al interaction. The EXAFS spectra of samples prepared in air at pH 6.0-7.0 did not show any U-U interaction. Above pH 7 the observation of a U-U interaction at 3.87 Å indicated the formation of multimeric uranium species. When CO_2 was excluded from the system, the size of the multimeric uranium species increased slightly. Thompson, *et al*. concluded that surface precipitates might have formed in the pH range of 7.1-8.0.

The aim of our study was to combine batch experiments with EXAFS spectroscopy to study the speciation of U(VI) at the kaolinite surface in more detail with emphasis on uranium loadings that are one order of magnitude below those of the previous EXAFS measurements.

Experimental

Batch experiments

The kaolinite KGa-1b (Source Clays Repository) was suspended in 0.1 M $NaClO_4$ solution. For the batch experiments, 50 mL polypropylene centrifuge tubes were used. The total volume of the aqueous phase was 40 mL. The solid to liquid ratio was 4 g/L. After three days, the pH of each sample was adjusted to the desired value in the range of 3.0-8.5 using 0.1 M NaOH and $HClO_4$, respectively. To speed up the equilibration with atmospheric CO_2, certain aliquots of 1 M $NaHCO_3$ solution were added to samples with pH ≥ 7. The pH was controlled and readjusted if necessary over a period of three days. Then, aliquots from a 1 mM U(VI) stock solution were added with immediate readjustment of the pH. The total U(VI) concentration was 1 and 10 μM, respectively. Between these preparation steps, the samples were placed on an end-over-end rotator (16/min). After a contact time of 60 hours, the final pH (see Table 1) was determined and the solid and liquid phases were separated by centrifugation for 10 min. at 10 000 rpm. The uranium content in the liquid and solid phases was determined by inductively coupled plasma mass spectrometry and instrumental neutron activation analysis, respectively.

EXAFS measurements

The samples for the EXAFS measurements were prepared such as to determine the U(VI) speciation as a function of pH, total uranium concentration and presence or absence of CO_2. Samples 1-4 were

prepared from 10 μM U(VI) under ambient conditions at pH 5.0, 6.0, 7.0 and 8.5, respectively, as described above. To study the influence of the uranium concentration, we prepared Samples 5-7 at pH 7.0 with 5, 10 and 20 μM total U(VI) and CO_2 present. Sample 8 was prepared at pH 8.5 and 10 μM U(VI) under Ar atmosphere for comparison with Sample 4 prepared under identical conditions in the presence of CO_2. For EXAFS measurements, approximately 200 mg of the sample was placed as a wet paste in the sample holder and sealed with Kapton tape and a double layer of polyethylene foil.

The uranium L_3-edge EXAFS spectra were recorded in fluorescence mode at room temperature at the Rossendorf Beamline (ROBL) [5] at the European Synchrotron Radiation Facility (ESRF). Depending on the amount of uranium in the sample, five to twelve scans were averaged and corrected for detector dead time. The software package EXAFSPAK was used for the analysis of the EXAFS data. Theoretical scattering phases and amplitudes were calculated using the *ab inito* code FEFF 8.20 [6] and an atomic cluster based on the crystal structure of soddyite [7].

Results and discussion

Batch experiments

Figure 1 shows the sorption curves for 1 and 10 μM U(VI) obtained in the presence and absence of CO_2 for pH 3.0-10.0. For 1 μM total U(VI) the absorption edge occurs at pH 5. This observation agrees with the previous results of Sekine and Redden, *et al*. [1,2]. Maximum absorption occurs at pH ≥ 6. In the presence of CO_2, the uptake by kaolinite starts to decrease at pH 8.5. At 10 μM total U(VI) the sorption edge is shifted slightly higher to pH 6. The uranium uptake decreases above pH 8 in the presence of CO_2 and remains at 100% in the CO_2-free system (see Figure 1, right). It can be concluded that the results of our batch experiments are in good agreement with previous studies.

Figure 1. Experimental adsorption data for total U(VI) concentrations of 1 μM (left) and 10 μM U(VI) (right)

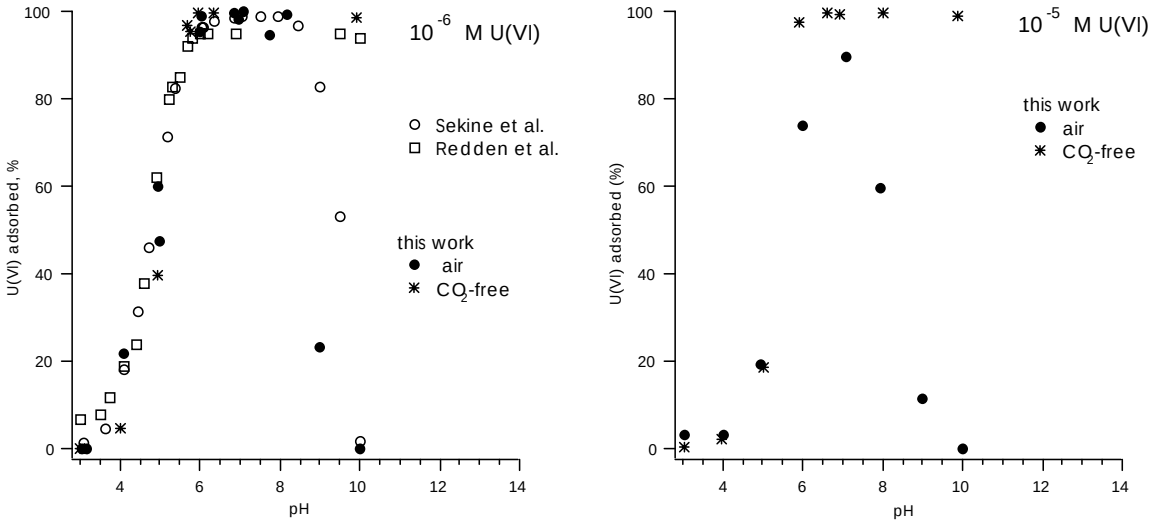

The results of the chemical analysis of Samples 1-8 used in the EXAFS measurements are summarised in Table 1. The adsorption data for the majority of these samples can also be seen in the sorption curves for 10 μM U(VI) given in Figure 1. The highest uranium loading of the EXAFS samples was 1 200 ppm and the lowest loading was less than 100 ppm, i.e. significantly less than in the previous EXAFS study of Thompson, *et al*. [4].

Table 1. Initial U(VI) concentration in the solutions and analytical results for the EXAFS samples. Samples 1-7 were prepared in air-equilibrated solutions.

Sample	[U(VI)] μmol/L	pH_{start}	pH_{final}	ppm adsorbed	% adsorbed
1	10	5.0	4.96	99	16.6
2	10	6.0	5.94	468	78.6
3	10	7.0	6.93	540	90.7
4	10	8.5	8.43	73	12.2
5	5	7.0	6.71	291	97.6
6	10	7.0	6.67	581	97.6
7	20	7.0	6.83	1 161	97.6
8	10, no CO_2	8.5	8.52	591	99.3

EXAFS measurements

The raw data of the U L_3-edge k^3-weighted EXAFS spectra of Samples 1-8 together with the best theoretical fit to the data and the corresponding Fourier transforms (FTs) are shown in Figure 2. The metrical parameters derived from the least-square fits are summarised in Table 2. As expected for U(VI) the average distance between uranium and its two axial oxygen atoms, O_{ax}, is nearly constant for all samples and equals 1.78 ± 0.02 Å. The average co-ordination number for the equatorial oxygen atoms, O_{eq}, is five. As can be seen from Table 2, the average U-O_{eq} distance varies between 2.32-2.38 Å. Therefore, it is interesting to discuss these changes in more detail.

Table 2. EXAFS fit results

Sample	Conditions	$2 \times O_{ax}$		$5 \times O_{eq}$		$1 \times Si$	
	[U(VI)] (μM)/pH	R(Å)	σ^2(Å^2)	R(Å)	σ^2(Å^2)	R(Å)	σ^2(Å^2)
1	10/ 5.0, air	1.78	0.002	2.32	0.012	2.71	0.008
2	10/ 6.0, air	1.78	0.001	2.33	0.011	2.69	0.008
3	10/ 7.0, air	1.78	0.001	2.35	0.011	2.72	0.006
4	10/ 8.5, air	1.80	0.001	2.38	0.010	2.71	0.004
5	5/7.0, air	1.79	0.002	2.35	0.011	2.74	0.006
6	10/7.0, air	1.79	0.001	2.35	0.011	2.74	0.008
7	20/7.0, air	1.79	0.001	2.35	0.014	2.88	0.004
8	10/ 8.5, no CO_2	1.79	0.001	2.32	0.013	2.71	0.008

The U-O_{eq} distance increases from 2.32 to 2.38 Å with increasing pH from 5.0 to 8.5 in the presence of CO_2 (Samples 1-4, Table 2). These distances are shorter than 2.41 ± 0.02 Å, the average U-O_{eq} distance of the U(VI) aquo ion [8]. This indicates inner-sphere sorption of U(VI) onto the kaolinite surface. Sample 8, which was prepared at pH 8.5 without CO_2, can be compared to Sample 4, which was prepared at the same pH but in the presence of CO_2. In contrast to Sample 4, the average U-O_{eq} distance for Sample 8 is 2.32 ± 0.02 Å. This is the same short U-O_{eq} distance as observed at pH 5.0 (Sample 1). It can be concluded that the presence of CO_2 leads to a lengthening of the average value of the U-O_{eq} bond distance. A change in pH from 5.0 to 8.5 does not have any influence on the average U-O_{eq} distance in the CO_2-free samples. The average U-O_{eq} bond distances of the aqueous $[UO_2(CO_3)_3]^{4-}$ complex is 2.44 ± 0.02 Å [9]. Therefore, the observed lengthening of the U-O_{eq} bond distance with increasing CO_3^{2-}/HCO_3^- in solution may indicate the formation of ternary U(VI) surface complexes with carbonate on the kaolinite surface.

Figure 2. Uranium L_3-edge k^3-weighted EXAFS spectra (left) and their corresponding Fourier transforms (right) for U(VI) adsorbed on kaolinite

Refer to Table 1 for the description of Samples 1-8. Dashed lines are fits to the spectra.

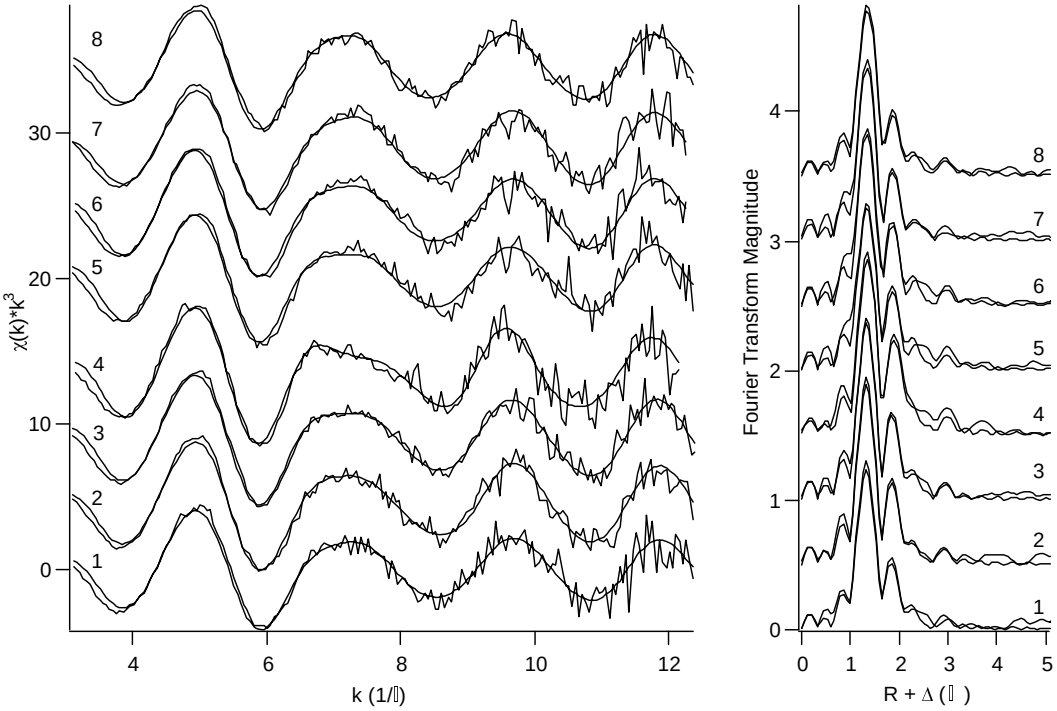

Samples 5-7, which were prepared at pH 7 but different U(VI) concentrations, did not show any change in the average U-O_{eq} bond distance (see Table 2). This indicates that the speciation of the U(VI) surface complexes at pH 7 does not change in the range of 5 to 20 μM U(VI) in solution. Even at the highest uranium loading of 1 200 ppm (Sample 7) the EXAFS spectrum did not show any indication of a U-U interaction or formation of polymeric surface complexes.

The theoretical fits to the raw data improved significantly when the structural model included a U-Si co-ordination shell. The average U-Si distance in Samples 1-6, and 8 was 2.74 ± 0.02 Å. Since the scattering properties of Si and Al are very similar, it is impossible to distinguish between these two back-scattering atoms in EXAFS spectra. However, a U-Al distance of 2.74 Å cannot be explained by the co-ordination of U(VI) to [AlO_6] octahedra of kaolinite. The expected U-Al distance for such co-ordination would be in the range of 3.2-4.2 Å [10]. This is much longer than the U-Si/Al distance observed for kaolinite. The interaction of U(VI) with [SiO_4] tetrahedra can result in U-Si distances between 2.7-3.5 Å depending on the edge-sharing or corner-sharing geometries of the [UO_2O_5] pentagonal bipyramid and the [SiO_4] tetrahedron. These geometries can be found in the mineral soddyite, $(UO_2)_2SiO_4 \cdot 2H_2O$ [7]. According to the crystal structure of soddyite, the U-Si distances equal 3.16 and 3.80 Å for edge sharing and corner sharing with [SiO_4], respectively. Although the U-Si distance for the sorption samples fall in the range for corner sharing, this possibility should be investigated further.

Conclusions

The batch experiments of U(VI) sorption on kaolinite showed significant differences between systems with and without CO_2. The strong decrease of the amount of U(VI) sorbed above pH 7

(10 μM U(VI) $p(CO_2) = 10^{-3.5}$ atm) can be rationalised by the formation of U(VI) carbonato complexes in solution. The EXAFS experiments wherein CO_2 was present showed that there is a change in U(VI) speciation at the kaolinite surface with increasing pH. The lengthening of the average $U\text{-}O_{eq}$ bond distance could indicate the formation of ternary surface complexes with carbonate. Such surface complexes have been detected in the case of U(VI) adsorption on hematite [11,12]. This conclusion is supported by the observation that the $U\text{-}O_{eq}$ distance remains constant over the pH range 5.0-8.5 when CO_2 was absent.

The EXAFS experiment showed that U(VI) forms inner-sphere, monomeric surface complexes with kaolinite in the pH range of 5.0-8.5 and total U(VI) concentration of 5-20 μM. A weak and broad feature in the Fourier transform of all samples at approximately 2.3 Å (see Figure 2) could be fit best with one Si atom at an average U-Si distance of 2.74 ± 0.02 Å. This very short U-Si distance can be rationalised by a corner-sharing model of U(VI) with the $[SiO_4]$ tetrahedrons of kaolinite. However, this possibility needs to be investigated further, for example, by measuring the EXAFS spectra of suitable reference samples.

Acknowledgements

We thank the German Bundesministerium für Wirtschaft und Arbeit (Project 02 E 9653) for the financial support. A. Bauer from the Forschungszentrum Karlsruhe is gratefully acknowledged for the preparation of the kaolinite size fraction < 2 μm. We acknowledge the European Synchrotron Radiation Facility for provision of synchrotron beam time and would like to thank H. Funke, C. Hennig, A. Roßberg and A. Scheinost from the Forschungszentrum Rossendorf for assistance in using the beamline BM20.

REFERENCES

[1] Sekine, K., T.E. Payne, T.D. Waite and J.A. Davis, Int*ernational Alligator Rivers Analogue Project (18): Experimental Study of Uranium Adsorption on Kaolinite-pH Dependence in Air-equilibrated System*, JAERI Memo 03–036 (1991).

[2] Redden, G.D., J. Li and J. Leckie, "Adsorption of U^{VI} and Citric Acid on Goethite, Gibbsite, and Kaolinite", in *Adsorption of Metals by Geomedia*, E.A. Jenne (Ed.) Academic Press, San Diego, pp. 291-314 (1998).

[3] Hyun, S.P., Y.H. Cho, P.S. Hahn and S.J. Kim, *J. Radioanal. Nuc. Chem.*, 250, 55 (2001).

[4] Thompson, H.A., G.A. Parks and G.E. Brown, Jr., "Structure and Composition of Uranium^{VI} Sorption Complexes at the Kaolinite-water Interface", in *Adsoption of Metals by Geomedia*, E.A. Jenne (Ed.), Academic Press, San Diego, pp. 349-370 (1998).

[5] Matz, W., N. Schell, G. Bernhard, F. Prokert, T. Reich, J. Claussner, W. Oehme, R. Schlenk, S. Dienel, H. Funke, F. Eichhorn, M. Betzl, D. Pröhl, U. Strauch, G. Hüttig, H. Krug, W. Neumann, V. Brendler, P. Reichel, M. A. Denecke, and H. Nitsche, *J. Synchrotron Rad*., 6, 1076 (1999).

[6] Ankudinov, A.L., C. Bouldin, J.J. Rehr, J. Sims and H. Hung, *Phys. Rev. B*, 65, 104107 (2002).

[7] Demartin, F., C.M. Gramaccioli and T. Pilati, *Acta Crystallogr.*, C48, 1 (1992).

[8] Allen, P.G., J.J. Bucher, D.K. Shuh, N.M. Edelstein and T. Reich, *Inorg. Chem*., 36, 4676 (1997).

[9] Bernhard, G., G. Geipel, T. Reich, V. Brendler, S. Amayri and H. Nitsche, *Radiochim. Acta*, 89, 511 (2001).

[10] Hennig, C., T. Reich, R. Dähn and A.M. Scheidegger, *Radiochim. Acta*, 90, 653 (2002).

[11] Bargar, J.R., R. Reitmeyer and J.A. Davis, *Environ. Sci. Technol.*, 33, 2481 (1999).

[12] Bargar, J.R., R. Reitmeyer, J.J. Lenhart and J.A. Davis, *Geochim. Cosmochim. Acta*, 64, 2737 (2000).

Facilities Reports and Updates

Chair: W.W. Lukens

THE NEW MULTI-TECHNIQUE BEAMLINE FOR RADIOACTIVE MATTER AT THE SOLEIL SYNCHROTRON

B. Sitaud[1] **and S. Lequien**[2]
[1]Synchrotron SOLEIL, Saint Aubin BP48, Gif-sur-Yvette, France, F-91192
[2]LPS, UMR 9956 CEA-CNRS, Gif-sur-Yvette, France, F-91191

Abstract

The construction of a new third-generation synchrotron facility in France, SOLEIL (*Source Optimisée de Lumière d'Énergie Intermédiaire de Lure*) offers a real opportunity to implement the experimental MARS beamline (*MAtière Radioactive à SOLEIL*) fully dedicated to research on a large number of high radioactive materials (α, β, γ and n emitters) up to 18.5 GBq per sample. The MARS beamline will be located on a bending magnet source and its X-ray optics have been designed for performing alternatively high-resolution powder diffraction and X-ray absorption fine structure spectroscopy from a standard configuration or a dispersive mode (access to ms scale time resolution) from 3.5 to 35 keV. The design also takes into account the requirements for focused and microfocused beams which contribute to decrease the total volume of analysed materials and consequently the dose rate. The MARS beamline should be opened beginning of 2007 to the international community.

Introduction

Understanding and modelling the properties of nuclear materials and radioactive nuclides are highly dependent upon the accuracy of experimental results. During the last decades, the use of synchrotron facilities which produce intense and bright X-ray beams over a large energy range has emerged as a key tool for the characterisation of structural, physical, chemical, electronic and magnetic properties of matter. The construction of a new third-generation synchrotron facility in France, SOLEIL (*Source Optimisée de Lumière d'Énergie Intermédiaire de Lure*) [1] offers a real opportunity to construct a new experimental beamline, MARS (*MAtière Radioactive à SOLEIL*) fully dedicated to research on radioactive matter.

The aims of the MARS beamline are clearly an extension of the current operational stations and of research towards the use of synchrotron radiation in multidisciplinary fields (physics, chemistry, biology) with respect to national and European safety regulations for preparation, handling, storage and transportation of radioactive materials. Hence the main characteristic is that this beamline will accommodate a large variety of radioactive samples (α, β, γ and n emitters) with an activity up to 18.6 GBq per sample. From this dedicated environment several experimental stations will be available and will allow a wide range of analyses with a relatively extended energy range.

Scientific requirements

The scientific needs which are at the genesis of this beamline project are numerous and clearly multidisciplinary. Ranges of environmental, geological and technological issues require systematic investigation of the properties of radioactive samples by synchrotron radiation. Indeed many of these fields are already topics of ongoing research using current synchrotron beamlines with *ad hoc* confinement sample holders. These studies have demonstrated the usefulness of synchrotron X-rays to solve many physico-chemical problems, but they also emphasise the need for a first-rate modern X-ray beamline allowing experiments carried out on highly irradiating samples under regular or drastic *in situ* conditions (high temperature, high pressure, etc.). The next paragraphs shortly review some issues pertaining to radioactive matter to be solved during the next ten years by three advanced techniques: X-ray absorption spectroscopy (XAS), micro X-ray diffraction (μXRD) and micro X-ray fluorescence (μXRF).

Carefully understanding the structural behaviour of nuclear fuels, fuel claddings and nuclear core elements is fundamental to optimising the current generation of reactor and for the design of new generation nuclear reactors. Mixed-oxide fuel (MOX) has been designed to recycle Pu from spent fuel and warheads. Optimal burning of Pu in MOX depends on the homogeneity of the solid solution and may be limited by the presence of structural defects, which in turn are connected to the protocol of fuel synthesis. The characterisation of the physical and chemical properties of MOX as a function of synthesis route and irradiation conditions will lead to a correlation between the heterogeneity of the microstructure and the fuel's mechanical and thermochemical properties, as well as its capacity to retain fission gases. Similar studies will apply to heterogeneous fuels, such as carbide or nitride ceramics dispersed in a ceramic or a metallic matrix developed to optimise actinide burning (Am, Cm). Due to severe thermochemical constraints and the formation of a wide variety of fission and activation elements, aged fuel constitutes an extremely complex system that should be studied step by step [2]. Therefore, the first systems to be studied will be simple and will probe materials in which a limited number of defects and/or doping elements are introduced with high precision by ion irradiation. Such experiments should provide reference data which will be extremely useful for interpreting the first results obtained directly from aged fuels.

Components of the structural framework of nuclear reactors are subject to intense neutron fluxes and heat-carrying water. Irradiation can dramatically alter the properties of these structural components by creating defects and forming important amounts of activated elements. The corrosion processes and the evolutions of the chemical and structural properties of zirconium claddings and steel materials upon irradiation have to be well identified and characterised from complementary investigations.

During the time the burned fuel is stored, this fuel may react with oxygen or radiolysis products. In this case, knowledge of the oxidation reactions is required to model the behaviour of spent fuel over long time scales. Characterisation of the chemical environment of long-lived fission products and neutron poisons is also crucial to predict release rates of radionuclides (RNs) during storage. High-level wastes generated by fuel processing are currently encased in glasses, and may be immobilised in ceramics that have enhanced retention properties in the future. The long-term tolerance of such matrices to RN decay and internal irradiation must be carefully evaluated to permit successful confinement of RNs over geological time scales. In addition, identifying the mechanisms of alteration and natural weathering of these materials is a prerequisite in the assessment of the impact of water intrusion into the radioactive waste repositories.

RN transfer from waste sites to subsurface environments is the key issue in designing waste disposal sites. Waste package structures as well as man-made barriers are engineered to protect each other and delay RN migration. The geological site then is selected to provide an additional natural retention barrier which is effective over geological time scales. To correctly quantify possible migration, two mechanisms must be correctly evaluated. First the sorption of the most mobile RN ions and their incorporation in all the barriers must be considered, and secondly, the retention influencing migration must be assessed by a detailed characterisation of the different interfaces. One should also note that concrete confinement barriers are expected to play a significant role in the retention of RN released either in a reactor accident or from a nuclear waste repository.

Radionuclide (RN) migration in natural environment is relatively complex. Natural organic matter (NOM: oxalate, acetate, humic and fulvic acid, etc.) is very diverse both in nature and concentration of possible binding groups which can significantly alter the solubility and the mobility of RN complexes [3]. Detailed characterisations of the conformation and chemical properties of NOM versus pH, redox potential, hydration state and ionic strength, and of the structure and stability of the NOM-RN complexes are needed to predict the NOM-RN affinity. Furthermore, changes in speciation with temperature may well increase the solubility of actinides under natural conditions. Hydrothermal conditions can then promote the molecular association of solution species that are fully hydrated at ambient temperature and pressure. Knowledge of the geometry of such complexes is thus essential to understand and predict changes of properties with temperature such as electrophoretic mobility, chemical reactivity in solution or toward surfaces, diffusivity in nanopores or in mineral and solid defects, and with respect to other solution species. In other respects, separation of fission products and actinides from nuclear spent fuel is currently performed by selective extraction techniques, whereby an organic ligand selectively complexes U and Pu under controlled chemical conditions and the organometallic complex is then dissolved in an extractant liquid phase. Optimisation of these RN separation techniques hinges on the resolution of key issues such as the selectivity of organic ligands with respect to a specific RN [4]. A better understanding of the electronic and co-ordination interactions between the ligand and the dissolved RN are required to increase this ligand affinity and specificity.

Specifications of the beamline

The MARS beamline will be built on the bending magnet port D03-1 of the SOLEIL storage ring. At a nominal energy of 2.75 GeV the electron beam of this new third-generation synchrotron radiation source will be characterised by a horizontal and vertical emittance of 3.7 nm.rad and 0.037 nm.rad respectively. A 1.71 T bending magnet field provides a continuous spectrum of photons with a critical energy of 8.6 keV. The machine is designed for a 500 mA maximum current distributed over 416 bunches with a beam lifetime expected to be over 15 hours [1].

The layout of MARS beamline (Figure 1) consists mainly of three hutches, the first one dedicated for the optics and the two others for the sample characterisation and the sample preparation and storage. Because of sample hazards in terms of contamination and irradiation, both of the hutches where samples will be present have been specially designed to be considered as “Listed Installation for the Protection of the Environment” (ICPE).

Figure 1. Top view of the MARS beamline located on the bending magnet port D03-1 of the synchrotron SOLEIL (Saint-Aubin, France)

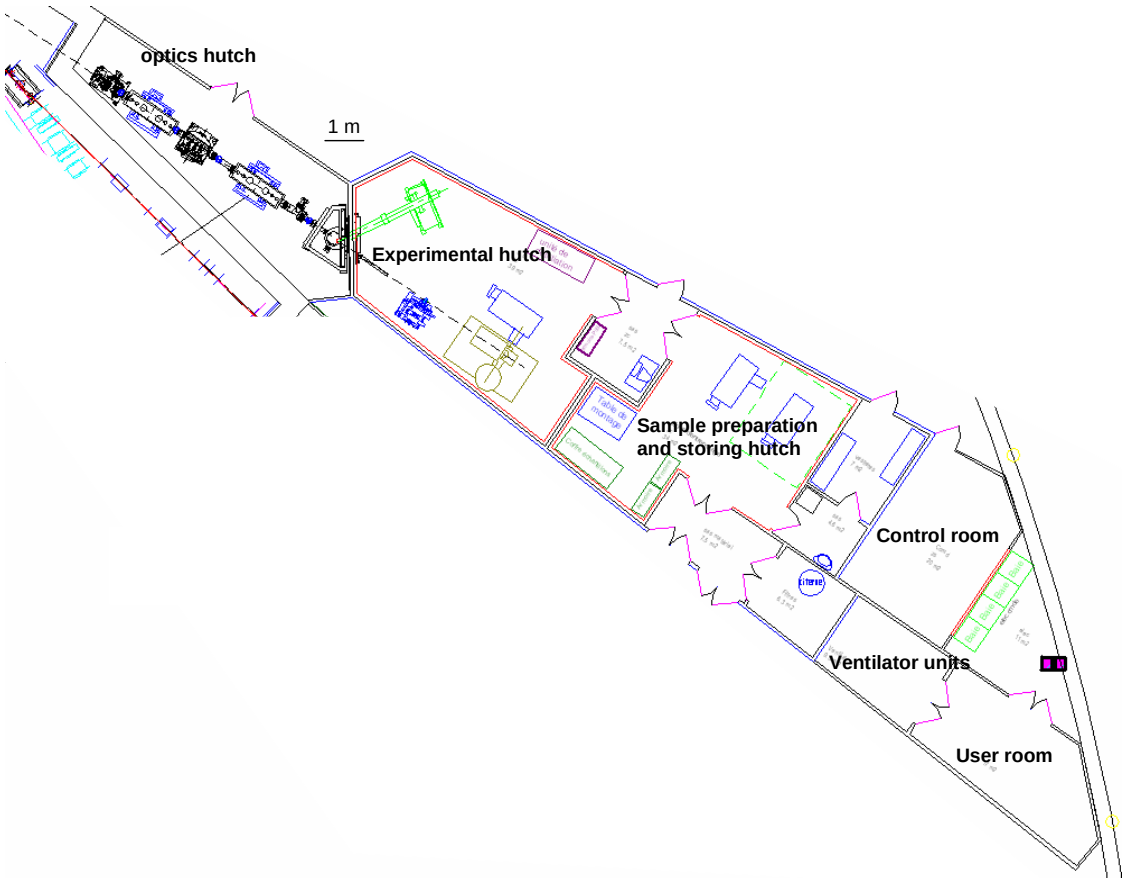

Hence, in order to maintain a dynamic confinement these hutches will be equipped with airlocks and kept at low pressure by a dedicated ventilation system. This system is characterised by two independent networks, one for the sample environments and more particularly the glove boxes and the other one for the hutches. From the experimental hall to the restricted volume inside a glove box three successive levels of decreasing pressure will be established. Very high efficiency filters located at the intake air point and at the blowers will trap radioactive material particles in case of a sample confinement

barrier failure. Pressure, temperature and radioactivity shall be continuously controlled and recorded from a specific monitoring unit. In addition, a fire-proof coating on walls and the ceiling will define two independent fire sectors with a fire resistance of two hours. To respect the loading limitations on the experimental slab, additional shielding will be limited to the volume around samples if necessary. This shielding will be calculated as function of the sample composition. In this context the hutch will be considered as the third confinement barrier, which means that holders of contaminant samples should have at least two independent airtight barriers. Considering these regulatory aspects, the fixed equivalent activity limits referred to Group 1 of radioisotopes, and are 18.5 GBq per sample and 185 GBq for the total activity stored on the beamline.

The end of the beamline which is outside the ICPE area consists of a control room, a small room for ventilator and pump units, and a user room for preparation of experiments or for the first analysis of experimental results. In order to make alignment of samples easier with respect to the X-ray beam and to avoid a large number of entrances of the ICPE area, part of control units will be duplicated inside the internal airlock which gives access to the experimental hutch.

Design of the beamline optics

The X-ray optics have been designed for performing mainly absorption spectroscopy, fluorescence measurements and diffraction characterisations with the possibility of time resolved analyses. Due to diversity of experiments, the MARS beamline has been optimised in the range of 3.5 to 35 keV with the capability for focused beams. Also, in order to extend this energy range, the layout of the beamline will integrate the possibility of carrying out some experiments at higher energy (up to 50 keV) using one of the experimental hutches of the high pressure beamline, which is set on a wiggler source.

The optical design takes into account the large demand for focused beams (sizes around $100 \times 100\ \mu m^2$) and micro-focus beams (sizes less than $10 \times 10\ \mu m^2$). Beyond the scientific interest, these focused modes on both horizontal and vertical planes provide a means to decrease the volume of analysed materials and consequently the effective dose rate from samples.

The main characteristic of MARS optics (Figure 2) is its ability to use two different alternative configurations depending on the selected elements and the nature of experiments. The main optical elements which accept a horizontal fan of 3 mrad of the bending magnet radiation are two long mirrors (M1 and M2) and two independent monochromators, a double crystal monochromator (DCM) first and a single bent crystal monochromator (SCM) downstream. Two complementary coatings are currently being considered for the reflecting surface of both M1 and M2 mirrors which must be fully water cooled because of the absorbed power in the dispersive configuration. A silicon strip will be used from 3.5 to 14 keV considering two values of the angle of incidence, 4 mrad below 10 keV and 2.2 mrad above. At higher energy and up to 35 keV, the platinum strip will be considered with a constant glancing angle of 2.2 mrad. Because of the limited length of the mirrors, the minimum glancing angle was fixed to 2 mrad in order to get reasonable photon fluxes at high energies.

The dispersive configuration will be mainly selected for time resolved experiments (ms regime) or low resolution (on consequently high flux) characterisations in the energy range of 4-22 keV. In order to operate with this configuration the DCM must be translated out the X-ray beam and the location of the M2 mirror has to be adjusted as a function of the glancing angle. The beam is then focused by the first mirror M1 and reflected by M2. Depending on the energy, the beam height is at 31.6 mm (4 mrad) or 17.4 mm (2.2 mrad) with respect to the primary beam. The energy dispersion and the horizontal focusing are achieved by Bragg reflection on the curved crystal made of Si(111) or Si(311) of the SCM.

Figure 2. Schematic representation of both configurations of MARS optics showing the main components and their respective distances from the source

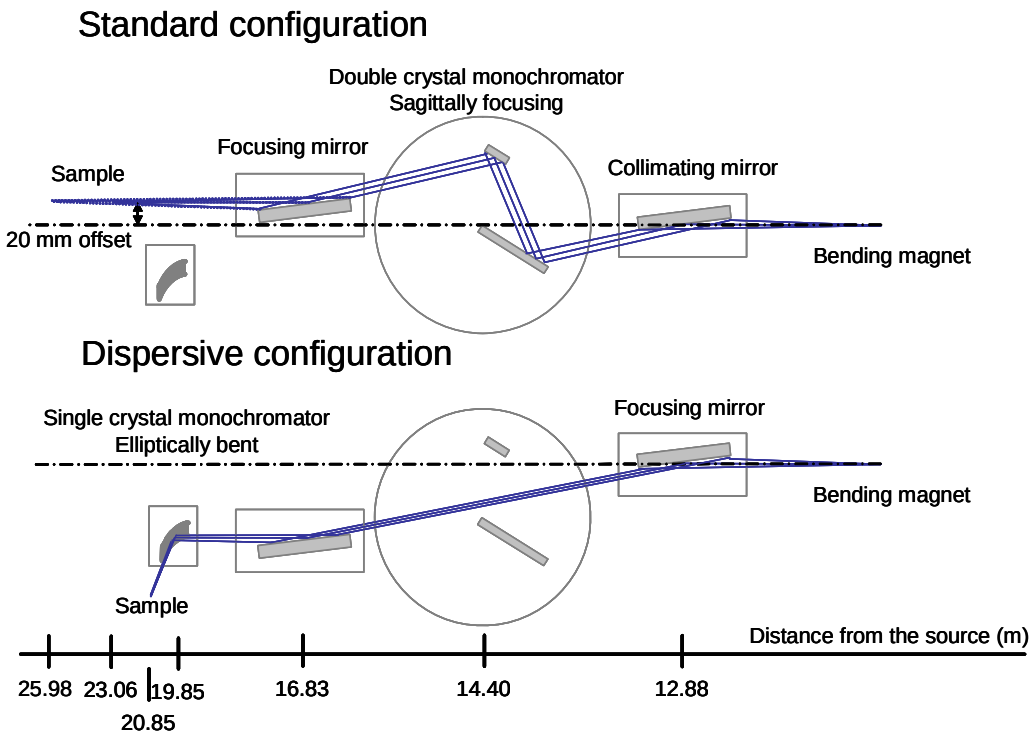

In the standard configuration the beam is firstly vertically collimated by the bent mirror M1, which also removes higher order harmonics. The vertically parallel beam from M1 then interacts with both crystals of DCM for energy selection by two successive Bragg reflections on Si(111) or Si(220) crystals. A continuous-energy scanning mode will allow adjustment of the experimental time-resolution during fast measurements and a conventional step-by-step scanning mode will yield to highest signal-to-noise ratios for slower scans. The second crystal of the DCM provides dynamical sagittal focusing by cylindrical bending. Finally the beam is reflected and focused by the mirror M2 onto the sample. This optical system gives a fixed exit beam during energy scans with a constant offset of + 20 mm with respect to the primary beam.

The flux which should be obtained from this configuration is indicated in Figure 3 for the selected energy range. This representation also shows that no significant difference is observed between the flux obtained from a Si coating and a Rh coating for the lower energy part.

In addition, micro beams with dimensions below $20 \times 20\ \mu m^2$ should be obtained by a set of crossed mirrors (Kirkpatrick-Baez geometry) located at a distance of about 3 m downstream the first focused image (around $150 \times 100\ \mu m^2$) of the X-ray source. This two-step focusing arrangement has a relatively large beam aperture with respect to the other optical solutions (Fresnel one plate or Bragg-Fresnel lens) and consequently a flux of about 2×10^{11} ph/s is expected over a beam dimension of $18\ \mu m \times 6\ \mu m$.

The ability to use both configurations alternatively (dispersive and standard) on the same beamline has required a special design of the feedthrough between the optics hutch and the experimental hutch. Hence three complementary and important elements (Figure 4) have been defined and designed from

Figure 3. Expected focused flux on the sample versus energy considering two couples of mirror surface coating

Above 21 keV, Si(111) crystals of the monochromator are replaced by Si(220) ones

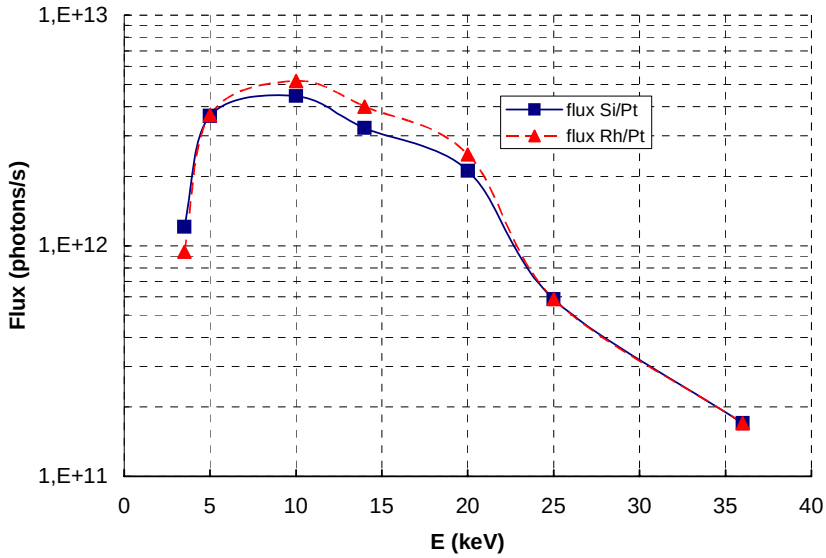

Figure 4. Safety components between the optical hutch and the experimental hutch which are specifically designed for the MARS beamline to be operational from both configurations

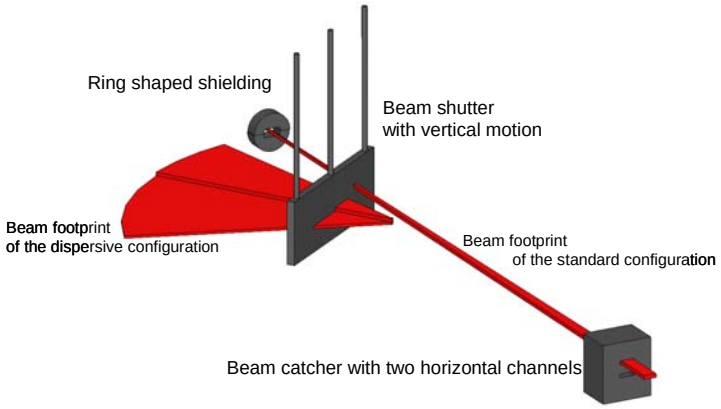

radiation calculations of the radiation attenuation. The beam catcher with both of its horizontal channels absorbs the direct beam and a large part of the bremsstrahlung radiation. In addition to the shielding wall, a large beam shutter is used to block the beam for the dispersive configuration while letting the beam impinge on the bent crystal during operations inside the experimental hutch. A ring-shaped shielding fixture on the vacuum tube is used to stop the bremsstrahlung inside this hutch when the shutter is opened.

Experimental stations

The diffraction station will be located at 23 m from the source and will be based on the use of a standard optical configuration. A robust two-circle diffractometer will be available for powder diffraction measurements. It features high resolution positioning of two coaxial rotary tables with high

loading capacities. The characteristics of the inner circle (omega) should be kept constant using sample container load up to 750 N (Figure 5). For particular studies (stress and texture measurements) an open Eulerian cradle can be mounted on the omega circle to provide two more circles. However in this case the weight and the volume of the sample holder must be greatly decreased, which constrains the studies to less radioactive materials. An ultra-high-resolution detector system based on the utilisation of a perfect crystal analyser is held by the outer table (2theta circle). It will be possible to perform quick measurements at the expense of the angular resolution by using an energy resolving Ge detector or a linear position sensitive detector coupled to Söller slits fixed on the same arm. In this case experiments will be limited to α or β emitters due to the noise coming from γ radioactive decays of samples.

Figure 5. Left, dose variations for a 3 mg irradiated steel sample after a cooling time of 1 month versus lead thickness. Right, one example of a special container designed for such a sample. The opening of the window through which the diffracted beams exit the container could be directly controlled by the external circle of the diffractometer.

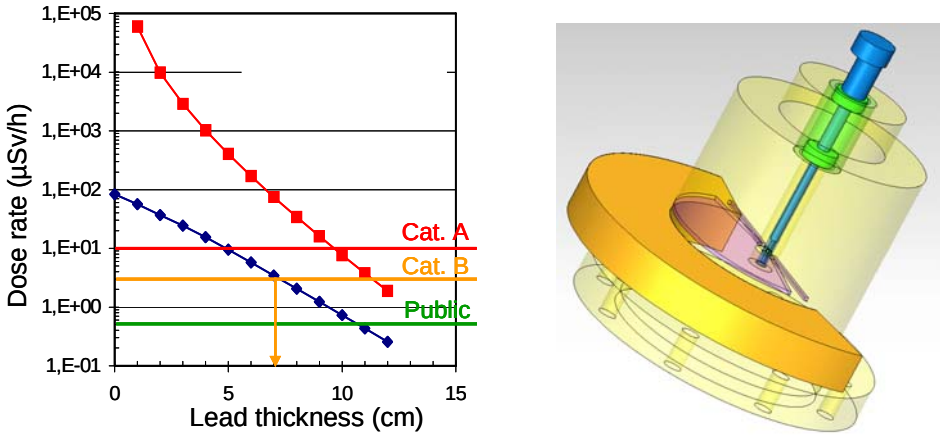

Similar to the previous station, the absorption station will be used with a standard optical configuration. The sample position will be at 26 m from the source. A general purpose X-ray absorption spectroscopy setup will be available at a distance of 3 m downstream from the diffraction station. This second station also will be equipped for X-ray fluorescence analysis. Two principal means of detection will be available, i.e. transmission mode (using photodiodes) and fluorescence mode (multi-element detector). Nevertheless, because of radioactive decays (high background) from the samples additional equipment will be necessary for optimising the signal-to-noise ratio to use special equipment such as a bent crystal Laue analyser to create a band pass filter and then removing unwanted energies (noise). Samples should be directly analysed inside either some standard sample holders or a glove box, depending on the risks estimated for the experiments (nature of samples, variations of external parameters, etc.). If necessary, measurements at low temperature could be achieved using a special cryostat with additional shielding around the sample. Moreover, different options for heating (electrical resistance or laser radiation) will be considered to develop complementary devices for high temperature experiments. Whatever the sample environment, the main difficulties will be to guarantee the sample confinement over the duration of the experiment.

The third experimental station on the MARS beamline is the dispersive station. The aim of this station is mainly to obtain complementary information from a short time resolution (typically 1 ms). For such experiments the optics will be set in the dispersive mode. The energy range on this station will be limited to 4 keV (or around 59.29° for the girder angle) and 22 keV (10.31°). In practice,

because of the minimum distance between the sample and the axis of the crystal of the SCM, XANES and EXAFS experiments will be performed above 7 or 8 keV. At lower energy only XANES measurements will be possible because of the minimum distance between the sample and the axis of the SCM crystal.

REFERENCES

[1] Synchrotron SOLEIL, *Synchrotron Rad. News*, 16, No. 5, pp. 49-56 (2003).

[2] Martin, Ph., M. Ripart, T. Petit, T. Reich, C. Hennig, F. D'Acapito, J.L. Hazeman, O. Proux, *J. Nuclear Mater.*, 312, 103 (2003).

[3] Sarret, G., A. Manceau, L. Spadini, J.C. Roux, J.L. Hazeman, Y. Saldo, L. Eybert-Berard, J.J. Menthonnex, *Environ. Sci. Technol.*, 32, 1648 (1998).

[4] Den Auwer, C., E. Simoni, S. Conradson, C. Madic, *Eur. J. Inorg. Chem.*, 21, 3843 (2003).

THE MICRO-XAS BEAMLINE AT THE SWISS LIGHT SOURCE (SLS): A NEW ANALYTICAL FACILITY SUITED FOR X-RAY MICRO-BEAM INVESTIGATIONS WITH RADIOACTIVE SAMPLES

André M. Scheidegger, Daniel Grolimund, Messaoud Harfouche, Markus Willimann, Beat Meyer, Rainer Dähn, Didier Gavillet, Michel Nicolet, Peter Heimgartner
Nuclear Energy and Safety Department (NES) Paul Scherrer Institute PSI
CH-5232 Villigen, Switzerland

Abstract

In view of the increasing awareness of the importance of the micrometer domain in many scientific fields, there has been a considerable effort to develop high resolution X-ray microprobes in the hard X-ray regime using state-of-the-art X-ray focusing devices. The microXAS beamline at the Swiss Light Source (SLS) is a microprobe facility optimised for X-ray absorption spectroscopy (XAS), X-ray fluorescence (XRF) and X-ray diffraction (XRD) experiments requiring high spatial resolution. It is designed for monochromatic and pink X-ray beams (5-20 keV) with high flux and energy resolution combined with dynamic (sub-) micron focusing capabilities. Within this manuscript, a brief description of the beamline layout is provided and a scheme on how radioactive samples can be measured at the beamline is presented.

Overview

X-ray absorption spectroscopy (XAS) and X-ray fluorescence (XRF) are key analytical techniques, not only regarding catalysis and materials science, but also as regards environmental sciences (nuclear waste management, geochemistry, soil sciences), life sciences, archeometry, and a broad range of industrial applications. In the past, "classical" XAS and XRF investigations (i.e. XAS/XRF studies with unfocused X-ray beams) have resulted in unique contributions towards an improved molecular-level understanding of material structure and chemical reactivity. Due to the small source size and low emittance of new third-generation synchrotron sources, improvements in X-ray optics and detector technology, and progress in sample positioning, it has become possible to obtain the wealth of structural information provided by XAS and XRF on a micro-scale. Highly heterogeneous samples can now be probed in a non-destructive manner with high spatial resolution and sensitivity as well as chemical specificity. In many scientific disciplines spatially resolved molecular-level information is the key to understanding fundamental physiochemical processes.

The microXAS beamline at the Swiss Light Source (SLS) is designed as a hard X-ray microprobe facility dedicated to XAS and XRF [1-3]. The microXAS beamline will further serve as the optical system for the FEMTO project. Within this project, time-resolved studies with a resolution of ~100 femto seconds will be feasible at the microXAS beamline to study time-dependent phenomena in physics, chemistry, biology and environmental science [4-6]. Finally, the beamline will allow for microXAS measurement of closed radioactive samples with micro-scale resolution. Under specially arranged conditions the Paul Scherrer Institut (PSI) will provide access to infrastructure in its "hot laboratory" facility (Type A laboratories) for preparation of samples and intermediate storage of radioactive samples.

Due to its special features (micro-focusing, open for radioactive samples, time-resolving capabilities) the microXAS beamline is of great interest for the XAS research community.

Optical layout

The microXAS beamline hosts a mini-gap in-vacuum undulator (U19) [7] which provides high-brightness X-rays in an energy range (~2.5 to ~20 keV) that covers the K- and L-edges of most transition metals and rare earth elements. The optical layout is designed to deliver a micro-focused X-ray beam with high-energy resolution ($\Delta E/E < 10^{-4}$) and is based on a vertical collimation and horizontal focusing scheme. The beamline design – including the side-deflecting mirror and resulting virtual source – has been inspired by ALS 10.3.2 [8]. By collimating the X-ray beam vertically, the transmitted energy bandwidth can be narrowed down to the Darwin width of the monochromator crystal cuts used. A horizontal focusing scheme offers the capability of dynamical focusing and optimises the overall acceptance of the optical system. At the microXAS beamline vertical collimation and horizontal focusing of the X-ray beam is achieved by means of a torroidal mirror in the optics hutch. The water-cooled Rh-coated mirror is operated in grazing incidence mode, reflects sideward (for optimal energy resolution) and produces a 1.4:1 image in the horizontal dimension.

By combining the torroidal mirror with a Kirkpatrick-Baez (KB) mirror system [9-10] which is placed in front of the sample, the design goal of a final spot size of $1 \times 1\ \mu m^2$ can be achieved, or even surpassed [2]. However, the maximised photon flux density is already reached at a beam size of $\sim 6 \times 1\ \mu m^2$. Any further reduction in spot size can be obtained by using a high-precision slit system and results in a corresponding reduction of the total photon flux.

Another important component of the optical layout is the monochromator. In order to meet the stringent requirements on the angular accuracies between the two crystals, we have chosen a double CAM design. The main advantage of a CAM system is that in order to change the Bragg angle while keeping the output beam offset fixed, it is necessary to change only one main axis motor. Therefore, the double CAM design offers good parallelism and stability when scanning over a large angular range as required for micro-beam XAS. The fixed-exit monochromator will be equipped with two fast interchangeable sets of monochromator crystals, namely Si(111) and Si(311), allowing optimisation of the experiments with respect to photon flux or energy resolution. Due to the power density impinging on the first monochromator, crystal liquid nitrogen cooling is required. For experiments requiring an even higher photon flux, the beamline can also be operated in pink beam mode using a set of filters instead of the monochromator.

In order to be able to ensure the requested beam stability and quality of the micro-beam, a number of specialised diagnostic devices are under development. Most important are fast beam position monitors (BPMs) and a high-resolution X-ray eye. The later device corresponds to a key tool during the focusing of the X-ray beam and was conceptualised in view of its utility within a proposed automated focusing routine. The BPMs are an integral part of a feedback system required to stabilise the monochromatic beam. Deviations from the zero trajectory are recorded by two BPMs, located between the monochromator and the intermediate focus point, and are converted to piezo-driven corrections executed by the second monochromator crystal. Imposed by the FEMTO project and the proposed micro-focusing scheme, the beamline has to be operated windowless up to the experimental hutch (minimisation of beam disturbance and flux reduction by windows).

Experimental infrastructure

The microXAS beamline hosts two Pb-shielded hutches (optical and experimental hutch) and a control hutch which includes the control room, a small laboratory for sample preparation and the prearrangement of *in situ* experiments, and a small room offering working space for users. A femto laboratory equipped with optical tables hosting laser systems and diagnostic tools is located adjacent to the control room.

The experimental hutch is equipped with two optical benches. The first bench hosts measurements, which do not necessarily require a micro-beam (e.g. FEMTO and *in situ* studies). The second optical bench is dedicated to micro-beam application and hosts the KB mirror pair and a motorised sample stage (translations: x, y, z; rotations: γ, θ, ω) that will allow – in addition to microXAS and XRF-mapping – for techniques such as Grazing-incidence X-ray Absorption Fine Structure (GI-XAFS) and X-ray Standing Waves (XSW). A motorised optical microscope and an X-ray eye are available for beam monitoring and sample alignment. In order to benefit from the highly brilliant X-ray beam, the detection systems available at the beamline are crucial. Energy-discriminating fluorescence detectors (a single-element Si- and a 32-element Ge-solid state detector) are of special interest for micro-beam experiments and XAS measurements of dilute samples. The high-resolution, wavelength dispersive X-ray detector system (WDX) allows resolution of overlapping fluorescence emission lines and is thus important for experiments requiring the highest energy resolution. As basic instrumentation, photodiodes or ion-chambers for transmission experiments and a Stern-Heald detector system for measurements in fluorescence and electron-yield mode are also available at the beamline. Finally, the beamline is equipped with a CCD area detector for diffraction experiments.

Micro-beam experiments with radioactive samples

A special feature of the microXAS beamline is that radioactive samples can be measured. However, since the SLS is a low-hazard, non-nuclear facility, tight regulations must be strictly observed. It is currently foreseen to declare the hutch temporarily as Zone 1 when radioactive samples are measured. In this case, a hand and foot monitor must be available at the entrance of the hutch. Furthermore, no sample manipulation will be allowed at the beamline at any time and the samples must be encapsulated (closed samples). One critical issue for experiments with radioactive samples is the fact that the dose rate will be limited to 20 microSv/week at a distance of 2 meters from the sample (hutch wall). Based on the above-mentioned restrictions, a modular and local shielding concept has been worked out in close collaboration with the safety department at PSI. In this concept, the Pb shielding is adjustable to the activity of the samples. Reviewing the proposed experiments with radioactive samples, a wide range in activity can be expected – from natural Th or U to "hot" samples containing, for example, spent fuel. Consequently, the thickness of the Pb shielding will vary. For example, in addition to the existing shielding of the experimental hutch a few cm Pb is mandatory for investigations of highly radioactive samples, while no additional shielding is required for samples containing only naturally-occurring actinides (Th, U).

The selected optical scheme at the microXAS beamline results in a working distance (available space between the end of the KB mirror box including the vacuum flange and the beam focus on the sample) which is in the order of 8 cm. Thus, the entire set-up for the measurements of radioactive samples needs to be kept as small as possible. A schematic outline of the specimen containment is given in Figure 1. The *specimen holder* consists of an air tight container holding up to three specimens which are covered with one layer of Kapton window. Kapton windows allow good transmission of the X-ray beam and ensure containment of the specimens. The *specimen holder* is encapsulated in a *safety case* which is again air tight and composed of a *massive base* and *a safety base cover*. To ensure specimens brought to the microXAS beamline are contamination free and doubly or triply (for spent fuel) encapsulated, an additional single or double layer of Kapton window is mounted on the safety

Figure 1. Outline of the radioactive specimen containment system consisting of a specimen holder, its safety case with a massive base and a safety base cover, as well as a steel cover used for transportation

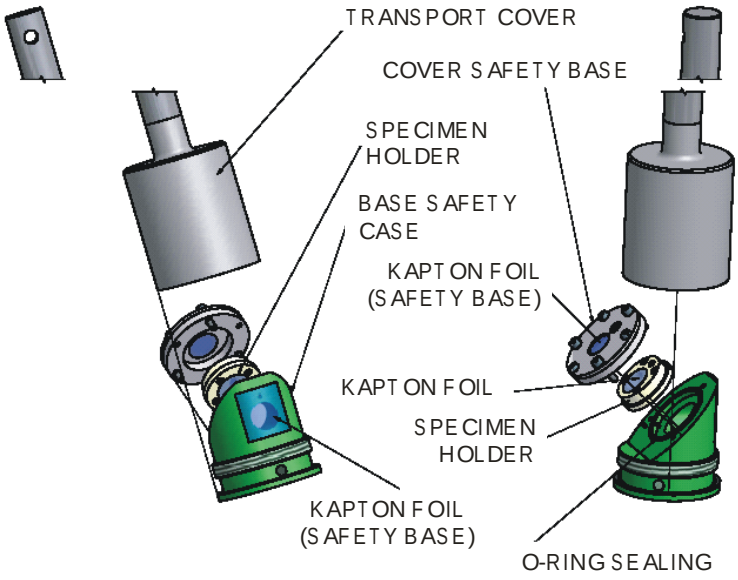

case components. The *specimen holder* allows measurements in transmission and fluorescence mode and contains a fluorescent screen that is used for beam alignment by an optical microscope. The surface of the sample should be within 1 mm of being flush with the surface of the fluorescent screen in order to avoid a significant increase of the bema size on the sample (normally a few μm^2) due to the 3 mrad divergence of the beam.

The safety case containing the specimen holder will be covered by a protective steel cover for transportation (*transport cover* – Figure 1). The specimens will be entirely encapsulated in the above outlined containment system at the "hot laboratory" at PSI. Once brought to the microXAS beamline at the SLS with a certified type transport container, the containment system is mounted on a highly precise sample manipulator dedicated for the measurements of radioactive samples. In case the activity is high enough that shielding is required, Pb shielding will be placed as close as possible horizontally around the samples. The detectors required for the experiments will then be placed above the samples and the Pb shielding. A dedicated detector portal has been designed to exchange and position the different detector system (e.g. 32-element Ge-detector for fluorescence and CCD detector for X-ray diffraction) around the containment system. For illustration, Figure 2 shows a 3-D model of the portal with a typical set-up to be used during the measurements of radioactive samples. The Ge-detector is mounted in the front rail system vertically above the samples. In the rear rail system a CCD detector is mounted and allows the monitoring of diffraction patterns. For the measurements of radioactive samples, diffraction experiments will be limited to reflection mode. Currently the details of the specimen holder and the containment system are outlined and the procedure on how to load the samples in the "hot laboratory" is finalised. Furthermore, decontamination issues, the transport procedure and the measurement protocol at the beamline are defined.

Figure 2. 3-D model of the detector portal showing the Ge-detector in vertical position for the measurements of radioactive samples

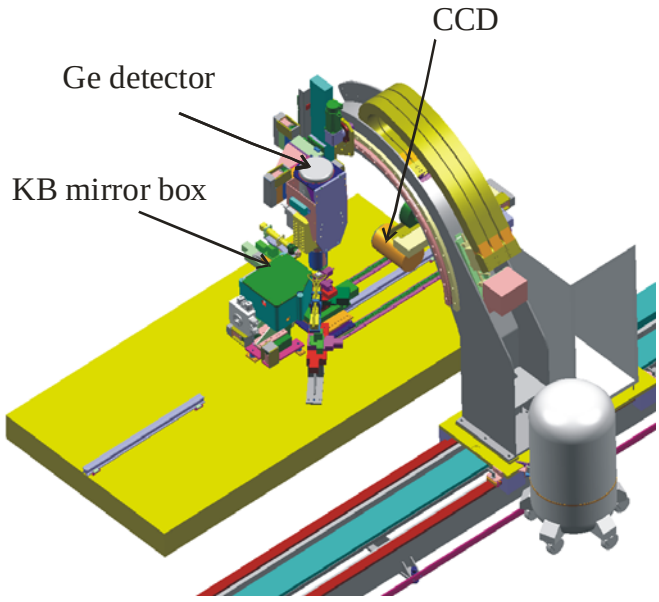

Time schedule

The first synchrotron light could be obtained in August 2004. The beamline commissioning included thorough tests of all optical and diagnostic components, the detector systems and the

micro-focusing system. The micro-XAS beamline will be opening for users in 2006. With respect to initiating the measurements of active samples at the microXAS beamline, a three-step procedure is proposed:

(i) Commissioning of the specimen holder and sample manipulator dedicated for radioactive samples using inactive samples. This phase will also be used for testing the entire experimental procedure, including transport and sample manipulation.

(ii) First experiments with weakly radioactive samples (starting summer 2006).

(iii) Step-wise extension of the measurements towards experiments with hot samples.

REFERENCES

[1] Scheidegger, A.M., R. Prins, *Joint Proposal by the Swiss XAS User Community for an EXAFS Beamline for Heterogeneous and Dilute Systems at the Swiss Light Source (SLS)*, Paul Scherrer Institute, Villigen PSI (2000).

[2] Grolimund, D., A.M. Scheidegger, J.F. van der Veen, R. Abela, "Layout of the MicroXAS Beamline at SLS", *PSI Scientific Report*, 4, 139-148 (2002).

[3] Scheidegger, A.M., D. Grolimund, B. Meyer, R. Abela, J.F. van der Veen, "Status of the MicroXAS Beamline", *PSI Scientific Report*, 7, 29-30 (2003).

[4] Schoenlein, R.W., S. Chattopadhyay, H.H.W. Chong, T.E. Glover, P.A. Heimann, C.V. Shank, A. Zholents, M. Zolotorev, *Science*, 287, 2237 (2000).

[5] Bressler, C., M. Saes, M. Chergui, D. Grolimund, R. Abela, P. Pattison, *J. Chem. Phys.*, 116, 2955 (2000).

[6] Bressler, C., M. Saes, R. Abela, D. Grolimund, S.L. Johnson, P.A. Heimann, M.Chergui, *Phys. Rev. Lett.*, 90, 47403 (2003).

[7] Schmidt, T., G. Ingold, A. Imhof, B.D. Patterson, L. Patthey, C. Quitmann, C. Schulze-Briese, R. Abela, *Nuclear Instrum. Methods A*, 467, 126 (2001).

[8] Marcus, M.A., A.A., MacDowell, R. Celestre, A. Manceau, T. Miller, H.A. Padmore, R.E. Sublett, *J. Synchrotron Radiation* 11, 239 (2004).

[9] Kirkpatrick, P., A.V. Baez, *J. Optical Society of America*, 38, 766 (1948).

[10] Yang, B.X., M. Rivers, W. Schildkamp, P.J. Eng, *Rev. Sci. Instrum.*, 66/2, 2278 (1995).

THE INE-BEAMLINE FOR ACTINIDE RESEARCH AT ANKA

Melissa A. Denecke[1], **Jörg Rothe**[1], **Kathy Dardenne**[1],
Th. Fanghänel[1], **Hubert Blank**[2], **H. Modrow**[2], **Josef Hormes**[3]
[1]Forschungzentrum Karlsruhe, Institut für Nukleare Entsorgung,
P.O. Box 3640, D-76021 Karlsruhe
[2]Universität Bonn, Physikalisches Institut, Nußallee 12, D-53115 Bonn
[3]Louisiana State University, CAMD, Baton Rouge, LA 70806

Abstract

The Institut für Nukleare Entsorgung (INE) at the Forschungszentrum Karlsruhe (FZK) Germany, has constructed, is presently commissioning, and will operate a beamline at the synchrotron source ANKA dedicated to actinide speciation investigations related to nuclear waste disposal as well as applied and basic actinide research. Experiments on non-fissile nuclides with activities up to 10^6 times the limit of exemption inside a safe and flexible containment concept will be possible. The design is for a multi-purpose beamline, i.e. a number of methods (XAFS, surface sensitive and spatial resolved techniques) are possible on the same sample, with X-ray energies from 2 472 eV (S K edge) to 23 220 eV (Rh K edge). Installation of the beamline components was completed in October 2003. Commissioning of the INE-Beamline officially began in January 2004 and the first X-ray absorption spectra were recorded the following August. Operations are targeted for 2005.

Introduction

The Institut für Nukleare Entsorgung (INE) at the Forschungszentrum Karlsruhe (FZK) Germany, has constructed, is presently commissioning, and will operate a beamline dedicated to actinide research at the FZK synchrotron source ANKA. There is presently a growing demand for synchrotron facilities, where the infrastructure, safety equipment and expertise are available for performing research on radioactive samples. One great advantage of the INE-Beamline is that the ANKA facility and INE's active laboratories are both located within the same FZK site. This symbiosis has numerous advantages, including profiting from the existing infrastructure, backed by decades of know-how. Samples can be prepared, characterised and analysed using the spectroscopic, microscopic and structural methods available at INE's active laboratories before being transported to ANKA and investigated using synchrotron-based methods at the INE-Beamline, all within a short time. The time span between sample preparation and experiment is reduced, which allows investigations of dynamic systems within a time frame of hours. The samples are also retrievable, so that sample characterisation in INE laboratories following the experiments at the INE-Beamline is possible. In addition, hazards associated with transporting radioactive samples to and from INE and nearby ANKA are minimised and the administrative requirements associated with such transports simplified.

In the following we present a discussion of the design considerations of the INE-Beamline, a short description of the ANKA facility, beamline optical components and experimental equipment available, first results of commissioning measurements made in August 2004 and a summary of the time plan for beamline operation.

INE-Beamline design considerations

The research and development at INE is largely aimed at the safety assessment of proposed deep geological repositories for high-level, heat-producing nuclear waste disposal. To ensure valid performance safety assessments, a molecular understanding of processes determinant in the fate of radionuclides, notably the actinides, is essential. To this end, the major portion of research at INE is concerned with actinide speciation, including co-ordination and redox chemistry of actinides, determination and characterisation of actinide cations sorbed onto surfaces (e.g. at the mineral/water interface) investigation of actinide containing precipitates, colloids, and secondary phases, as well as glass and spent fuel corrosion. Because actinide speciation associated with nuclear disposal concerns is manifold, the major aim at the INE-Beamline design is to ensure variability, i.e. to provide a multi-purpose station where a number of methods are possible. The methods available are standard, surface sensitive and spatially resolved methods. The standard X-ray methods [X-ray absorption fine structure (XAFS) and X-ray fluorescence (XRF)] are available and it is possible (to a limited extent) to combine XAFS with X-ray diffraction (XRD). Because many reactions of actinides in the hydro- and geo-spheres are at interfaces and junctions, emphasis at the INE-Beamline is being placed on surface sensitive techniques based on grazing incidence (GI) geometry such as GI-XAFS, X-ray reflectivity and total external reflection X-ray fluorescence analysis (TXRF). In addition, a micro-focus option will be available after a planned future upgrade to offer spatially resolved measurements. This will allow chemical state imaging (μ-XAFS), elemental mapping (μ-XRF) and identification of phases (μ-XRD).

Investigation of samples with activities up to 10^6 times the limit of exemption of non-fissile nuclides will be possible. This amount of activity will allow experiments on samples containing, e.g. more than 25 mg long-lived nuclide ^{237}Np, ^{242}Pu, ^{243}Am or ^{248}Cm. The necessary infrastructure and safety equipment is available at the INE-Beamline for active experiments. The experimental section of the radiation hutch is equipped with a special ventilation/filter system, specially sealed chicanes, easily decontaminated surfaces and a personnel lock room with a hand/foot monitor for entry and exit.

During the experiments, the samples themselves reside within two levels of containment. We have planned a flexible concept; there is no predetermined containment. The first containment is typically a sealed sample cuvette, vial or plastic bag. The second containment generally is a mechanically stable box or cylinder having sealed windows for beam entrance, transmitted beam and fluorescent beam, into which a sample or a number of samples on a sample changing stage are mounted. The windows are made of low-Z material, e.g. Kapton® or polycarbonate. A special protocol for working with radioactive samples at the INE-Beamline exists and must be adhered to. The INE-Beamline is a pooled facility of the EU European Network of Excellence for Actinide Sciences (ACTINET). A portion of annual beamtime will be available at the INE-Beamline via the standard ANKA facility proposal procedure. Experiments are also possible through co-operation with INE.

The ANKA light source and INE-Beamline location

The ANKA storage ring is operated at 2.5 GeV, with a characteristic energy of 6.0 keV, and presently with a beam current of ~200 mA. The ring is usually refilled twice a day. The beam lifetime ranges from 15-30 h. The overview of the ANKA light source with the accelerator components and the beamlines installed in the 60 × 60 m^2 experimental hall is depicted Figure 1. More information can be found at the ANKA web site (hikwww1.fzk.de/anka/maschine.html). The INE-Beamline is located at the bending magnet (BM) port designated 3.2-5 at the east side of the building. The envelope of the radiation protection hutch and the control cabin with integrated lock room bordering the experimental section of the radiation protection hutch is shown in Figure 1.

Figure 1. Overview of the ANKA light source with the main accelerator and the beamlines installed in the 60 × 60 m^2 hall

The location of the INE-Beamline (port B3.2-5) is indicated on the right. The outline of the INE-beamline hutches and cabins are shown.

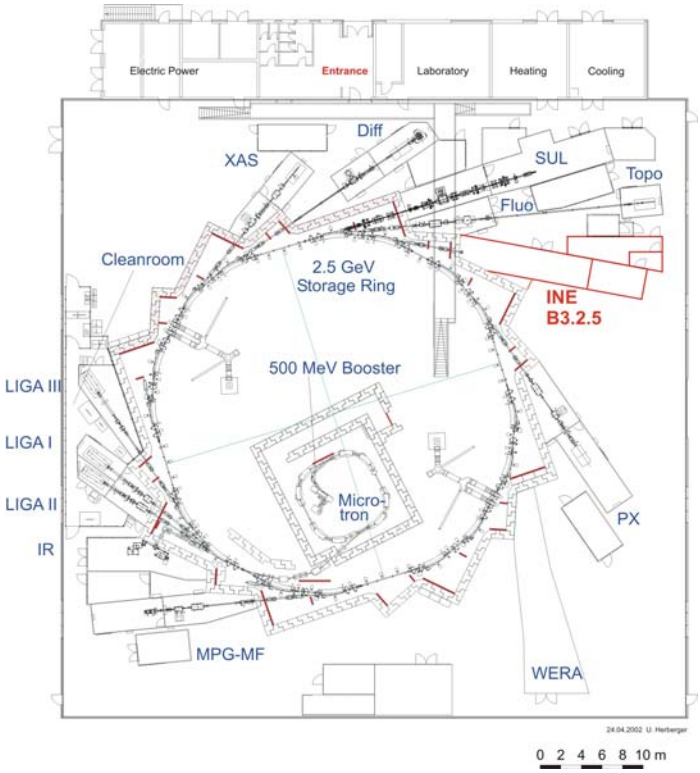

INE-Beamline optics and the experimental station

The layout of the INE-Beamline is given in Figure 2. The INE-Beamline design is optimised for X-ray spectroscopic investigations using photon energies from the K edge of S (2 472 eV) to the Rh K edge (23 220 eV). This range covers key energy regions of interest for investigations of actinides (L edges ~16-20 keV) and lanthanides as their homologues (L-edges ~5.5-11 keV). The thickness of the Be-window separating the beamline vacuum from the first mirror and ring vacuum is the determinant factor for the lower energy limit. Presently the Be window is 100 μm thick. A 50 μm window may be installed following commissioning, thereby making P K-edge experiments possible. The upper energy is limited by both the Rh coating on the mirrors and the characteristic energy of the ring. The monochromator at the INE-Beamline is a Lemonnier-type double-crystal X-ray monochromator (DCM) built at the Universität Bonn, Physikalisches Institut, with INE contributing the first crystal copper cooling block and piezo motor adjustment for detuning and feedback control to maintain constant content of harmonic radiation. The pressure inside the DCM vacuum housing is ~10^{-6} mbar and the housing only 380 mm in diameter, allowing fast changes of crystals, without long pumping times. Four pairs of crystals are presently available, Si(111), Si(311), Ge(220) and Ge(422). The DCM can also accommodate multi-layer mirrors for wide energy band-pass experiments, e.g. for XRF analysis measurements requiring higher flux.

Figure 2. INE-Beamline design layout

The beam-shutter located between optics and experimental hutch is not shown

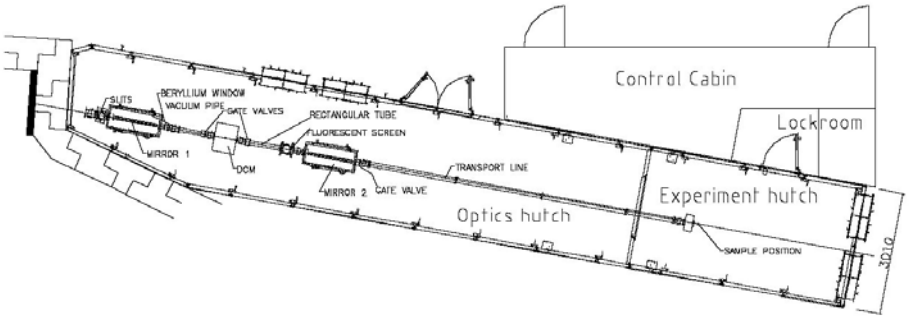

The beamline optics include collimating and focusing Rh coated silicon mirrors for a sub-mm beam dimension at the sample position. The synchrotron radiation beam is vertically collimated through the cylindrical mirror (Mirror 1) upstream from the DCM. Downstream from the DCM, the beam is focused horizontally and vertically by a toroidal mirror (Mirror 2). Mirror 2 is suspended hanging so that the beam is reflected down from its surface, in order to allow studies of liquid films. The beam focus location is in the experimental hutch at a distance of ~24 m from the BM source. There is a beam-shutter between the experimental and optics hutches, so that work can be performed in the experimental hutch without having to turn off the beam in the optics hutch, thereby keeping optical elements under a constant heat load. The distance between Mirror 2 and the beam focus is as nearly the same distance from the source to Mirror 2 as possible, thereby minimising aberration of the beam. In order to enable μ-focused spatially resolved studies, a later upgrade is planned to install an auxiliary μ-focusing optic such as a polycapillary, an elliptical monocapillary, or planar compound refractive lenses (CRL) fabricated by the Institut für Mikrostrukturtechnik (IMT) at FZK. The focal length of monocapillaries and CRL can be a number of centimetres, which is an advantage for working with radioactive samples where their containment limits the working distance between focusing optic and sample. Capillaries have the advantage for spectroscopy in that they are achromatic; no achromatic CRL is yet available, although design studies for achromatic planar CRLs are presently being conducted at IMT.

The optical tabletop in the experimental hutch is a 1.2 × 3 m^2 breadboard, large enough to accommodate almost any experimental set-up. Three ionisation chambers (HASYLAB Design, "IONIKA") and a LE-Ge five-element fluorescence detector (Canberra) are available for recording XAFS spectra in transmission and fluorescence mode. The grazing incidence equipment (HUBER Diffraktionstechnik GmbH) available at the beamline consists of two goniometer cradles with a common centre of rotation (step-size = 0.0001°), a z-stage (step-size = 40 nm) and a rotation stage (step-size = 0.0001°) as well as two micrometer-adjustable vertical slits. The goniometer cradles are for adjusting the relative incident angle of the impinging beam onto the sample surface, the z-stage for vertical height adjustment, and the rotational stage for selecting the sample surface orientation relative to the synchrotron beam polarisation vector during polarisation-dependent measurements. There is a special chamber available for performing spectroscopy measurements at lower energies.

First commissioning measurements

The first X-ray absorption spectra were recorded in August 2004 (Figures 3 and 4). The first EXAFS spectra of reference foils included a Zr foil (Figure 3). The beamline proved to be very stable at the Zr K edge energy (17.998 keV) which is near to the Pu L_3 edge (18.057 keV). The high resolution of the Ge(422) with a d value of 1.155 Å is visible in the clearly resolved features on the rising edge of the Cu K edge XANES spectrum in Figure 4. Presently, pilot experiments are being conducted (see Figure 5) and the beam profile at focus systematically studied.

Figure 3. First EXAFS spectra measured at the INE-Beamline at various energies

The available energy range (S K to Rh K) is indicated

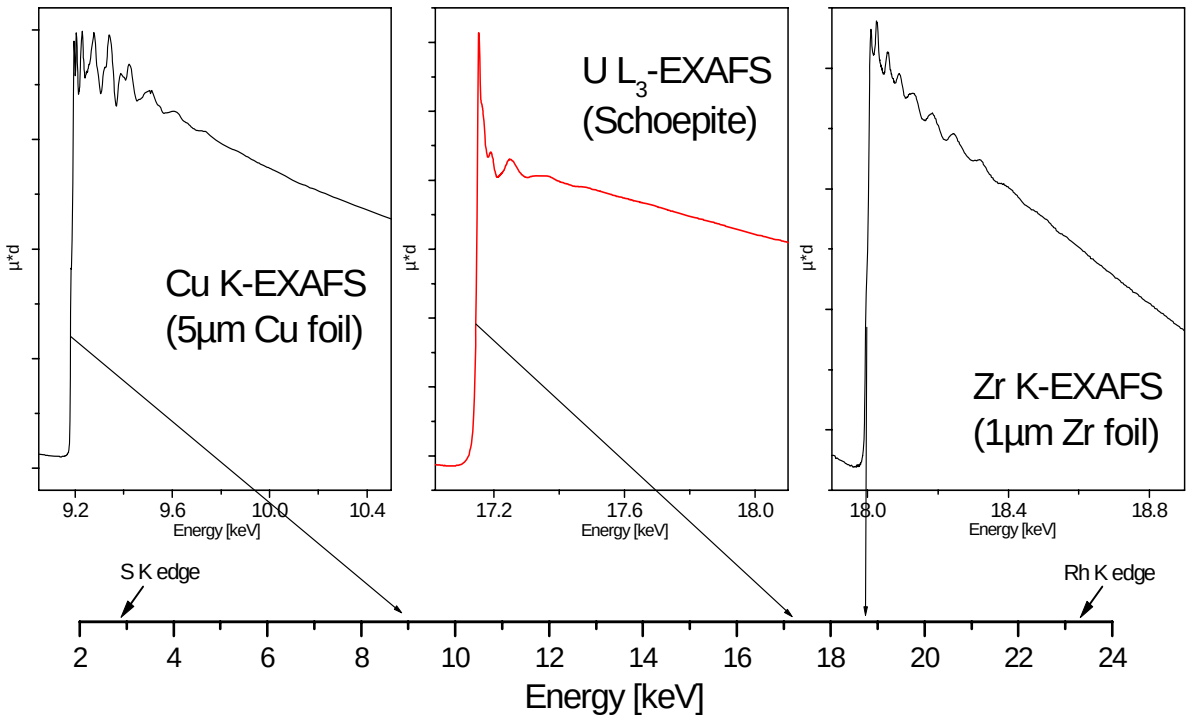

Figure 4. Cu K XANES (5 μm Cu foil) measured with Ge(422) monochromator crystals (d = 1.155 Å)

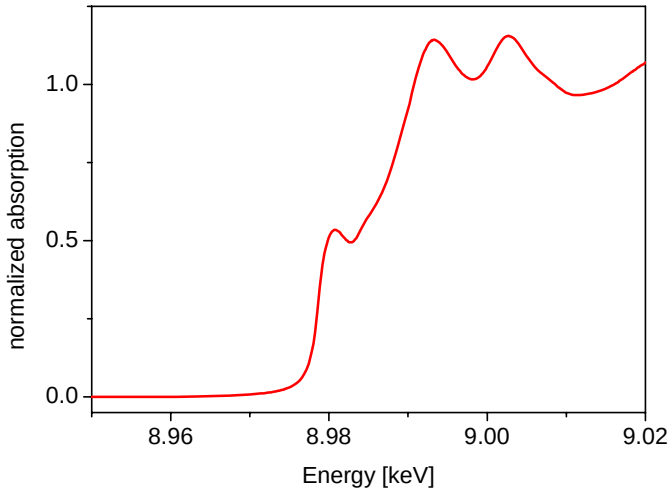

Figure 5. Zr K edge raw data (a), k^2-weighted EXAFS (b) and its Fourier transform envelope (c) of an aqueous solution of aged, microcrystalline Zr(IV) colloids < 10 nm in size recorded during one of the first pilot experiments performed at the INE-Beamline

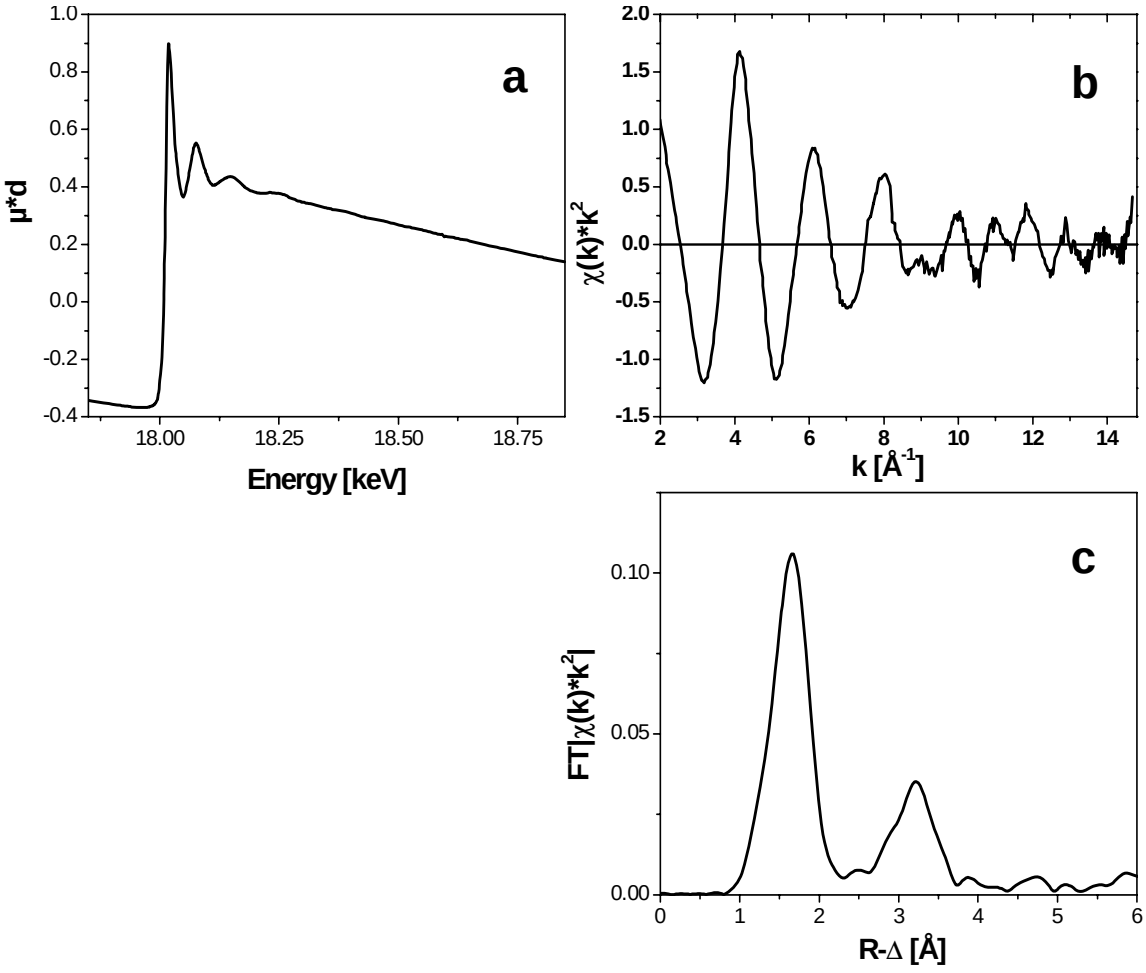

Target dates

The front end was installed in 2002. Radiation hutches were built in March 2003. The control cabin and media were installed in June/July 2003. The installation of the optic components was completed in October 2003. Commissioning of the beamline officially began in January 2004. The DCM was successfully commissioned in the spring of 2004. The INE-Beamline was issued its license to operate both of its beam shutters in May 2004. In June/July 2004 the ventilation/filter system was installed, prerequisite to licensing for handling of radioactive samples expected to be awarded sometime in the first half of 2005. Operations are targeted for 2005.

THE ROSSENDORF BEAMLINE AT ESRF: AN XAS EXPERIMENTAL STATION FOR ACTINIDE RESEARCH

Andreas C. Scheinost
The Rossendorf Beamline at ESRF, Grenoble, France

Abstract

The Rossendorf Beamline has been in full operation since 1999. Its X-ray absorption spectroscopy station dedicated to actinide research is unique in Europe, and has served for about 80 different experiments in the past four years. An overview on the current status of operation modes, technical details and access conditions is presented.

Introduction

The Rossendorf Beamline was built at the European Synchrotron Radiation Facility (ESRF) following an initiative of H. Nitsche, the former director of the Institute of Radiochemistry at the Forschungszentrum Rossendorf (FZR) near Dresden, Germany. The beamline is owned and operated by the FZR, having a collaborative research group (CRG) status at the ESRF. It consists of two experimental stations which run alternatively, one for diffraction and reflectivity experiments in materials sciences, the other for X-ray absorption spectroscopy (XAS) experiments related to radiochemistry. Only the latter is discussed here. Detailed descriptions of the beamline and the XAS end station are published [1,2]. Here, I will update that earlier information and summarise the features most important for prospective users.

The radiochemical end station of the Rossendorf Beamline was constructed to serve the main research goals of the Institute of Radiochemistry at the FZR. As these are related to the environmental behaviour of actinides and other radionuclides, the EXAFS experiments predominantly involve speciation of low concentrations of radionuclides in a large variety of media, including aqueous and non-aqueous solutions, rock minerals, clay minerals, microorganisms, plants, etc., but also combined systems like soils and sediments. This demand is supported by the EXAFS technique itself, as well as by the high brilliance of the ESRF and by special equipment at the beamline, for instance a sensitive fluorescence detector and a cryostat. The research interest as well as safety concerns of the ESRF restricted the list of radionuclides to α-emitters, hence the safety features include no shielding for γ-radiation, and the total activity is restricted to 185 MBq (see safety features below).

Optics

The beamline is located on bending magnet BM20 of the ESRF. The electron storage ring operates at 6 GeV in several modes (uniform fill, 2/3 fill, 16-bunch, single bunch) providing ring currents between 20 and 200 mA. Within the beamlines optics hutch, the white light is collimated by a mirror, converted to a monochromatic beam by a double-crystal monochromator [Si(111) or Si(311)] running either in channel-cut or fixed-exit mode, and then vertically focused by a second mirror (Figure 1). Besides collimating and focusing the beam, the two mirrors are used to reject higher

Figure 1. Schematic drawing of the beamline optics

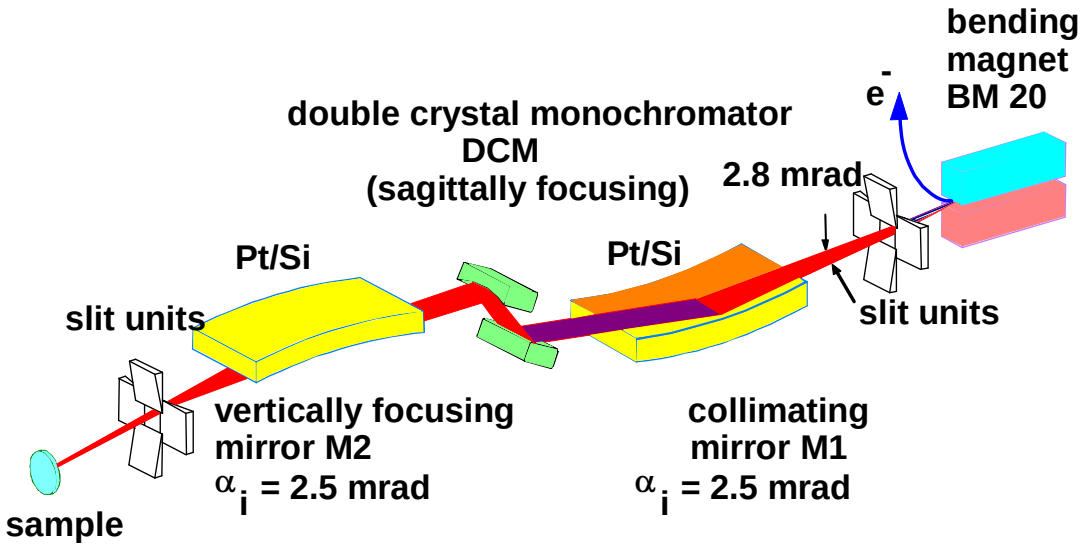

harmonics. Depending on energy range, either the Si-coated (5-13 keV) or the Pt-coated surfaces (13-35 keV) of the two mirrors are used. The integrated flux at 200 mA and 20 keV is $6 \cdot 10^{11}$ photons/s. The standard beam size for XAS is 1×10 mm^2. Using a sagitally-focusing second crystal in the monochromator, a spot-size of 0.4×0.4 mm^2 is achieved. This allows measuring small samples, often a necessity in the light of the limited radioactivity permitted at the beamline. With the energy range covered by the monochromator and the other optical components, including Be windows, the K-edges of elements Cr to Sb and the L-edges of elements Ba to Cm can be investigated (5-35 keV).

XAS technical features

For transmission XAS measurements, three gas-filled ion chambers are available. Mixtures of He, N_2 and/or Ar suited for the respective energy ranges are prepared by three software-controlled mass flow controllers.

The measurement of environmental samples with typically low concentrations of the target element in a complex matrix often results in overlapping fluorescence lines, which require special fluorescence detection techniques. At the Rossendorf Beamline, a high-throughput/high-energy resolution 13-element solid-state Ge detector (100 mm^2 LEGes) equipped with a XIA digital X-ray spectrometer (DXP-2X4T-M, 4-channel, 40 MHz, timing model) is now available. Figure 2 shows as an example the fluorescence spectra of two uranium-containing mill tailings sample, collected with low shaping time (0.25 μs), i.e. low-energy resolution and high count rate, one collected for 5 s (bottom) and the other collected for an hour (top). Even at these conditions, which are very unfavourable in terms of energy resolution, but typical for EXAFS spectroscopy of environmental samples, the energy resolution is sufficient to isolate the U-L_α from the Rb-K_α line by selecting a narrow SCA.

Figure 2. XRF of two similar uranium mill-tailing samples collected with a shaping time of 0.25 μs, and varying integration times (top: 1 hour, bottom: 5 s)

The hatched area marks the U-L_α line which produces only a shoulder on the right side of the more pronounced Rb-Kα line

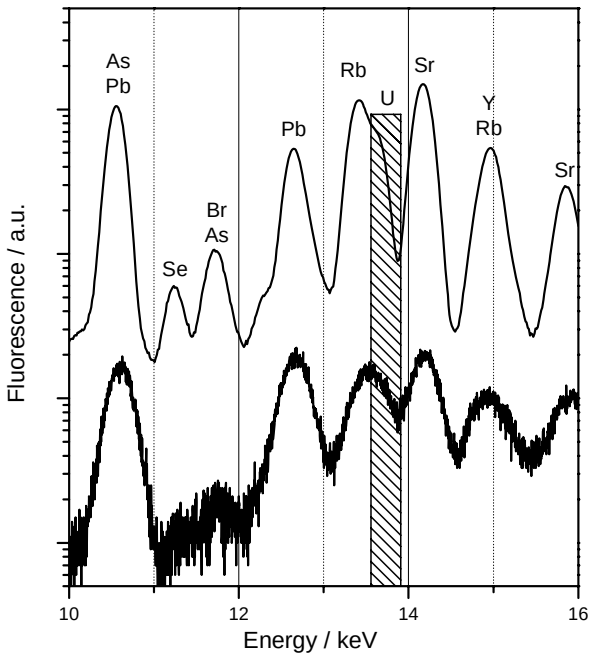

Sample cooling down to 15 K is routinely used for several reasons. First, in crystalline phases the detection of atomic shells beyond the first co-ordination sphere is greatly enhanced due to the reduction of the thermal (vibrational) component of the Debye-Waller term. An example is shown in Figure 3 for a uranyl silicate mineral. Second, cooling to cryogenic temperatures greatly reduces the risk that biological or other organic samples are "fried-up" by the intense X-ray beam. Third, redox processes are inhibited, which is especially important when measuring actinides with several labile oxidation states. Finally, measuring samples at a range of temperatures allows investigation of temperature-dependant structural effects.

Figure 3. EXAFS spectrum of soddyite collected at 295 K (hatched lines) and at 30 K (solid lines)

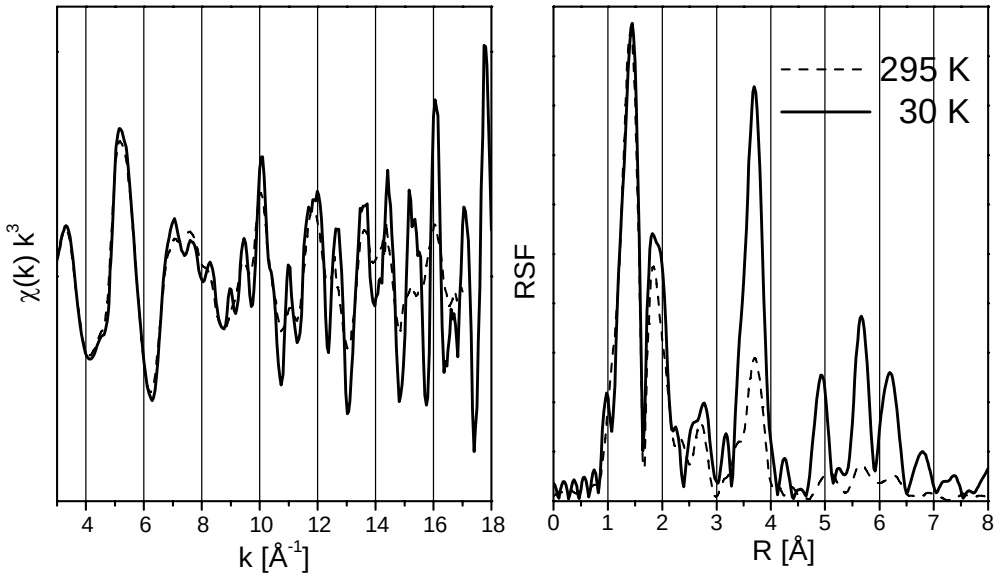

Redox control of aqueous and ionic liquids is possible by employing a spectro-electrochemical cell, which was specifically designed to suit the safety demands of the ESRF and prevents release of hydrogen gas by using second-order anode reactions [3]. Furthermore, a uniaxial goniometer is available to investigate the polarisation dependency of structures and to cancel the unwanted preferred orientation of particles within a sample by the magic angle technique.

Radiochemical safety features

The XAS experimental station is fully equipped and has the proper licenses to run a list of presently 18 radionuclides with a maximum of 185 MBq (Table 1). It is expected that ^{243}Cm will be added to this list in early 2005.

The technical safety features are adjusted to handle predominantly α-emitting radionuclides. The central safety equipment is a glove box with negative pressure gradient towards the experimental hutch (which in turn has a negative gradient towards the ESRF hall). The ventilation system encompasses air filters and α-, β- and γ-radiation monitor systems, with all components backed up by a parallel system in case of component failure (redundancy principle) [4]. The monochromatic X-ray beam enters and leaves the glove box through Kapton bay-windows which are placed at the back side of the glove box. Detection of fluorescence radiation is possible through a third, large (80 mm diameter) Kapton window. Due to arrangement, the samples remain inside the glove box during an experiment; X-ray transmission and fluorescence detectors, filters, calibration foils and additional slit systems remain outside.

Table 1. List of approved radionuclides

Nuclide	Max amount [g]	Exemption [Bq]	Half-life [y]	Specific activity [Bq/g]
^{99}Tc (β-)	29.1	$5\cdot10^{6}$	$2.1\cdot10^{5}$	$6.4\cdot10^{8}$
^{208}Po (α)	$8\cdot10^{-6}$	0	2.898	$2.2\cdot10^{13}$
^{209}Po (α)	$3\cdot10^{-4}$	0	102	$6.2\cdot10^{11}$
^{226}Ra (α)	$5\cdot10^{-3}$	$5\cdot10^{3}$	1 600	$3.7\cdot10^{10}$
^{nat}Th (α)	1 000	$5\cdot10^{4}$	$1.4\cdot10^{10}$	$8.2\cdot10^{3}$
^{231}Pa (α)	0.106	$5\cdot10^{3}$	$3.28\cdot10^{4}$	$1.7\cdot10^{9}$
^{nat}U (α)	1 000	$5\cdot10^{6}$	$4.47\cdot10^{9}$	$2.6\cdot10^{4}$
^{237}Np (α)	6.97	$5\cdot10^{5}$	$2.1\cdot10^{6}$	$2.6\cdot10^{7}$
^{238}Pu (α)	$2.9\cdot10^{-4}$	$5\cdot10^{3}$	87.7	$6.3\cdot10^{11}$
^{239}Pu (α)	0.08	$5\cdot10^{3}$	$2.411\cdot10^{4}$	$2.3\cdot10^{9}$
^{240}Pu (α)	0.022	$5\cdot10^{3}$	6563	$8.4\cdot10^{9}$
^{241}Pu (α)	$4.9\cdot10^{-5}$	$5\cdot10^{3}$	14.35	$3.8\cdot10^{12}$
^{242}Pu (α)	1.24	$5\cdot10^{3}$	$3.735\cdot10^{5}$	$1.5\cdot10^{8}$
^{241}Am (α)	$1.4\cdot10^{-3}$	$5\cdot10^{3}$	432.2	$1.3\cdot10^{11}$
^{243}Am (α)	$25\cdot10^{-3}$	$5\cdot10^{3}$	7 365	$7.4\cdot10^{9}$
^{244}Cm (α)	$6.2\cdot10^{-5}$	$5\cdot10^{3}$	18.1	$3.0\cdot10^{12}$
^{246}Cm (α)	0.017	$5\cdot10^{3}$	4 750	$1.1\cdot10^{10}$
^{248}Cm (α)	1.156	$5\cdot10^{3}$	$3.39\cdot10^{5}$	$1.6\cdot10^{8}$

All samples have to be placed inside double-confinement sample holders. Due to this enclosure, which has to be maintained at all times, sample intervention is restricted to modification of temperature (15-300 K with the cryostat) of redox potential (with the closed-system electrochemical cell) and in some rare cases of pH (injection of acids or caustics through a septic membrane).

A variety of holders for liquids, wet pastes, dry powders and pressed pellets, approved by the ESRF safety group for room or cryo-temperatures is available. A detailed description of these sample holders together with technical drawings may be downloaded from the beamline home page (http://www.esrf.fr/exp_facilities/BM20).

The samples are mounted in fully-automated sample stages. For room-temperature measurements, up to eight samples can be mounted and measured without any user intervention. A uniaxial goniometer allows to rotate the eight-fold sample holder towards the polarisation vector of the X-ray beam. For measurements at temperatures down to 15 K, a single sample is placed into a closed-cycle He cryostat, which is mounted inside the glove box. A new cryostat with larger exit window and larger sample chamber will be available in mid-2005. With this new cryostat the 13-element fluorescence detector will be illuminated more evenly even at the small sample-to-detector distances often required for dilute samples. Furthermore, two to three small samples may be placed inside the cryostat to reduce sample exchange time and user intervention.

Data analysis

Besides standard data reduction and analysis tools (FEFF8, IFEFFIT, EXAFSPAK, WinXAS, Six-pack) we provide advanced statistical tools like iterative transformation factor analysis [5,6] and

Monte Carlo simulations [7]. These methods greatly improve the detection, quantification and structural analysis of species from samples, which contain several species simultaneously. Furthermore, a wavelet analysis tool improves the analysis of the scattering amplitude distribution and hence the discrimination of atoms [8]. Finally, under certain (very restrictive) circumstances, X-ray diffraction data may be collected in the neighbouring materials science hutch in addition to EXAFS spectra. Software is available to refine structures using both the XRD and the EXAFS information simultaneously [9].

Spectra collected at the beamline are stored in a database for easy retrieval. A combined database and spectral analysis tool is currently under development, which will allow to search for spectra based on similarity. This tool will simplify the identification of the species in ill-defined samples by comparison with spectra of well-characterised samples.

Modes of access

Due to the CRG status of the Rossendorf Beamline at the ESRF, users may apply for beamtime in two different ways. Two-thirds of the beamtime at the radiochemistry station, corresponding to about 200 eight-hour shifts or 67 days per year, are in-house beamtime for the FZR. Outside users have access to this beamtime by collaboration with scientists of the FZR. Applications for beamtime are accepted any time by submitting an application form to the acting head of the radiochemistry station (see http://www.esrf.fr/exp_facilities/BM20). Beamtime will be scheduled after acceptance of the proposal, usually within four months.

One-third of the beamtime (100 shifts or 33 days) is managed by the ESRF. Accordingly, proposals have to be submitted to the ESRF. Deadlines are March 1 and September 1. The proposals are evaluated by the scientific advisory committee of the ESRF. In case of approval, beamtime is scheduled by the beamline personnel, usually between 6 and 12 months after the proposal deadlines. For ESRF experiments, travel and accommodation expenses are reimbursed by the ESRF. For a detailed user guide please visit the ESRF home page (www.esrf.fr).

All radioactive samples for both types of access mode have to delivered, stored and handled according to the safety regulations agreed upon with ESRF. It is recommended to contact the beamline personnel at least two months in advance of the scheduled experiment to discuss sample preparation, transport, and measurement procedures. If an experiment is labelled “red” by the ESRF Safety Group (generally experiments involving Np, Pu, Am, Cm samples) two persons must be present at the beamline, 24 hours a day. These experimentalists have to be provided by the user group.

REFERENCES

[1] Matz, W., N. Schell, G. Bernhard, F. Prokert, T. Reich, J. Claussner, W. Oehme, R. Schlenk, S. Dienel, H. Funke, F. Eichhorn, M. Betzl, D. Prohl, U. Strauch, G. Huttig, H. Krug, W. Neumann, V. Brendler, P. Reichel, M.A. Denecke and H. Nitsche, *J. Synchrotron Radiation*, 6, 1076 (1999).

[2] Reich, T., G. Bernhard, G. Geipel, H. Funke, C. Hennig, A. Rossberg, W. Matz, N. Schell and H. Nitsche, *Radiochimica Acta*, 88, 633 (2000).

[3] Hennig, C., J. Tutschku, A. Rossberg, A.C. Scheinost and G. Bernhard, these proceedings (2006).

[4] Funke, H., G. Bernhard, J. Claussner, K. Jansen, W. Matz, H. Nitsche, W. Oehme, T. Reich and D. Rollig, *Kerntechnik*, 66, 195 (2001).

[5] Roßberg, A., T. Reich and G. Bernhard, *Anal. Bioanal. Chem.*, 376, 631 (2003).

[6] Scheinost, A.C., A. Rossberg, S. Pfister, R. Kretzschmar and M. Marcus, *Physica Acta*, in press (2004).

[7] Rossberg, A. and A.C. Scheinost, *Physica Acta*, in press (2004).

[8] Funke, H., M. Chukalina and A. Rossberg, *Physica Scripta*, in press (2004).

[9] Hennig, C., T. Reich, W. Kraus, G. Reck, F. Prokert and N. Schell, *Physica Scripta*, in press (2004).

Poster Session

Chair: D.K. Shuh

XAFS ANALYSIS OF LANTHANIDE SPECIES ADSORBED ON PYRIDINE RESIN: ADSORPTION MECHANISM OF LANTHANIDES (ACTINIDES) BY PYRIDINE RESIN

Atsushi Ikeda[1,2], **Tsuyoshi Yaita**[1], **Shinichi Suzuki**[1],
Takaumi Kimura[1], **Tatsuya Suzuki**[2], **Yasuhiko Fujii**[2]
[1]Department of Materials Science, Japan Atomic Energy Research Institute, Japan
[2]Research Laboratory for Nuclear Reactors, Tokyo Institute of Technology, Japan

Abstract

Chemical species of lanthanide (Ln(III)) ions adsorbed on a pyridine resin have been investigated by X-ray absorption fine structure (XAFS) spectroscopy in order to elucidate the adsorption mechanism of trivalent actinides (An(III)) and Ln(III) on the pyridine resin. The Ln-L_{III} edge EXAFS spectra measured and their Fourier transforms indicate that the Ln(III) species adsorbed as chloro complexes, while Ln(III) ions are tightly hydrated by water molecules in the solution phase. From these results, a possible adsorption mechanism by the pyridine resin is discussed herein.

Introduction

The separation of trivalent actinides [An(III)] and lanthanides [Ln(III)] is one of the most important processes for the partitioning and transmutation strategy [1] for reducing high-level radioactive wastes (HLW) produced from the reprocessing of nuclear spent fuels. However, it is well-known that the chemical properties, such as oxidation state or ionic radius, of An(III) and Ln(III) are similar, giving rise to a difficulty in their separation. We have recently developed a novel separation technique using a tertiary pyridine type resin for the separation of An(III) and Ln(III) [2-5]. In this separation system, An(III) and Ln(III) are chromatographically separated due to the difference of their adsorbability on the pyridine resin, that is, An(III) are adsorbed on the resin more strongly than Ln(III), with the result that An(III) are eluted from the resin column more slowly than Ln(III).

In order to improve this separation technique for practical purposes, we need to understand the adsorption and separation mechanisms of An(III) and Ln(III) by the pyridine resin to optimise solvent compositions. In this study, the chemical speciation of Ln(III) adsorbed on the pyridine resin was carried out by using Extended X-ray Absorption Fine Structure (EXAFS) spectroscopy. The results are compared with those obtained in a solution phase, and the adsorption and separation mechanisms are discussed from these results.

Experimental

Sample preparation

Solution samples for XAFS measurements were prepared by dissolving hydrated Ln(III) chlorides ($LnCl_3 \cdot nH_2O$, 99.9%-purity) into a desired methanolic hydrochloric acid solution, which is used for the above-mentioned chromatographic separation using the pyridine resin, or de-ionised water. The concentration of Ln(III) in the sample solutions was adjusted at 0.1 mol/L. All the chemicals used in this study were reagent grade. The Ln chloride compounds were supplied by Rare Metallic Co., Ltd., Japan and other chemicals were supplied by Wako Pure Chemical Ind., Ltd., Japan.

The resin used in this study was a tertiary pyridine type resin and it was synthesised by the co-polymeriaation of vinylpyridine (90 vol.%) and divinylbenzene (10 vol.%). The porosity of the resin was 40 vol.%. This pyridine resin was mixed with the solution sample prepared as mentioned above and the mixture was shaken for 20 h at 283 K. Then the mixture was filtrated and the resin separated from the solution was doubly sealed in a polyethylene bag and used for XAFS measurements. This resin sample was still wet and it retained the solvent in the porous structure of their resin matrix in large quantities. This resin sample is called a “wet sample” in this study to distinguish from the dried resin samples that follow. After the measurements, the wet sample was dried at 293 K for two hours and then for one day. These two different samples of dried resin are designated “dried sample” and “well-dried sample”, respectively. The dried resin samples were also doubly sealed in a polyethylene bag and used for XAFS measurements.

XAFS measurement and data treatment

Ln-L_{III} edge XAFS spectra were collected at the beam line BL-27B of Photon Factory (2.5 GeV, 350-400 mA), High-Energy Accelerator Organization (KEK) using a Si(111) monochromater. All the solution samples were measured in a transmission mode using ion chambers which are filled with nitrogen gas and 50 vol.% nitrogen/50 vol.% argon gas for monitoring the intensities of incident and transmitted X-rays, respectively. On the other hand, the resin samples were measured in a fluorescence

mode using a seven-element solid-state detector. All the measurements were performed at room temperature. The incident flux from the synchrotron was reduced to 60-70% of its maximum at around adsorption edges to remove the effect of higher-order harmonics.

The XAFS data were reduced and fitted with theoretical EXAFS curves using the program package WinXAS Ver. 3.1 [6]. The theoretical EXAFS parameters, i.e. phase shifts and back-scattering amplitudes were calculated by the program FEFF 8.00 [7]. The EXAFS scattering paths were generated from the single scatterings of Ln-O and Ln-Cl calculated by the same program. Structural parameters [co-ordination number (N), interatomic distance (R), Debye-Waller factor (σ^2)] were obtained from the curve fitting in k-space. The amplitude reduction factors, S_0^2, were fixed at 0.9 for all the curve fittings for raising the precision of other parameters. The shifts in threshold energy, ΔE_0, were allowed to vary from -10 to 10 eV for each fitting, but it was held constant for all co-ordination shells.

Results and discussion

Figure 1 shows the L_{III}-edge k^3-weighted EXAFS spectra of Nd(III) in de-ionised water, 50 vol.%-concentrated HCl and 50 vol.%-methanol mixture, and in the pyridine resin for three different samples (wet, dried and well-dried samples), respectively. Figure 2 shows their corresponding Fourier transforms (FTs), and the structural parameters obtained from curve fittings are listed in Table 1. The EXAFS data for solution samples indicate that Nd(III) ions are tightly hydrated by 9~10 water molecules in de-ionised water and this aqua-complex is maintained even in a very extreme solvent of 50 vol.%-concentrated HCl and 50 vol.%-methanol mixture. On the other hand, the k^3-weighted EXAFS spectra for resin samples gradually changed their oscillation patterns, especially after the fourth oscillation, and the first peaks of their FTs shifted to longer distance as the resin was dried.

Figure 1. Nd L_{III}-edge k^3-weighted EXAFS spectra for Nd^{3+} in de-ionised water, concentrated HCl and methanol mixture, and adsorbed in pyridine resin

(• • •) experimental data, (——) theoretical fit

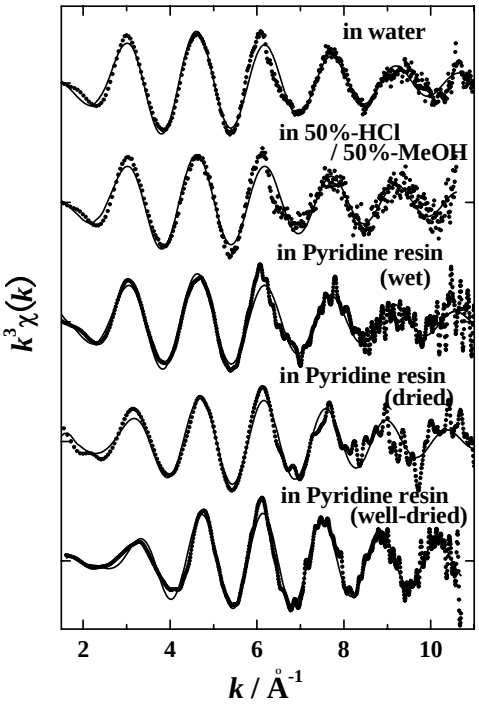

Figure 2. Fourier transforms of the Nd L_{III}-edge k^3-weighted EXAFS spectra in Figure 1

Phase shifts are not corrected

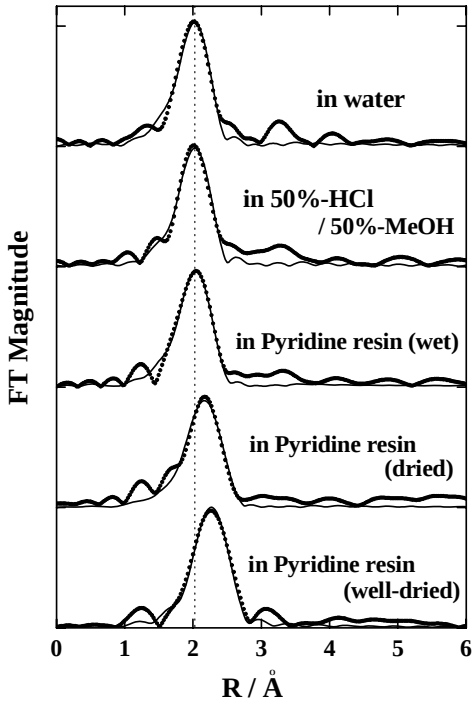

Table 1. Structural parameters obtained from the curve-fittings of Nd L_{III}-edge EXAFS spectra

Error: R ± 0.01 Å, N ± 15%, Debye-Waller factors (σ^2): 0.001 ~ 0.008 Å^2

	Ln-O(H_2O)		Ln-Cl			
Sample	**R/Å**	**N**	**R/Å**	**N**	***k*-range**	**ΔE_0/eV**
Water	2.50	9.7			1.5-11	5.0
50%-HCl/50%-MeOH	2.49	9.5			1.5-10.5	5.7
Pyridine resin (wet)	2.50	9.3	2.77	0.4	1.5-11	4.9
Pyridine resin (dried)	2.51	4.4	2.75	3.7	1.5-11	5.8
Pyridine resin (well-dried)	2.50	0.4	2.74	6.5	1.5-10.5	5.7
14 M-LiCl by XAFS [8]	2.51	7.8	2.85	1.9		
10 M-HCl by XRD [9]	2.41	6~8	2.78	0~2		

As mentioned in *Sample preparation* section above, the pyridine resin used in this study has 40 vol.% of micro- and macropores in its structure, like a sponge. The wet resin sample still retained a large quantity of solvent inside. Therefore, we consider that most of the EXAFS signals from the wet sample derive from the Nd(III) ions in the solvent inhaled in the pore-structure of the resin, not from those adsorbed on pyridine functional sites of the resin. The FT and structural parameters obtained from the curve fitting for the wet sample indicate that the Nd(III) ions existed in the interstitial solvent inside of the resin matrix are hydrated by nine water molecules, holding the same aqua-complex as that observed in the solution phase. However, the interstitial solvent existed in the resin matrix is removed by drying the resin. Consequently, the EXAFS signals from a well-dried sample are considered as the signals for the Nd(III) ions adsorbed on the resin, although the signals from a dried sample still include the information from the solution phase because the sample is not dried completely and it still

has some interstitial solvent left in the pores. The FTs and structural parameters for the well-dried sample indicates that the dehydration of Nd(III) ions occurs and the Cl^- co-ordination is strongly enhanced when the cations are adsorbed on the resin, forming chloro complexes in the resin phase. The dried sample shows the intermediate spectrum and values between those for the solution sample and for the well-dried sample, implying that the results contain the information both for the solution phase and for the resin phase.

Figures 3 and 4 show the L_{III}-edge k^3-weighted EXAFS spectra and corresponding FTs of Gd(III) and Er(III) ions for solution and well-dried resin samples. The FTs and structural parameters in Table 2 indicate that Gd(III) ions also form chloro complexes in the resin phase, while they are tightly hydrated by water molecules in the solution phase. However, Er(III) ions show no dehydration and Cl^- co-ordination even in the resin phase, persisting their aqua-complexes.

Figure 5 shows the distribution coefficients (K_d) of Nd(III), Gd(III) and Er(III) ions for the pyridine resin in the mixed solvent of 50 vol.%-concentrated HCl and 50 vol.%-methanol, along with the N_{Cl} in the resin phase. The K_d and N_{Cl} show a similar decreasing tendency as the atomic numbers increase. This means that the adsorptivity of Ln(III) ions for pyridine resin is affected by the degree of their Cl^- complexations. Allen, *et al.* [8] has reported that the Cl^- complexation of An(III) is stronger than that of Ln(III). Therefore, we can expect that An(III) ions can form chloro complexes in the resin phase more easily than Ln(III) ions, bringing the larger adsorptivity of An(III) over Ln(III) [2,3]. The pyridine groups of the resin are protonated in acidic solution [12] so that they can behave as weakly basic anion exchange sites. If the pyridine resin works as an anion exchange resin, the adsorptivity of metal cations

Figure 3. Gd and Er L_{III}-edge k^3-weighted EXAFS spectra for Ln^{3+} in de-ionised water, concentrated HCl and methanol mixture, and adsorbed in pyridine resin

(• • •) experimental data, (——) theoretical fit

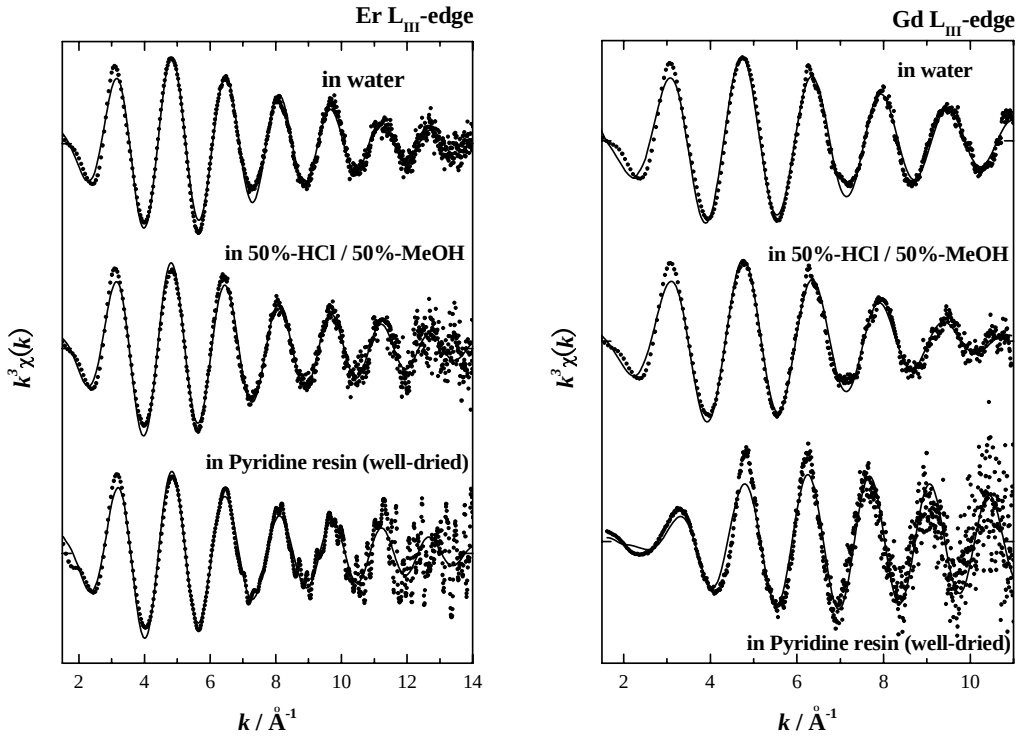

Figure 4. Fourier transforms of the Gd and Er L_{III}-edge k^3-weighted EXAFS spectra in Figure 3

Phase shifts are not corrected

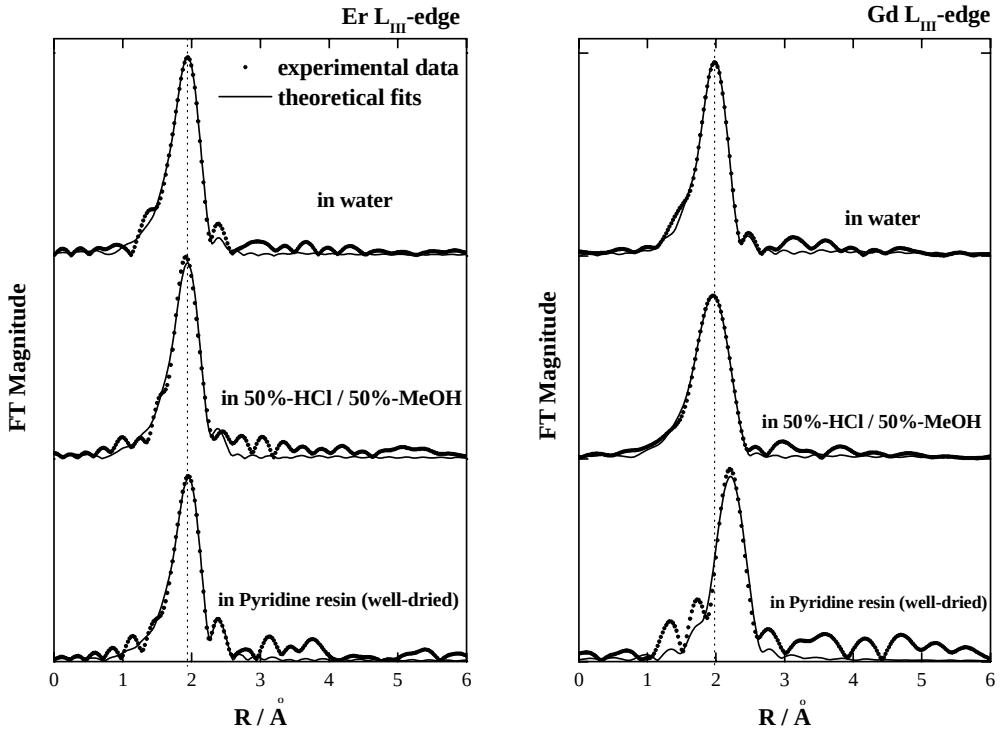

Table 2. Structural parameters obtained from the curve fittings of Gd(III) and Er(III) L_{III}-edge EXAFS spectra

Error: R ± 0.01 Å, N ± 15%, Debye-Waller factors (σ^2): 0.003 ~ 0.009 Å^2

		Ln-O (H_2O)		Ln-Cl			
Metal	**Sample**	**R/Å**	**N**	**R/Å**	**N**	***k*-range**	**ΔE_0/eV**
Gd	Water	2.41	8.9			1.5-11	
	50% HCl/50% MeOH	2.41	8.8			1.5-11	
	Pyridine resin (well-dried)			2.66	4.8	1.5-11	
	10 M-HCl by XRD [10]	2.37	6~8	2.80	0~3		
Er	Water	2.35	8.7			1.5-14	3.97
	50% HCl/50% MeOH	2.36	8.0	2.74	0.4	1.5-14	2.92
	Pyridine resin (well-dried)	2.35	7.2	2.73	0.4	1.5-14	4.49
	10 M-$ErCl_3$, solution by XRD [11]	2.37	8.2				

Figure 5. Variation of distribution coefficients (K_d) of Ln(III) in pyridine resin and Cl^- co-ordination numbers (N_{Cl}) and Ln(III) cations adsorbed in pyridine resin in 50 vol.% concentrated HCl and 50 vol.% methanol mixed solvent

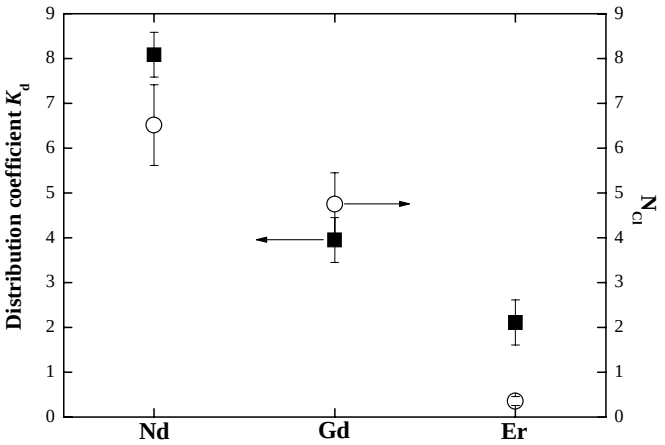

for the resin is dominated by the degree of their Cl^- complexation. However, pyridine groups can also co-ordinate to An(III) and Ln(III) ions directly, forming metal-pyridine complexes [13-15]. We did not have any evidence of pyridine co-ordination in the resin phase in this study. But we still need to consider the possibility of direct co-ordination of pyridine groups because the pyridine resin can adsorb An(III) and Ln(III) ions even in a LiCl solution, in which the pyridine groups are hardly protonated and the resin cannot behave as an anion exchange resin [3]. Further study is required for the detailed interpretation of the adsorption mechanism by pyridine resin.

Summary

An L_{III}-edge EXAFS analysis of Ln(III) ions in several solutions and in the pyridine resin showed that Ln(III) ions were strongly hydrated by water molecules even in a extreme solvent of concentrated HCl and methanol mixture, while the hydrated water molecules were removed and chloro complexes was formed in the pyridine resin phase. The co-ordination of Cl^- in the resin phase was more enhanced for lighter Ln(III) than for heavier ones. The co-ordination number of Cl^- in the resin phase seems to have some relationship with the distribution coefficients of Ln(III) for the pyridine resin.

REFERENCES

[1] Chwaszczewski, S., B. Słowiński, *Appl. Energy*, 75, 87 (2003).

[2] Suzuki, T., M. Aida, Y. Ban, Y. Fujii, M. Hara, T. Mitsugashira, *J. Radioanal. Nucl. Chem.*, 255, 581 (2003).

[3] Ikeda, A., T. Suzuki, M. Aida, K. Ohtake, Y. Fujii, K. Itoh, M. Hara, T. Mitsugashira, *J. Alloys Compd.*, 374, 245 (2004).

[4] Ikeda, A., T. Suzuki, M. Aida, Y. Fujii, K. Itoh, T. Mitsugashira, M. Hara, M. Ozawa, *J. Chromatog. A*, 1041, 195 (2004).

[5] Ikeda, A., T. Suzuki, M. Aida, K. Otake, Y. Fujii, K. Itoh, T. Mitsugashira, M. Hara, M. Ozawa, *J. Nucl. Sci. Technol.*, 41, 915 (2004).

[6] Ressler, T., *J. Synchrotron Rad.*, 5, 118 (1998).

[7] Rehr, J.J., J. Mustre de Leon, S.I. Zabinsky, R.C. Albers, *J. Am. Chem. Soc*., 113, 5135 (1991).

[8] Allen, P.G., J.J. Bucher, D.K. Shuh, N.M. Edelstein, I. Craig, *Inorg. Chem.*, 39, 595 (2000).

[9] Steele, M.L., D.L. Wertz, *Inorg. Chem.*, 16, 1225 (1977).

[10] Steele, M.L., D.L. Wertz, *J. Am. Chem. Soc.*, 98, 4424 (1976).

[11] Habenschuss, A., F.H. Spedding, *J. Chem. Phys.*, 70, 2797 (1979).

[12] Kapinos, L.E., H. Sigel, *Inorg. Chim. Acta*, 337, 131 (2002).

[13] Jensen, M.P., L.R. Morss, J.V. Beitz, D.D. Ensor, *J. Alloys Compd.*, 303-304, 137 (2000).

[14] Rivière, C., M. Nierlich, M. Ephritikhine, C. Madic, *Inorg. Chem.*, 40, 4428 (2001).

[15] van Staveren, D.R., G.A. van Albada, J.G. Haasnoot, H. Kooijman, A.M.M. Lanfredi, P.J. Nieuwenhuizen, A.L. Spek, F. Ugozzoli, T. Weyhermüller, J. Reedijk, *Inorg. Chim. Acta*, 315, 163 (2001).

SORPTION OF Am(III) ONTO 6-LINE-FERRIHYDRITE AND ITS ALTERATION PRODUCTS: INVESTIGATIONS BY EXAFS

Silvia Stumpf[1], Thorsten Stumpf[1], Thomas Fanghänel[1], Kathy Dardenne[1], Christoph Hennig[2], Reinhardt Klenze[1]
[1]Forschungszentrum Karlsruhe, Institut für Nukleare Entsorgung
PO Box 3640, D-76021, Karlsruhe, Germany
[2]Forschungszentrum Rossendorf, ROBL-CRG, European Synchroton Radiation Facility
BP 220, F-38043, Grenoble, France

Abstract

The sorption of Am(III) onto 6-line-ferrihydrite at different pH values is studied using X-ray absorption spectroscopy (XAS). Am(III) sorbs onto ferrihydrite by formation of a bidentate (corner-sharing) at pH 5.5 (Am-O 2.48 Å, Am-Fe 3.70 Å) and pH 8.0 (Am-O 2.48 Å, Am-Fe 3.69 Å). IR and TEM measurements indicate the transformation of 6-line-ferrihydrite into goethite and hematite for both pH values during the heating of the ferrihydrite suspension at 85°C for 67 days. While Am(III) is released during the transformation at pH 5.5, it is incorporated in a goethite-like structure at pH 8.0 (Am-O 2.46 Å, Am-Fe 3.32 Å, Am-Fe 3.59 Å). XANES spectra confirm these results.

Introduction

For the long-term performance assessment of nuclear waste repositories, knowledge about the interactions of actinide ions with mineral surfaces is imperative. The mobility of released radionuclides is strongly dependent on the sorption/desorption processes at mineral surfaces and on their incorporation into the mineral structure.

Iron oxides can occur as corrosion products and naturally as sediment coating or colloids [1]. Due to its high specific area (200-800 m^2/g) [2,3], very small amounts of the amorphous 6-line-ferrihydrite (6LFh) can strongly influence the migration behaviour of metal ions. This property of Fh combined with its omnipresence confers to this amorphous metastable iron phase the possibility to play an important role in the retardation of radionuclides, in particular actinides, in the near-field as well as in the far-field of a nuclear waste repository.

Extended X-ray absorption fine structure (EXAFS) investigations of Cu, Pb and Zn sorption onto Fh show the formation of bidentate inner-sphere complexes at the mineral surface [4,5]. For the sorption of Lu onto Fh the formation of mono- and bidentate surface complexes is dependent on pH [6]. Fh is a metastable phase and converts to crystalline goethite and/or hematite. The relative proportion of both the crystalline phases depends on experimental conditions such as pH value, temperature or concentration of metal ions [7] during the Fh transformation. To accelerate the alteration under laboratory conditions the temperature is increased to 85°C. A pH decrease during the transformation process is reported in the literature [8]. Moreover, the transformation of the Fh phase affects the sorption behaviour of different metal ions. Whereas Cu, Mn and Ni are strongly attached to the surface, Pb and Cd are released during the transformation process [9,10]. In the case of Al it is incorporated into the crystal lattice [11]. The incorporation of the trivalent lanthanide Lu into a hematite-like structure lattice during the Fh transformation is reported in the literature [12].

This study aims to understand and determine the importance of Fh as a sorbent in the near field as well as in the far field of a nuclear waste repository. The influence of the Fh transformation on the speciation of the adsorbed Am(III) is studied at different pH values using XAS spectroscopy.

EXAFS measurements

Americium L_3 edge EXAFS spectra were recorded at the European Synchrotron Radiation Facility (ESRF) operating at 6 GeV with a maximal current of 200 mA, at the Rossendorf Beamline (ROBL) [13]. The double-crystal monochromator was equipped with a pair of Si(111) crystals. Two Pt-coated mirrors were used to reject higher harmonics. The radioactive samples were sealed with polyethylene foils and put into containers out of lead with two windows for the excitation and emission radiation. All measurements were performed at room temperature. The samples were measured in fluorescence mode using a four-pixel Ge detector with a sample orientation of 45° to the incident beam. The energy was calibrated by assigning the first inflection point at the K-edge absorption spectrum of a Zr metal foil to 17 998 eV [14]. The data were analysed using standard procedures [15] and software packages like the EXAFSPAK program for the sorption of Am(III) onto ferrihydrite [16]. The data of the transformation experiment were analysed using WINXAS97 [17] for extracting $\chi(k)$ from the absorption spectrum. The fit to the data was carried out in the R space (1.5 to 4.0 Å) using the FEFFIT program of the UWXAFS package [18]. The k-space range was set from 2.7 to 10.3 $Å^{-1}$ (3.3 to 8.2 $Å^{-1}$ for Am(III) sorption on iron coating). Theoretical backscattering amplitude and phase functions for fitting the experimental data were calculated with the FEFF8 [19] code. The overall scaling factor, S_0^2, was held constant to 1.

Results and discussion

Sorption of Am(III) onto 6-line-ferrihydrite at pH 5.5 and pH 8.0

The sorption of 1×10^{-3} mol/L Am(III) (^{243}Am; $t_{1/2}$ = 7 370 years) onto 6LFh (preparation: Schwertmann and Cornell [20]) was investigated by EXAFS measurements at pH 5.5 and pH 8.0. The fit to the EXAFS data yields an Am-O distance of 2.48 ± 0.02 Å at both pH values and similar Am-Fe distances of 3.69 ± 0.02 Å (Table 1).

Table 1. Results from fits to the EXAFS data shown in Figure 3

Sample	Shell	R [Å][a]	N[b]	σ^2 [Å^2][c]	ΔE_0 [eV][d,e]
Am/Ferrihydrite pH 5.5	Am-O Am-Fe	2.480(5) 3.70(2)	6.3(9) 1.0*	0.0084 0.0046	-2.73[d] 5.47[e]
Am/Ferrihydrite pH 8.0	Am-O Am-Fe	2.478(3) 3.69(2)	6.1(5) 1.0*	0.0086 0.0112	-2.73[d] 5.47[e]
Am/Goethite pH 5.5 after Fh transformation	Am-O Am-Fe	2.478(3) 3.75(3)	7.2(6) 0.3(1)	0.0079 0.0020*	-2.73[d] 5.47[e]
Sample	**Shell**	**R [Å][a]**	**N[b]**	**σ^2 [Å^2][c]**	**ΔE_0 [eV][d,e]**
Am/Goethite pH 8.0 after Fh transformation	Am-O Am-Fe Am-Fe	2.466(4) 3.59(1) 3.32(1)	4.1(4) 4.4(8) 1.4(3)	0.0081 0.0200* 0.0108	-2.73[d] 2.28 2.28

Standard deviation in parentheses, [a] ± 0.02 Å, [b] ± 20%, [c] Debye-Waller-Factor, * fixed value, [d] correlated value for the four samples and [e] correlated value for three samples.

The EXAFS results suggest that the Am(III) is adsorbed onto the mineral surface of Fh by formation of a bidentate surface complex at pH 5.5 and pH 8.0. The proposed structure for the complex shown in Figure 1 is deduced from the structural parameters obtained from the fit (Table 1). The Am-Fe distance found matches the expected distances for a corner-sharing bidendate surface complex.

Figure 1. Structural model of the Am(III) sorption species onto 6-line-ferrihydrite at pH 5.5 and pH 8.0

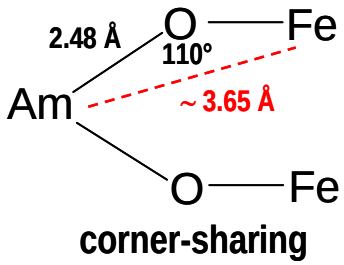

Transformation of ferrihydrite at pH 5.5 and pH 8.0

In view of the characterisation of the transformation of Fh in presence of Am(III) at 85°C for 67 days into the crystalline phases goethite and hematite, samples including the non-radioactive analogue Eu(III) were prepared and treated in the same way and then analysed by IR (Figure 2) and TEM measurements. It was not possible to quantify the different mineral phases by these methods.

Figure 2. IR spectra of ferrihydrite samples at pH 5.5 and pH 8.0 a) before and b) after transformation

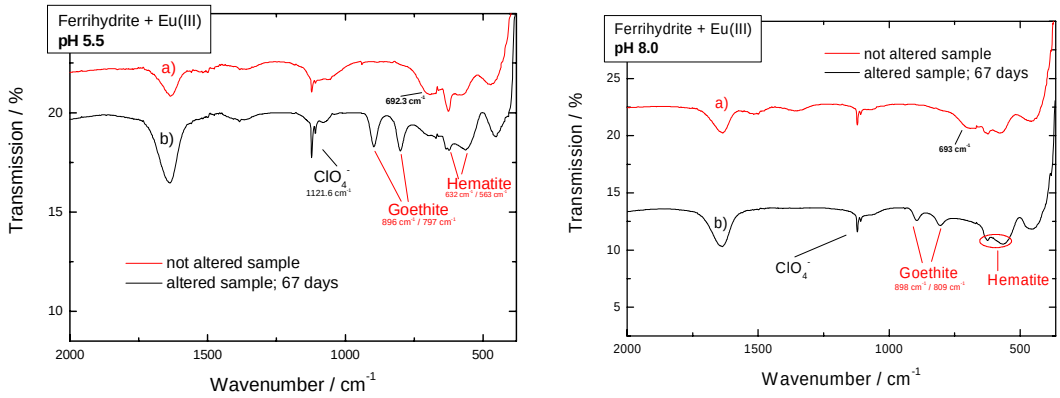

Figure 3 shows a comparison of the EXAFS and Fourier transformed (FT) spectra of the sorption and altered samples at pH 5.5 and pH 8.0. The structural parameters obtained from the fit to the EXAFS data are listed in Table 1. The amplitude of the main Am-O oscillation increases in the transformed sample at pH 5.5 while the amplitude of the Am-Fe oscillation observable in the k-range from 7.0 $Å^{-1}$ to 7.5 $Å^{-1}$ and 9.0 $Å^{-1}$ to 10.5 $Å^{-1}$ is reduced. This is more evident in the FT spectra on the right part of Figure 3. The intensity of the oxygen FT peak increases for the altered sample while the iron FT peak intensity is strongly reduced. The fit results show that the number of O co-ordinating ligands at 2.18 Å increases from 6.3 to 7.2 for the transformation sample while the co-ordination number of Fe neighbouring the Am decreases from 1 to 0.3 (Table 1). The Am-Fe distance becomes slightly longer in the transformed sample but still lies in the expected range for bidentate corner-sharing sorption complex. This surprising result can be explained by the release of Am during the transformation of the ferrihydrite. Indeed during the transformation, the pH of the solution decreases and a significant amount of the Am(III) can desorb and remain in the solution as aquo-species. A previous study [6] with Lu has shown that 48% of the initially sorbed Lu onto ferrihydrite is released during the transformation at pH 6. Due to the fact that the sample is investigated without prior separation of the aqueous phase, we measure a mixture containing a large part of aquo-species with nine water molecules in the first co-ordination sphere (2.48 Å) and no Fe neighbour. As the Am-O distance of the sorbed species and the aquo ion is the same, the EXAFS spectrum of the transformed sample at pH 5.5 does not show any structural change compared to the spectrum of the sorption sample at pH 5.5. The EXAFS spectra of the sorption and transformed sample at pH 8.0 show a significant difference in both the fine structure and amplitude (Figure 3, bottom).

We observe a broadening of the EXAFS oscillation for the transformation sample particularly visible in the k-range from 7.0 $Å^{-1}$ to 7.5 $Å^{-1}$. We can also note a splitting of the oscillation between 9.0 $Å^{-1}$ and 10.5 $Å^{-1}$ indicating an Am-Fe interaction. The fraction of oxygen in the FT spectrum of the transformation sample at pH 8.0 is strongly reduced. This can be explained by the reduction of the number of co-ordinated oxygen ligands during the transformation. Co-ordination by 6 oxygen ligands would be comparable to a replacement of octahedral co-ordinated Fe(III) in the mineral frame. Contrary to the pH 5.5 sample, the XANES spectra of the pH 8.0 sample given in Figure 4 show pronounced differences in the position of the multiple scattering features around 18 550 eV. The energy shift of the scattering resonance allows the calculation of the distance between Am and the O atoms in the first co-ordination sphere.

Figure 3. Am/ferrihydrite interaction at pH 5.5 and pH 8.0 before and after transformation

Left: k^3-weighted Am L_3 edge experimental EXAFS results; right: corresponding Fourier transformed spectra

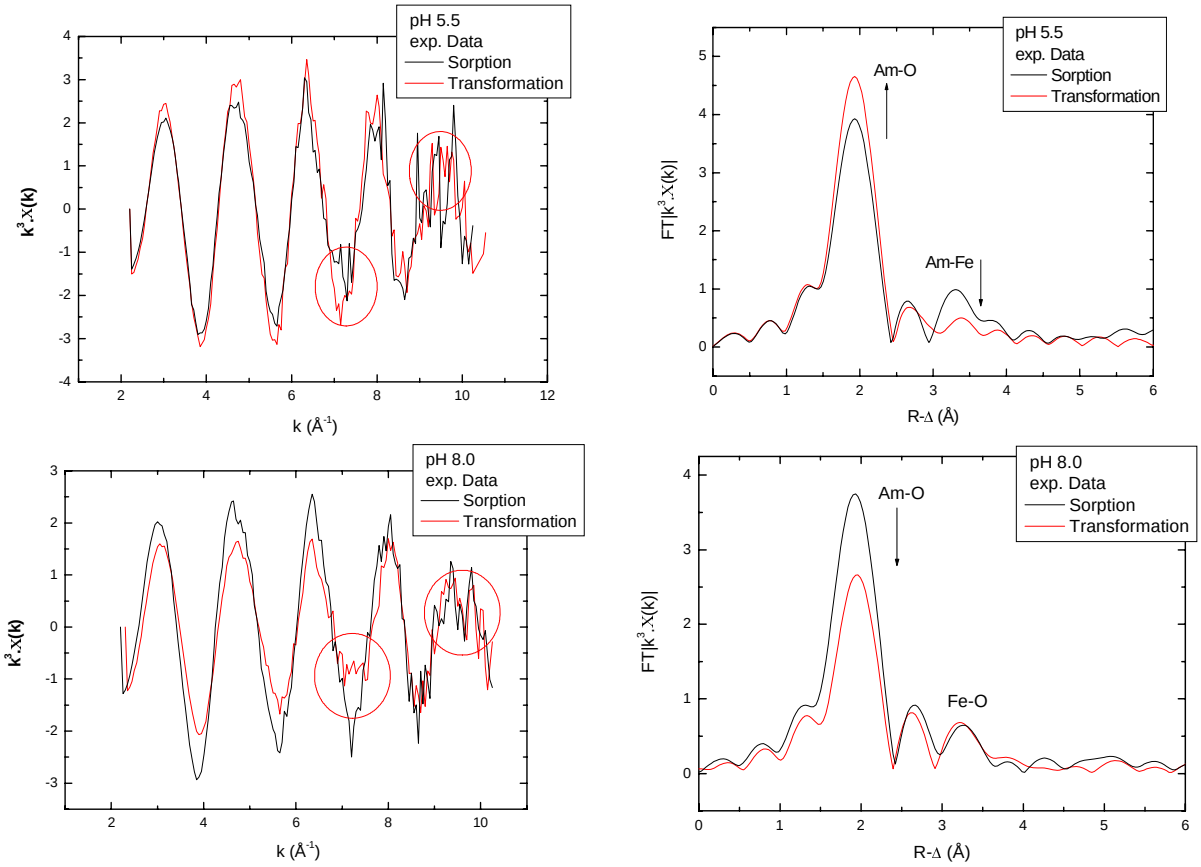

Figure 4. XANES spectra: comparison of the Am_{L3} edge of the ferrihydrite samples at pH 8.0 before and after transformation

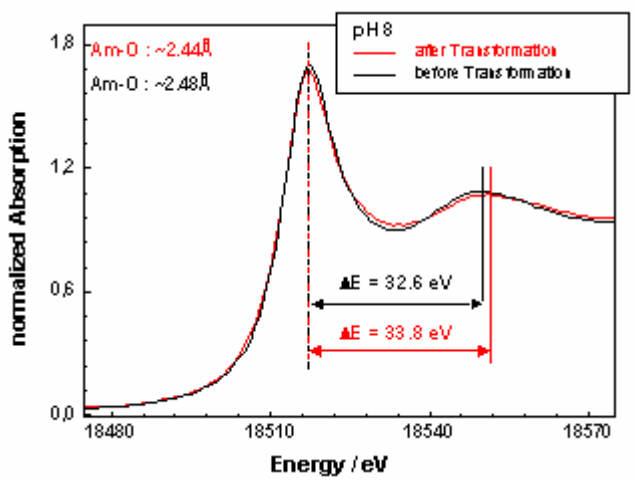

The scattering resonance shift is related to the bond distance by [21]:

$$\Delta E * R^2 = C \quad (1)$$

C is a constant determined by using known compounds with known bond distances. From literature data [22] we obtain a value of 201 ± 4 eV*Å^2.

After transformation the scattering resonance around 18 550 eV is shifted by 1.2 eV which corresponds to an Am-O bond of 2.44 Å, i.e. 0.04 Å shorter than for the sorption sample (2.48 Å). A shortening of the mean bond distance indicates a reduction of the co-ordination number according to the bond valence theory [23,24]. This indicates a possible incorporation of Am(III) into the iron mineral phase during transformation at pH 8.0. In this case, shorter Am-Fe distances are expected because of a stronger Am-Fe interaction. The fit to the EXAFS data yields Am-Fe distances of 3.32 and 3.59 Å. In the literature two models for the incorporation of lutetium into transformed Fh are described [25]. For Lu incorporation into a goethite-like structure, three Lu-Fe distances with values of ~3.04 Å, ~3.24 Å and ~3.45 Å are expected, whereas incorporation into a hematite-like structure would yield bond distances of ~3.08 Å, ~3.41 Å and ~3.88 Å. If we take into account the difference of ionic radii between Lu^{3+} (0.86 Å) and Am^{3+} (0.97 Å) we can estimate that the distance for Am would be ~0.11 Å longer than the one for Lu. This gives Am-Fe distances of ca. 3.15 Å, 3.35 Å and 3.56 Å for incorporation of Am(III) into goethite and ca. 3.19 Å, 3.52 Å and 3.99 Å for the incorporation into hematite. The obtained values of 3.32 Å and 3.59 Å suggest the incorporation of Am(III) in a goethite-like structure during the transformation of ferrihydrite at pH 8.0.

Conclusion

The interaction of Am(III) with iron mineral surfaces was investigated by EXAFS spectroscopy. At low pH values (pH 5.5) as well as at higher pH values (pH 8.0) Am(III) sorbs as a bidentate corner sharing species onto the surface. Upon heating, Fh is transformed into goethite and hematite as shown by TEM and IR measurements. The results of the fit to the EXAFS data indicate the release of sorbed Am(III) at pH 5.5 during the transformation and suggest the incorporation of Am into a goethite-like structure at pH 8.0. The analysis of the XANES spectra is in good agreement with these results.

REFERENCES

[1] Dario, M., A. Ledin, *Chem. Spec. Bioavail.*, 9/1, 3 (1997).

[2] Janney, D.E., J.M. Cowley, P.R. Buseck, *Clays and Clay Minerals*, 48/1, 111 (2000).

[3] Cornell, R.M., U. Schwertmann, *The Iron Oxides: Structure, Properties, Reactions, Occurrence and Uses*,VCH Verlagsgesellschaft, Weinheim (1996).

[4] Scheinost, A.C., S. Abend, K.I. Pandya, D.L. Sparks, *Environ. Sci .Technol.*, 35, 1090 (2001).

[5] Waychunas, G.A., C.C. Fuller, J.A. Davis, *Geochim. Cosmochim. Acta*, 66/7, 1119 (2002).

[6] Dardenne, K., T. Schäfer, M.A. Denecke, R. Rothe, J.I. Kim, J.I., *Radiochim. Acta*, 89, 469 (2001).

[7] Martínez, C.E., S. Sauvé, A. Jacobson, M.B. McBride, *Environ. Sci. Technol.*, 33, 2016 (1999).

[8] Schwertmann, U., J. Friedl, H. Stanjek, D.G. Schulze, *Clays and Clay Min.*, 48/2 (2000).

[9] Ford, R.G., P.M. Bertsch, K.J. Farley, *Environ. Sci. Technol.*, 31, 2028 (1997).

[10] Karthikeyan, K.G., H.A. Elliott, F.S. Cannon, *Environ. Sci. Technol.*, 31, 2721 (1997).

[11] Lewis, D.G., U. Schwertmann, *Clays and Clay Min.*, 27/3, 195 (1979).

[12] Dardenne, K., T. Schäfer, P. Lindqvist-Reis, M.A. Denecke, M. Plaschke, J. Rothe, J.I. Kim, *Environ. Sci. Technol.*, 36, 5092 (2002).

[13] Matz, W., N. Schell, G. Bernhard, F. Prokert, T. Reich, J. Claußner, W. Oehme, R. Schlenk, S. Dienel, H. Funke, F. Eichhorn, M. Betzl, D. Pröhl, U. Strauch, G. Hüttig, H. Krug, W. Neumann, V. Brendler, P. Reichel, M.A. Denecke, H. Nitsche, *J. Synchrotron Rad.*, 6, 1076 (1999).

[14] McMaster, W.H., N. Kerr Del Grande, J.H. Mallett, J.H. Hubbell, *Compilation of X-ray Cross Sections*, Report UCRL-50174, Section II, Revision I, Lawrence Livermore National Laboratory (1969).

[15] Koningsberger, D.E., R. Prins, "X-ray Absorption: Principles, Applications, Techniques for EXAFS, SEXAFS and XANES", Wiley Interscience, New York (1988).

[16] George, G.N., I.J. Pickering, EXAFSPAK: A Suite of Computer Programs for Analysis of X-ray Absorption Spectra", Stanford Synchrotron Radiation Laboratory, Stanford (1995).

[17] Ressler, T., *J. Physique IV*, 7, 269 (1997).

[18] Newville, M., P. Livins, Y. Yacoby, J.J. Rehr, E.A. Stern, *Phys. Rev. B* 47, 14126 (1993).

[19] Ankudinov, A.L., B. Ravel, J.J. Rehr, S.D. Conradson, *Phys. Rev B* 58, 7565 (1998).

[20] Schwertmann, U., R.M. Cornell, "Iron Oxides in the Laboratory (Preparation and Characterization)", VCH-Verlag, Weinheim (1991).

[21] Natoli, C.R., "EXAFS and Near Edge Structure", 27 in *Chemical Physics*, A. Bianconi, L. Incoccia and S. Stipcich, Springer Verlag, Berlin (1984).

[22] Allen, P.G., J.J. Bucher, D.K. Shuh, N.M. Edelstein, I. Craig, *Inorg. Chem.*, 39(3), 595 (2000). Supporting information.

[23] Altermatt, D., I.D. Brown, *Acta Cryst.*, B41, 240 (1985).

[24] Brown, I.D., D. Altermat, *Acta Cryst.*, B41, 244 (1985).

[25] Dardenne, K., M.A. Denecke, Th. Schäfer, *Advanced Photon Source Activity Report 2002*, ANL-03/21, December 2003.

XPS STUDY OF NEPTUNYL INTERACTION WITH GOETHITE (α-FeOOH), MAGHEMITE (γ-Fe_2O_3) AND HEMATITE (α-Fe_2O_3) IN AQUEOUS MEDIUM

L. Vukcevic[1], Yu.A. Teterin[2], S.N. Kalmykov[3], A.P. Novikov[4], Yu.A. Sapozhnikov[3], A.Yu. Teterin[2], K.I. Maslakov[2], I.O. Utkin[2], K.E. Ivanov[2], A.B. Hasanova[3], N.S. Sherbina[3]

[1]Faculty of Natural Sciences and Mathematics, University of Montenegro
Podgorica, Serbia and Montenegro, vukas@rc.pmf.cg.ac.yu

[2]RRC "Kurchatov Institute", Moscow, Russia, teterin@ignph.kiae.ru

[3]Chemical Department, M.V. Lomonosov MSU, Moscow, Russia, stepan@radio.chem.msu.ru

[4]Vernadsky Institute of Geochemistry and Analytical Chemistry, Russian Academy of Sciences, Moscow, Russia, novikov@geokhi.ru

Abstract

The sorption behaviour of goethite (α-FeOOH) maghemite (γ-Fe_2O_3) and hematite (α-Fe_2O_3) was studied and neptunium physical and chemical states on the surface of these minerals were established. On the basis of the obtained data, elemental and ionic quantitative compositions of the surfaces of the studied minerals and neptunyl NpO_2^+ complexes were determined. Compounds containing Np^{4+} and Np^{6+} did not form. Formation of complexes with the neptunyl $Np^{5+}O_2^+$ group on the surface of α-FeOOH, γ-Fe_2O_3 and α-Fe_2O_3 was observed.

Introduction

Goethite (α-FeOOH) maghemite (γ-Fe_2O_3) and hematite (α-Fe_2O_3) are prevalent natural minerals of high sorption ability to heavy metal ions and radionuclides. The present work studied the sorption mechanisms and $Np(V)O_2^+$ complexes on the surfaces of these minerals by liquid-liquid extraction and X-ray photoelectron spectroscopy (XPS) methods.

Experimental

Goethite (α-FeOOH) maghemite (γ-Fe_2O_3) and hematite (α-Fe_2O_3) were synthesised by the techniques described in [1]. The samples for the XPS study were: Sample I – neptunium on goethite (α-FeOOH + Np), Sample II – neptunium on maghemite (γ-Fe_2O_3 + Np), Sample III – neptunium on hematite (α-Fe_2O_3 + Np). Neptunium chemical states were determined by liquid-liquid extraction. Only Np^{5+} was shown to be present on the samples. XPS spectra of the samples were measured with an electrostatic spectrometer MK II VG Scientific using non-monochromatised $AlK_{\alpha 1,2}$ ($h\nu$ = 1486.6 eV) radiation. The device resolution measured as full width at the half-maximum (FWHM) of the $Au4f_{7/2}$ line on the standard rectangular golden plate was 1.2 eV. The binding energies E_b(eV) were measured relatively to the binding energy of the C 1s electrons from hydrocarbons adsorbed on the sample surface accepted to be equal to 285.0 eV. For the gold standard, the calibration binding energies E_b(C 1s) = 284.7 eV and $E_b(Au4f_{7/2})$ = 83.8 eV were used. The FWHM were measured relative to the width of the C 1s line of hydrocarbons found to be 1.3 eV. The error in determination of electron binding energies and the line widths did not exceed 0.1 eV and that of the relative line intensities was less than 10%. The studied samples were prepared from finely dispersed powders milled on the agate mortar and mounted with adhesive tape on a titanium substrate. For all the samples the quantitative elemental and ionic analysis was done. It was based on the fact that the spectral intensity is proportional to the number of certain atoms in the sample. The following ratio was used: $n_i/n_j = (S_i/S_j)(k_j/k_i)$ where n_i/n_j is the relative concentration of the studied atoms, S_i/S_j is the relative core-shell spectral intensity and k_j/k_i is the relative experimental sensitivity coefficient [2].

Results and discussion

Low binding energy XPS range

The valence bands for the Samples I, II, III are formed mostly from the Fe 3d, 4s, Np 6p, 6d, 7s, 5f and O 2s, 2p electronic shells. The outer valence molecular orbital (OVMO) structure is from the Fe 3d, 4s, Np 6d,7s, 5f and O 2p electrons, while the inner valence molecular orbital (IVMO) structure is from the Fe 3d, 4s, Np 6p and O 2s ones [3]. The OVMO intensity is mostly due to the Fe $3d^5$ electrons from the Fe^{3+} ions (Figure 1). The low intense structure at 12–16 eV can be attributed to the MOs from carbonate CO_3^{2-} and nitrate NO_3^- groups, as well as the C l3s [3]. The Na 2p peak is observed in the spectra from Samples I and III at 31.2 eV. The low binding energy XPS from Samples I, II and III are expected to exhibit the Np 5f peaks at $E_b \approx 2.5$ eV (Table 1). The area under this peak is proportional to the number of the Np 5f electrons weakly participating in the chemical bond and is characteristic of neptunium oxidation states in compounds. Unfortunately, it is very difficult to separate this peak due to the low neptunium concentration in the samples.

Core electron XPS range

The C 1s spectra from the studied samples consist of the basic peak at E_b = 285.0 eV (saturated hydrocarbons) used for calibration and peaks at 287 eV attributed to -CH_2-O- groups and at 289 eV

Figure 1. Low binding energy XPS from $Np^{5+}O_2^+$ + hematite (α-Fe_2O_3) (Sample III)

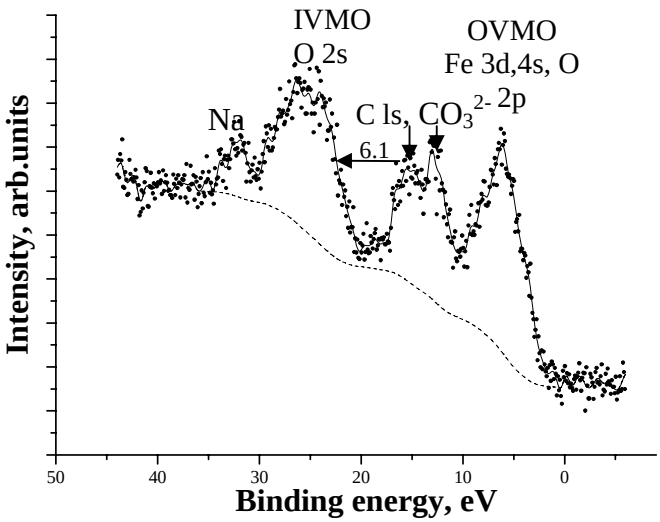

Table 1. Neptunium oxidation states (Np^{n+}) and electron binding energies (E_b, eV) for Samples I, II, III and neptunium compounds

Sample	Np^{n+}	MO	Fe $2p_{3/2,1/2}$ [a)]	Fe 3s	Np $4f_{7/2,5/2}$	O 1s	C 1s
Sample I (α-FeOOH+ Np^{n+})		6.4 17.6 22.4 31.2	711.7 (719.0) 725.3 (734.3)(739.2)	94.1 101.2	403.2 414.9	530.2 531.5 533.4	285.0 286.8 288.8
Sample II (γ-Fe_2O_3 + Np^{n+})	Np^{6+}	7.0 22.7	712.0 (720.0) 725.7 (733.4)(741.3)	94.0 101.5	403.7 415.5	530.7 532.2 533.7	285.0 286.7 288.8
Sample. III (α -Fe_2O_3 + Np^{n+})		6.1 13.1 26.4 31.8	711.9 (719.9) 725.4 (733.4)	93.8 101.3	403.8 415.6	531.0 533.0 534.1	285.0 287.0 289.2
NpO_2	Np^{4+}				402.5 414.3	529.7	284.5
$RbNpO_2(NO_3)_2$ $2H_2O$	Np^{5+}	2.9 (Np 5f) 5.4 27.0			403.6 415.3	531.5 533.5	285.0
Cs_2NpO_2 $(CH_3COO)_3$	Np^{5+}	2.3 (Np 5f) 4.3 27.2			403.0 414.6	531.5	285.0 288.3
$Cs_3NpO_2Cl_4$	Np^{5+}	2.5 (Np 5f) 4.9 26.2			403.4 415.2	531.6	285.0
$Cs_2NpO_2Cl_4$	Np^{6+}	3.3 (Np 5f) 5.3 25.8			404.6 416.4	531.9	285.0
$NaNpO_2$ $(CH_3COO)_3$	Np^{6+}	3.4 (Np 5f) 5.9 24.2 26.0			405.2 417.0	532.0	285.0 288.8

[a)] Satellite binding energies given in parentheses.

attributed to CO_3^{2-} groups (Table 1). The O 1s spectrum (Sample I) consists of a widened peak Γ(O 1s) = 3.2 eV at average E_b = 531 eV, that can be subdivided into the three peaks. The peak at 530.2 eV can be attributed to oxide, the one at 531.5 eV to hydroxyl, and the one at 533.4 eV to water (Table 1). The O 1s spectrum from Sample II also consists of the three peaks (Table 1, Figure 2). The first one is attributed to oxide, the second one to the surface oxygen, and the third one to water. The O 1s spectrum from Sample III differs significantly from that from Samples I and II. It exhibits a weak peak at 531 eV from iron oxide and an intense peak at 533.0 eV attributed to impurities like ClO_4^-, NO_3^-, etc. At 534.1 eV one can see a water-related peak. The Fe 2p spectra are structured and cannot be

Figure 2. XPS from $Np^{5+}O_2^+$ + goethite (α-FeOOH) (Sample I)

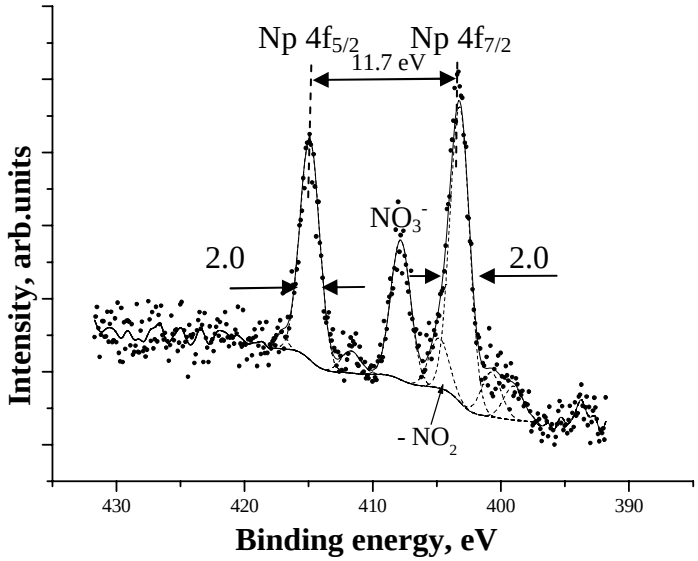

separated correctly into components [4] due the fact that these spectra with high probability manifest the multiplet splitting [5,6]. The Fe $2p_{3/2}$ binding energy (Sample I) E_b = 711.7 eV is some higher than the corresponding value 711.0 eV for α-FeOOH given in [6]. The spin-orbit splitting from this spectra is ΔE_{so} = 13.6 eV is comparable to that ΔE_{so} = 13.2 eV for metallic iron [7]. Typical satellites at about $\Delta E_{sat.}$ = 8 eV (Table 1) on the higher binding energy side from the basic line are observed. Going to the spectra from Samples II and III one can see a certain smearing of satellites for Sample III.

The Np 4f spectra from the studied samples consist of relatively sharp spin-orbit doublets split by ΔE_{so} = 11.7 eV (Figure 2). The binding energies $E_b(Np4f_{7/2})$ of 403.2, 403.7 and 403.8 eV for the studied samples are close to the corresponding values 403.4 and 403.6 eV for $Cs_3NpO_2Cl_4$ and $RbNpO_2(NO_3)_2 2H_2O$ containing Np^{5+} ions (Table I). All the spectra in the Np 4f binding energy range exhibit the N 1s peak.

Quantitative analysis

Since the Fe 2p spectra were structured and complicated, we used the Fe 3s peak for the quantitative analysis in the present work. In this approximation the surfaces (~5 nm) of the studied samples were found to have the following compositions relative to 1 iron atom:

- Sample I: $Fe_{1.00}O^{I}_{1.11}(O)O^{II}_{1.00}(OH^{1-})O^{III}_{0.36}(H_2O)Np_{0.013}(Np^{5+})Na_{0.33}(Na^{+})Cl_{0.14}$ $(Cl^{-})C^{I}_{0.83}(CH_3\text{-})$ $C^{II}_{0.19}(\text{-}CH_2\text{-}O\text{-})C^{III}_{0.12}(CO_3^{2-})$ $N^{I}_{0.03}(\text{-}NO_2)N^{II}_{0.09}(NO_3^{-})K^{I}_{0.06}(K^{+})$

- Sample II: $Fe_{1.00}O^{I}_{1.08}(O)O^{II}_{0.71}(O)O^{III}_{0.20}(H_2O)Np_{0.008}(Np^{5+})C^{I}_{0.66}(CH_3\text{-})C^{II}_{0.09}(\text{-}CH_2\text{-}O\text{-})C^{III}_{0.04}$ (CO_3^{2-}) $N^{I}_{0.06}(NO_3^{-})$

- Sample III: $Fe_{1.00}O^{I}_{1.60}(O)O^{II}_{3.87}(ClO_4^{-})O^{III}_{0.81}(H_2O)Np_{0.02}(Np^{5+})Na_{0.07}(Na^{+})Cl_{0.37}(ClO_4^{-})C^{I}_{3..80}$ $(CH_3\text{-})$ $C^{II}_{0.30}(\text{-}CH_2\text{-}O\text{-})C^{III}_{0.30}(CO_3^{2-})N^{I}_{0.87}(NH_4^{+})N^{II}_{0.16}(\text{-}NO_2)N^{III}_{0.68}(NO_3^{-})$

where $O^{I}(O)$ $O^{II}(OH^{1-})$ $O^{III}(H_2O)$ and $O^{II}_{3.87}(ClO_4^-)$ – oxygens from oxide, hydroxyl, water, and perchlorate group. The observed oxide excess in Samples I, II and III can be partially explained by absorbed oxygen-containing molecules on the surface and relatively high measurement errors. Despite the presence of the impurity groups on the surface, the Np 4f spectra yield a conclusion that neptunium presents only as Np^{5+}. Other neptunium ions like Np^{4+} and Np^{6+} are not present on the surfaces of the studied samples.

Conclusions

For the first time the XPS study of interaction of $Np^{5+}O_2^+$ in aqueous medium with goethite (α-FeOOH) maghemite (γ-Fe_2O_3) and hematite (α-Fe_2O_3) was done. It allowed a quantitative elemental and ionic analysis of the studied samples and determination of neptunium physical and chemical states on the surface.

It was established that as a result of interaction of neptunyl group with goethite, maghemite and hematite in aqueous medium, Np^{4+} and Np^{6+}compounds did not form on the surface, while the new neptunyl $Np^{5+}O_2^+$ compounds formed. These compounds were found to contain oxygens from goethite, maghemite, hematite and water and/or carbonate CO_3^{2-} and nitrate NO_3^- groups in the equatorial planes.

Acknowledgements

The present work was supported by the common program of US DOE and RAS (Project M6RAS0008) administrated via CRDF (grant RC0-20003-SC14), RFBR (grants 02-03-32693, 04-03-32892) and the State Program of the Leading Scientific Schools (grant 1763).

REFERENCES

[1] Chopin, G.R., A.H. Bond, *J. Analyt. Chem.*, 51(12), 1240 (1996) (in Russian).

[2] *Surface Analysis by Auger and X-ray Photoelectron Spectroscopy*, D. Briggs and M.P. Sih, Eds., Moscow, Mir (1987), 598 pages (in Russian).

[3] Teterin, Yu.A., S.G. Gagarin, *Russian Chemical Reviews*, 65(10), 825 (1996).

[4] Scrocco, M., *Phys. Rev. B* 23(9) 4381 (1981).

[5] Teterin, Yu.A., A.Yu. Teterin, *Russian Chemical Reviews* 71(5), 347 (2002).

[6] Nefedov, V.I., "X-ray Photoelectron Spectroscopy of Chemical Compounds", Mosow, Himiya (1984), 256 pages.

[7] Fuggle, J.C., *J. Electron Spectros. Relat. Phenom.*, 21, 275 (1980).

ANNEX

Abstracts*

* The abstracts of the papers unavailable in their entirety at the time of publication have been grouped here.

CO-ORDINATION CHEMISTRY OF TRIVALENT ACTINIDES AND LANTHANIDES FOR THE PURPOSE OF RATIONAL DESIGN OF SEPARATION SYSTEMS

Tsuyoshi Yaita
Department of Materials Science & Synchrotron Radiation Research Center
Japan Atomic Energy Research Institute
Tokai-mura, Naka-gun, Ibaraki 319-1195, Japan
yaita@mummy.tokai.jaeri.go.jp

Abstract

The co-ordination chemistries of trivalent lanthanides [Ln(III)] and actinides [An(III)] give us key information toward design of separation system of these elements. Until now, we have performed investigations of complex structure and electronic structure using X-ray crystallography, neutron scattering, the synchrotron radiation methods of EXAFS/XANES, XES and NEXAFS. The ligands we have studied to date are: 1) mutidentate phosphine oxides and 2) amides as oxygen donor ligands. The oxygen donor ligands do not show any difference between Ln(III) and An(III) of the same size and their complex structures are determined mainly by a relationship between structure of the molecule and the occupancy around the metal ion.

Carbamoyl phosphine oxide (CMPO) is an unsymmetrical structure having two kinds of a donor site, i.e. phosphoryl and carbonyl groups, and its co-ordination structure is quite unique, since there are two types of co-ordination structure, i.e. cis- and trans-structure on the arrangement of P=O and C=O. In contrast, diphosphine oxide (DPDO) is a symmetrical structure due to forming two phosphoryl groups. These two ligands are very interesting in comparison to required space in the primary co-ordination sphere in both solution and solid states.

Amide compounds have been introduced as a separation of actinides on the basis of the concept of green chemistry. However, the amide group is essentially weaker donor than the phosphoryl group and amide type ligands were often insufficient as a separation reagent of trivalent actinides and lanthanides. Then, diglycolamide (DGA) a kind of diamide, recently has developed. The DGA is tridentate ligand, composed of two amides and one ether group as donor part and shows the highest extractability from aqueous nitric acid solution for trivalent lanthanides and actinides of all the extractants. According to the results of relativistic molecular orbital calculation method (DV-DS) the charge distributions of carbonyl and ether oxygens of DGA in Er-DGA complex present -0.34 and -0.22, respectively, and the bond overlap population of the carbonyl and the ether oxygens present 0.66 and 0.40, respectively. Accordingly, the chemical bond of carbonyl oxygen is superior to that of the ether one. Therefore, ether oxygen often shows slightly larger Debye-Waller factor than the carbonyl one. The required space of DGA for co-ordination to the metals is larger than that of bidentate ligands such as malonamide. Counter ion, e.g. nitrate ion, chloride ion, therefore, does not co-ordinate directly to the ions and the DGA forms complex ion. Furthermore, small angle neutron scattering method (SANS) suggests that the DGA molecules aggregate through nitric acid and water bridging. The aggregated DGA behaves as another ligand in the extraction, so that the DGA produces the superior results of trivalent lanthanides and actinides separation. In this presentation, the detailed chemical bond properties on the basis of XES and XAS of O-K edge will be mentioned.

XAFS OF TECHNETIUM COMPLEXES RELEVANT TO TECHNETIUM SPECIATION HANFORD HIGH-LEVEL WASTE TANKS

W.W. Lukens[1], **D.K. Shuh**[1], **N.C. Schroeder**[2], **K.R. Ashley**[3]
[1]Lawrence Berkeley National Laboratory, Berkeley, CA 94720
[2]Los Alamos National Laboratory, Los Alamos, NM 87545
[3]Texas A&M University-Commerce, Commerce, TX 75429

Abstract

Technetium is a long-lived (^{99}Tc: 213 000 year half-life) fission product found in nuclear waste and is one of the important isotopes of environmental concern. The known chemistry of technetium suggests that it should be found as pertechnetate, TcO_4^-, in the extremely basic environment of the nuclear waste tanks at the Hanford site. However, other chemical forms of technetium are present in significant amounts in certain tanks, and these non-pertechnetate species complicate the treatment of the waste. The only spectroscopic characterisation of these non-pertechnetate species is the XANES spectra of actual tank waste reported by Blanchard and co-workers. To better understand the behaviour of technetium under these conditions, we have investigated the reduction of pertechnetate in highly alkaline solution in the presence of compounds found in high-level waste. These results and the XAFS spectra of these species are compared to the chemical behaviour and XANES spectra of the actual non-pertechnetate species.

PHONON DISPERSIONS AND CRYSTAL DYNAMICS IN fcc δ-PLUTONIUM-GALLIUM USING HIGH-RESOLUTION INELASTIC X-RAY SCATTERING [1]

J. Wong
Lawrence Livermore National Laboratory, University of California
P.O. Box 808, Livermore CA, 94551 USA

Abstract

The phonon spectra of plutonium and its alloys have been sought after in the past few decades following the discovery of this actinide element in 1941, but with no success. This was due to a combination of the high neutron absorption cross-section of ^{239}Pu, the common isotope, and non-availability of large single crystals of any Pu-bearing materials. We have recently designed a high-resolution inelastic X-ray scattering experiment using a bright synchrotron X-ray beam at ESRF, Grenoble and mapped the full phonon dispersion curves of an fcc δ-phase polycrystalline Pu-Ga alloy. Several unusual features, including a large elastic anisotropy, a small shear elastic modulus C', a Kohn-like anomaly in the T_1[011] branch, and a pronounced softening of the [111] transverse modes are found. These features can be related to the phase transitions of plutonium and to strong coupling between the lattice structure and the 5*f* valence instabilities. Our results also provide a critical test for theoretical treatments of highly correlated 5*f* electron systems as exemplified by recent dynamical mean field theory (DMFT) calculations for δ-plutonium [2]. Recent work on imaging phonons in Pu-Ga alloys with thermal diffuse scattering [3] will be also be discussed.

This work was performed in collaboration with D. Farber, F. Occelli, D. Clatterbuck, M. Wall and A. Schwartz of LLNL, as well as with Dr. M. Krisch (ESRF) and Prof. T-C. Chiang (UIU), and under the auspices of the US Department of Energy by the University of California, Lawrence Livermore National Laboratory, Contract No. W-7405-Eng-48.

REFERENCES

[1] Wong, *et al*., *Science*, 301, 1078 (2003).

[2] Dai, *et al*., *Science*, 300, 953 (2003).

[3] Wong, *et al*., *Appl. Phys. Lett*., 84, 3747 (2004).

LOCAL STRUCTURE AND VIBRATIONAL PROPERTIES OF α-PU, α-U AND THE α-U CHARGE DENSITY WAVE

E.J. Nelson[1], **P.G. Allen**[2], **K. J.M. Blobaum**[1], **M.A. Wall**[1], **C.H. Booth**[3]
[1]Materials Science and Technology Division, Lawrence Livermore National Laboratory
P.O. Box 808, Livermore, CA 94551
[2]Chemistry and Chemical Engineering Division, Lawrence Livermore National Laboratory
P.O. Box 808, Livermore, CA 94551
[3]Chemical Sciences Division, Lawrence Berkeley National Laboratory
Berkeley, CA 94720

Abstract

The local atomic environment and vibrational properties of atoms in monoclinic pure α-plutonium as well as orthorhombic pure α-uranium and its low-temperature charge-density-wave (CDW) modulation are examined by extended X-ray absorption fine structure spectroscopy (EXAFS). Pu L_{III}-edge and U L_{III}-edge EXAFS data measured at low temperatures verify the crystal structures of α-U and α-Pu samples previously determined by X-ray diffraction and neutron scattering. Debye-Waller factors from temperature-dependent EXAFS measurements are fit with a correlated Debye model. The observed Pu-Pu bond Debye temperature of θ_{cD}(α-Pu) = 162 ± 5 K for the pure α-Pu phase agrees with our previous measurement of the Debye temperature of the gallium-containing α′-Pu phase in a mixed phase 1.9 at.% Ga-doped α′-Pu/δ-Pu alloy. The temperature dependence of the U-U nearest neighbour and second nearest neighbour Debye-Waller factors exhibits a sharp discontinuity in slope near T_{CDW} = 43 K, the transition temperature at which the charge-density wave (CDW) in α-U condenses from a soft phonon mode along the (100) direction. Our measurement of the CDW using EXAFS is the first observation of the structure of the CDW in polycrystalline α-U. The different temperature dependence of the Debye-Waller factor for $T < T_{CDW}$ can be modelled by the change in bond length distributions resulting from condensation of the CDW. For $T > T_{CDW}$, the observed Debye temperature of θ_D(α-U) = 199 ± 3 K is in good agreement with other measurements of the Debye temperature for polycrystalline α-U. CDW structural models fit to the α-U EXAFS data support a squared CDW at the lowest temperatures, with a displacement amplitude of ε = 0.05 ± 0.02 Å.

This work was performed under the auspices of the US Department of Energy by the University of California, Lawrence Livermore National Laboratory under Contract W-7405-Eng-48. UCRL-ABS-206132.

ACTINIDE SOLUTION SPECIATION USING HIGH-ENERGY X-RAY SCATTERING

L. Soderholm, S. Skanthakumar, J. Neuefeind
Chemistry Division
Argonne National Laboratory
Argonne, IL 60439

Abstract

High-energy (> 80 keV) X-ray scattering (HES) is proving to be an important tool for probing metal-ion speciation in solution. Historically dissolved metal ions in aqueous solutions have been thought of as homogeneous, amorphous systems with no significant correlations outside of the metal-ion first co-ordination sphere. This description is the fundamental concept used in a variety of theories and calculations designed to quantify the energetic of dissolved ions in solution. Recent high-energy X-ray scattering experiments are providing a new picture of the metal-ion environment, which includes metal-metal and metal-solvent correlations out to distances of 6 Å and longer. The scattering data can be analysed to provide metal-solvent correlation distances. In addition, electron densities about scattering ions determined from the spectra can be used to glean information about the number of co-ordinating ions. Several examples of heavy-metal (actinide) ions in aqueous solution are presented and compared with EXAFS data in order to demonstrate the complementarities of these techniques. Efforts are made to highlight the new information available from HES and its implication for computational studies.

This work has taken advantage of the Actinide Facility and the Advanced Photon Source, both of which are funded by the US DOE – OBES, under contract W-38-109-ENG-38.

ACTINIDE SPECIATION BASED ON EXAFS SPECTROSCOPY: FROM SHELL FITTING TO MCTFA

A. Rossberg[1] **and A. Scheinost**[2]
[1]The Rossendorf Beamline at ESRF, Grenoble, France
[2]Institute of Radiochemistry, Forschungszentrum Rossendorf, Dresden, Germany

Abstract

The speciation of actinides in the geosphere is one of the most crucial tasks for reliable risk assessments. Using EXAFS spectroscopy, structural parameters of actinide species, such as interatomic distances, structural and thermal disorder, and co-ordination numbers, can be determined by shell fitting. While this approach has proven very useful for deciphering the molecular structure of isolated actinide species, it fails if more than one species is present at the same time. Unfortunately, the coexistence of several metal species is a common case in environmental samples due to the presence of aqueous, sorbed, organic and mineral phases [1]. For actinides, species variability is even higher, since they form complexes with a wide range of inorganic and organic ligands ubiquitous in natural environments, and since several oxidations states may coexist. Hence, the measured EXAFS spectra are a superposition of the EXAFS contributions of each single species, weighted according to their relative concentrations. To derive the spectral contribution of each species from such mixtures three statistical approaches may be used, depending on the degree of information available. In any case, a set of EXAFS spectra ($N_{spectra} > N_{species}$) with some variation in speciation is a prerequisite.

1) A comprehensive spectral database of known species is available, which contains all species present in the set of samples. In this case, principal component analysis is used to derive an approximate number of species present in the mixtures, target transformation factor analysis [2] is used to find the matching species in the database, and linear combination fit is used to quantify their relative spectral contribution, i.e. their relative concentration.

2) The concentrations of some of the species in the mixtures are known, e.g. derived from thermodynamic equilibrium calculations. In this case, one can use incomplete concentration profiles as test vectors for iterative target transformation factor analysis (ITFA) [3] to derive the relative concentrations and the spectral patterns of the species. Then, the molecular structure of the species is derived by standard shell fitting.

3) Neither the species spectra nor their concentrations are known. For this case, we are presently developing a new method by combining target transformation factor analysis with Monte Carlo simulation (MCTFA). This method requires a first approximated structure of the ligand, which presumably interacts with the metal ion to form the species. This could be the structure of a mineral to represent the sorbing surface, or the structure of a small organic ligand to represent either a dissolved organic species or the functional group of natural organic substance. Such approximate structures are often available from XRD structural databases and increasingly

from quantum chemical calculations. The MCTFA method yields the spectra, the relative concentration distribution, the refined three-dimensional structure of the pure complexes and the statistically determined radial absorber/scatterer pair distribution functions for the single scattering and the possibly multiple scattering paths.

Using test mixtures of uranyl phosphate, uranyl oxalate and uranyl acetate, we will demonstrate the use and limitations of all three statistical methods.

REFERENCES

[1] Scheinost, A.C., R. Kretzschmar, S. Pfister and D.R. Roberts, *Environ. Sci. Technol.*, 36, 5021 (2002).

[2] Wasserman, S.R. *Journal de Physique IV*, 7, 203 (1997).

[3] Rossberg, A., T. Reich and G. Bernhard, *Analytical and Bioanalytical Chemistry*, 376, 631 (2003).

SURFACE DIFFRACTION COMBINED WITH GRAZING-INCIDENCE X-RAY SPECTROSCOPY: A NEW LEVEL OF DETAIL FOR SURFACE COMPLEXATION CHARACTERISATION

G.A. Waychunas
Earth Sciences Division, Lawrence Berkeley National Laboratory
MS70R0108B, One Cyclotron Road, Berkeley, CA 94720 USA

Abstract

Surface complexation studies utilising grazing-incidence EXAFS and XANES (GIXAS) can reveal crucial details of specific surface chemistry, and can be applied to extremely low surface coverages. However surface diffraction, and specifically Crystal Truncation Rod (CTR) analysis, can enhance the utility of GIXAS by revealing the precise nature of the mineral surface in equilibrium with reactive solutions. This information permits a complete picture of the interface to be determined, and reveals complexities not seen well with GIXAS alone, and completely undetectable with powder XAS.

In this talk the methods and physics of both GIXAS and CTR diffraction experiments will be described, and a detailed example using hematite (0001) and $(1\bar{1}02)$ surfaces and arsenate sorption will be discussed. Limitations in using the combined methods for actinides will be considered. [Jeff Catalano from Stanford University will describe an example of uranyl GIXAS/CTR analysis later in this programme.]

THE COVALENT BOND IN THE URANYL ION

R.G. Denning
Department of Chemistry, Inorganic Chemistry Laboratory
South Parks Road, Oxford, OX1 3QR, UK

Abstract

Recently polarised oxygen-K_α X-ray absorption and emission spectroscopic data have been obtained on a single crystal of $Cs_2UO_2Cl_4$. These will be discussed. They give a direct measure of oxygen 2p covalent interactions as manifest in the vacant metal-centred (5f and 6d) molecular orbitals of the uranyl ion. With the aid of earlier polarised XAS data at the L_1 and L_3 edges (from Zachariasen, and also from Denecke) it is now possible to arrive at a complete experimental order for all of the important metal-centred valence orbitals.

THE STRUCTURE OF X-RAY $O_{4,5}$(U) – EMISSION AND ABSORPTION NEAR $O_{4,5}$(U) EDGE SPECTRA OF UO_3

K.E. Ivanov[1], D.K. Shuh[2], Yu.A. Teterin[1], A.Yu. Teterin[1], S.M. Butorin[3], J-H. Guo[3], M. Magnuson[3], J. Nordgren[3]
[1]Russian Research Center "Kurchatov Institute", Kurchatov 1, sq., Moscow 123182 Russia
[2]Lawrence Berkeley National Laboratory, Berkeley, CA 94720, USA
[3]Physical Department of the Uppsala University, C-751 21, PB 530, Uppsala, Sweden

Abstract

Resonant X-ray emission spectra (RXES) and X-ray near $O_{4,5}$(U) edge absorption spectra (NEXAFS) of UO_3 were measured at the Advanced Light Source of the Lawrence Berkeley National Laboratory in order to study the density of the occupied and vacant U 5*f* (np) states. Earlier, the direct participation of the U 5*f*,6p electrons in the chemical bond was shown on the basis of the X-ray photoelectron [1] and non-resonant X-ray $O_{4,5}$(U) emission [2] spectral data for uranium oxides. The present work examines the structure of the resonant $O_{4,5}$(U) emission spectra measured using $O_{4,5}$(U) NEXAFS data and compares it to the non-resonant spectra for the filled U 5*f*,6p states. The $O_{4,5}$(U) NEXAFS spectra were also interpreted. Taking into account the non-relativistic and relativistic theoretical calculations results of the ground state for the clusters reflecting the close environment of uranium ion in oxides, the U 5*f* electrons were suggested to be able to participate directly in the chemical bond. The fine RXES structure from UO_3 was explained by the presence of the filled U 6p beside the U 5*f* states in the outer valence band. Resonant soft X-ray emission and X-ray absorption spectroscopies have proven to be an efficient tool in study of the electronic structure of uranium compounds. It provides high resolution reliable spectral data with relatively small amount of uranium samples.

This work was supported by the RFBR (Grant N 04-03-32892) and Office of Energy Research, Office of Basic Energy Science, Material Science Division of the US Department of Energy, under Contract No. DE-AC03-76SF00098.

REFERENCES

[1] Teterin, Yu.A. and S.G. Gagarin, *Russian Chemical Reviews*, 65 (10), 825 (1996).

[2] Teterin, Yu.A., V.A. Terekhov and K.E. Ivanov, *Doklady Rossiiskoi Akademii Nauk*, 345 (3) 356 (1995).

ADSORPTION AND CO-PRECIPITATION OF U(VI) WITH CALCITE: SPECTROSCOPIC OBSERVATIONS

R.J. Reeder[1], **E.J. Elzinga**[1], **C.D. Tait**[2], **D.E. Morris**[2]
[1]Department of Geosciences and Center for Environmental Molecular Science
SUNY-Stony Brook, NY 11794-2100
[2]Chemistry Division, Los Alamos National Laboratory
Los Alamos, NM 87545

Abstract

The adsorption and co-precipitation of U(VI) species at the calcite surface were investigated in separate experiments over the pH range 7.4-8.3 using EXAFS and luminescence spectroscopies. Results from adsorption experiments in pre-equilibrated calcite suspensions indicate that uranyl triscarbonate-like adsorption complexes dominate at U(VI) solution concentrations < 500 μM, whereas the formation of U(VI) hydroxide and carbonato precipitates is observed at higher concentrations, consistent with isotherm data and aqueous speciation calculations. The EXAFS data indicate weak splitting in the equatorial O shell of the U(VI) adsorption complexes, which could indicate that adsorption complexes are bound in an inner-sphere fashion at the calcite surface, or alternatively that multiple U(VI) species exist. The luminescence data indicate the presence of at least two adsorption complexes that change proportion with U(VI) loading. One species, dominating at low surface coverage, is the uranyl triscarbonate complex. A second species is observed at higher surface loadings with a luminescence spectrum that is intermediate between the triscarbonate species found at the lowest loadings and uranyl co-precipitated into bulk polycrystalline calcite. Consequently, multiple uranyl species are likely to exist at the calcite surface during interaction of U(VI)-containing waters in the near-surface environment.

Co-precipitation experiments with calcite single crystals reveal site-selective incorporation of U(VI) with bulk EXAFS revealing a co-ordination that differs from that in the aqueous solution. Luminescence spectra reveal the presence of multiple U(VI) species, associated with incorporation at distinct surface sites. The formation of uranyl triscarbonate-like surface complexes indicated by the adsorption results allows formulation of a model that explains the site selective incorporation of U(VI) at the calcite $(10\bar{1}4)$ growth surface of single crystals. We can additionally conclude that preferential incorporation at "–" sites relative to "+" sites reflects steric hindrance for binding of the triscarbonate complex at the latter.

SYNCHROTRON-BASED STUDIES OF URANIUM SPECIATION IN CONTAMINATED SEDIMENTS AND RELATED MODEL SYSTEM

J.G. Catalano[1,2], S.M. Heald[3], J.M. Zachara[4], G.E. Brown, Jr.[1,5]
[1]Surface and Aqueous Geochemistry Group, Department of Geological and Environmental Sciences
Stanford University, Stanford, CA 94305-2115
[2]Environmental Research Division, Argonne National Laboratory, Argonne, IL 60439
[3]PNC-CAT, Advanced Photon Source, Argonne National Laboratory, Argonne, IL 60439
[4]Pacific Northwest National Laboratory, Environmental Dynamics & Simulation
PO Box 999, MS K8-96, Richland, WA 99352
[5]Stanford Synchrotron Radiation Laboratory, SLAC
MS 69, 2575 Sand Hill Road, Menlo Park, CA 94025

Abstract

Evaluation of the human health risks of widespread uranium contamination of soils, sediments and groundwater requires an understanding of the geochemical processes that control the fate and transport of uranium in such systems. Determining the speciation of uranium at the source of contamination, as well as the processes affecting transport, especially adsorption to mineral surfaces, is essential in order to develop appropriate predictive transport models. We employed synchrotron-based X-ray spectroscopic and diffraction methods to study uranium speciation in contaminated vadose zone sediments from the Hanford Site in Washington, and also applied these methods to study uranyl adsorption onto mineral surfaces in model systems. In the study of contaminated sediments from the Hanford Site, U L_{III}-EXAFS spectroscopy revealed that uranium occurred primarily as a member of the uranophane group of minerals. As the local atomic environment of uranium is similar in all members of this mineral group, EXAFS could not identify the specific phase present. Complementary μXRD measurements identified only sodium-boltwoodite $Na(UO_2)(SiO_3OH)\cdot 1.5\ H_2O$, which has effectively sequestered uranium in these sediments under the current geochemical and hydrologic conditions.

Two studies were conducted to evaluate how adsorption processes influence uranium partitioning to solids from contaminated waters. In the first study, U(VI) adsorption onto montmorillonite as a function of pH, ionic strength, and CO_2 content was examined using EXAFS spectroscopy. At low ionic strength, outer-sphere adsorption of U(VI) via cation exchange was found to be more important than predicted by previous surface complexation models. U(VI) adsorbs to edge sites as inner-sphere uranyl-carbonato ternary complexes in the presence of atmospheric CO_2 concentrations. U(VI) binds preferentially to $[Fe(O,OH)_6]$ edge sites over $[Al(O,OH)_6]$ sites in both the presence and absence of CO_2. Past surface complexation models should be modified to account for these findings, and future studies of U(VI) transport in the environment should consider how uranium retardation will be affected by changes in pH and ionic strength. In the second study, CTR diffraction and GI-EXAFS spectroscopy were used to investigate U(VI) adsorption onto α-Al_2O_3 and α-Fe_2O_3 $(1\bar{1}02)$ surfaces at pH 5-7 (I = 0.1 M). U(VI) in the form of uranyl-carbonato ternary complexes, adsorbed in a monodentate fashion on α-Al_2O_3 $(1\bar{1}02)$ and in a bidentate fashion on α-Fe_2O_3 $(1\bar{1}02)$. The α-Fe_2O_3 $(1\bar{1}02)$ surface was found to have a higher affinity for U(VI) adsorption under these solution conditions. The adsorption geometries observed in this study differed from those typically found on powdered substrates using EXAFS spectroscopy under the same conditions.

URANIUM IN CALCIUM CARBONATE SYSTEMS

S.D. Kelly[1], J.F. Banfield[2], S.C. Brooks[3], J.K. Fredrickson[4], E.T. Rasbury[5], C. Spötl[6], N.C. Sturchio[7], Y. Suzuki[8], K.M. Kemner[1]

[1]Environmental Research Division, Argonne National Laboratory, Argonne, IL 60439
[2]Department of Earth and Planetary Sciences, University of California, Berkeley, CA 94720
[3]Environmental Sciences Division, Oak Ridge National Laboratory, Oak Ridge, TN 37831
[4]Pacific Northwest National Laboratory, Richland, WA, 99338
[5]Department of Geosciences, SUNY at Stony Brook, Stony Brook, NY, 11794
[6]Institut für Geologie und Paläontologie, Universität Innsbruck, 6020, Innsbruck, Austria
[7]Department of Earth and Environmental Sciences, University of Illinois, Chicago, IL 60607
[8]Frontier Research System for Extremophiles, Japan Marine Science & Technology Center, 2-15, Natushima-cho, Yokosuka 237-0061, Japan

Abstract

The interaction of U-carbonato complexes with calcium in both aqueous and solid phases has implications for fate and transport of U in the subsurface. Dating of natural calcite deposits based on U-Pb and U series techniques is based on the assumption that the U within these samples originate with the time of formation and has not been altered by diagenesis. However, the mobility of U in natural calcite deposits is unknown, leaving the interpretation of U-based dating techniques open to criticism. In contrast to the physical dimensions of Ca^{2+}, hexavalent U is often in the form of a uranyl with two tightly bound oxygen atoms. This size difference between the uranyl and Ca^{2+} cations has led some investigators to the conclusion that the uranyl cation cannot be accommodated in the calcite structure. The dilute concentrations of U in natural materials have precluded direct determination of uranyl's local environment until recently. Hence, debate over the accuracy of U-based dating techniques has continued.

Current remediation efforts for U-contaminated subsurface environments focus on altering the redox chemistry of U. Hexavalent U, U(VI) is relatively mobile in oxidising subsurface environments and forms carbonate complexes in carbonate-rich environments. In contrast, compounds containing tetravalent U, U(IV) such as uraninite (UO_2) are much less soluble and therefore U(IV) is considered to be relatively immobile. The change in mobility of U on the basis of redox chemistry can be exploited to sequester U in the subsurface and limit contaminant migration. Potential reduction mechanisms being explored include the use of indigenous microorganisms and Fe(II) from Fe-oxyhydroxides. The rich geochemistry at U-contaminated sites is being explored for their potential impacts on different remediation strategies. Recently, environmentally relevant concentrations of Ca^{2+} in calcareous groundwater, like those found at DOE sites including Oak Ridge and Hanford, have been shown to have a negative effect on bioreduction of U(VI). Furthermore, the by-products of bioreduction of U(VI) can form UO_2 nanoparticles that can be transported as colloids. Therefore, direct measurement of the U valence state and chemical species in soils is fundamental to understanding the fate and transport of U in contaminated subsurface environments.

X-ray absorption fine structure (XAFS) measurements are ideally suited for investigating incorporation of dilute concentrations of U in calcium carbonate aqueous solutions and solid phases and in by-products of microbial reduction. We have used the MRCAT insertion device beamline at the Advanced Photon Source to make U L_{III} edge XAFS, micro-X-ray fluorescence, and micro-XAFS measurements on a number of natural and synthetic samples. These studies have investigated the local chemical environment of U in natural calcites and carbonate- and calcium-rich solutions. We have determined the local chemical environment of U in these samples and have observed the incorporation of uranium in natural calcite and the presence of Ca^{2+} counterions associated with uranyl-triscarbonato moieties in solution. These results directly address questions related to the geological dating of calcite deposits and the feasibility of bioremediation of U in calcium- and carbonate-rich environments. A more detailed discussion of these results will be presented.

Acknowledgements

The submitted manuscript has been created by the University of Chicago as operator of Argonne National Laboratory under Contract No. W-31-109-ENG-38 with the US Department of Energy. The US government retains for itself, and others acting on its behalf, a paid-up, nonexclusive, irrevocable worldwide license in said article to reproduce, prepare derivative works, distribute copies to the public, and perform publicly and display publicly, by or on behalf of the government.

IMMOBILISATION OF Ni AND Co IN CEMENT-STABILISED WASTE FORMS: A MICRO-SPECTROSCOPIC STUDY

M. Vespa, E. Wieland, R. Dähn, D. Grolimund, A.M. Scheidegger
Paul Scherrer Institut, Laboratory for Waste Management, 5232 Villigen PSI, Switzerland
M. Vespa, marika.vespa@psi.ch, Tel.: +41 56 310 2966, Fax: +41 56 310 4595

Abstract

Cement-based materials play an important role in multi-barrier concepts developed worldwide for the safe disposal of industrial and radioactive wastes in underground repositories. Cement is used to condition the waste materials and to construct the engineered barrier systems (container, backfill and linear materials). Therefore, a mechanistic understanding of the processes governing the binding of heavy metals in cement systems is essential for long-term predictions of the environmental impact of cement-stabilised waste forms. Co and Ni isotopes are among important contaminants in waste materials resulting from a variety of electricity production in nuclear power plants.

In this study, Co and Ni uptake by hardened cement paste (HCP) has been investigated with the aim of improving our understanding of the immobilisation process of heavy metals in cement at the molecular level. From a chemical standpoint, HCP is a very heterogeneous material, composed mainly of calcium silicate hydrates, calcium hydroxide, calcium aluminates and highly reactive minor phases such as Fe and Mn oxides. Furthermore, the material is highly heterogeneous with particle sizes ranging from a few to a few hundred micrometers. To address the influence of the inherent heterogeneity of HCP on the uptake processes of heavy metals, micro X-ray fluorescence (XRF) and micro X-ray absorption spectroscopic (XAS) experiments were conducted at the micro-focusing ALS beamline 10.3.2 on Ni(II) and Co(II) doped HCP. Although both Ni and Co are divalent metal ions, their behaviour in cementitious systems appears to be different. For example, the micro-spectroscopic study showed that Ni(II) forms layered double hydroxide (LDH) phases. In addition, other newly formed phases such as $Ni(OH)_2$ or Ni phyllosilicates, may also be present. For Co(II) the micro-spectroscopic investigations reveal a highly heterogeneous Co distribution with respect to concentration as well as Co speciation. At some Co-rich spots, Co(II) was found to be oxidised to Co(III) during the hydration period of HCP. The micro-XAS data suggest that Co(III) tends to be incorporated into a Co(III)O(OH)-like phase. At other spots of interest, Co(II) was not oxidised. XAS data analysis suggests that Co(II) is predominately incorporated into newly formed Co(II) hydroxide-like phases ($Co(OH)_2$), Co phyllosilicates or Co LDH. The findings from the micro-spectroscopic study indicate that Co(II) and Ni(II) react differently during the hydration of cement and that both became immobilised in specific cement minerals. These immobilisation processes are expected to reduce the mobility of Co(II) and Ni(II) in the cement matrix. Furthermore, it proves that the immobilisation potential of cement on a micro-scale is element-specific. It is, therefore, important, within a performance assessment programme, to extend our knowledge of immobilisation processes of cement by investigating other radionuclides, including also the actinides. The new micro-XAS beamline at the Swiss Light Source (SLS) will allow micro-XRF, micro-XAS and micro-XRD measurements on sealed radioactive samples.

LOCAL STRUCTURE AND SPECIATION IN THE OXY-HYDROXIDES OF THE MIDDLE ACTINIDES

S.D. Conradson
MST-8 MS G755, Los Alamos National Laboratory, Los Alamos, NM 87545 USA
conradson@lanl.gov

Abstract

XAFS measurements on U, Np and Pu oxy-hydroxide solutions and solids in the IV, VI and VII valences show a number of unusual features relative to complexes under acidic and near neutral conditions. Expanded An-oxo and contracted An-OH equatorial bond lengths are observed in solution that carry over into solids. At the extreme, these changes in bonding induce unusual oxo configurations, such as the tetra-oxo. These are, however, not especially stable and represent minima on a dynamic energy landscape that is easily modified by changing the conditions. These characteristics of the solutions extend to the solids. Consistent with the solution behaviour, oxo groups appear to be a common feature of both U and $PuO_{(2+x)}$. Insofar as the distorted geometries associated with oxo complexes do not easily fit into the fluorite type lattice, collective behaviour among these sites must produce clustering and nanoscale heterogeneity. These in turn give unusual structural and chemical properties to the resulting solids.

RECENT ADVANCES IN RESONANT MAGNETIC SOFT X-RAY SCATTERING FROM LANTHANIDES: QUANTITATIVE ANALYSIS AND APPLICATIONS

E. Weschke[1]*, H. Ott[1], E. Schierle[1], C. Schüßler-Langeheine[2], G. Kaindl[1]
[1]Institut für Experimentalphysik, Freie Universität Berlin,
Arnimallee 14, D-14195 Berlin, Germany
*eugen.weschke@physik.fu-berlin.de
[2]II. Physikalisches Institut, Universität zu Köln,
Zülpicher Str. 77, D-50937 Köln, Germany

Abstract

X-ray scattering in the soft X-ray region is emerging as an important tool for magnetic studies, exploiting the large enhancement of magnetic scattering at resonant core-electron excitations. For the $M_{4,5}$ resonances of the lanthanides, magnetic scattering lengths as large as $100r_o$ have been theoretically predicted by Hannon, *et al*. [1]. This agrees qualitatively with the observed enhancement of the magnetic scattering intensity by a factor of $\approx 10^7$ at the M_4 resonance of uranium [2]. A quantitative characterisation of magnetic X-ray scattering at these resonances, however, has been impeded by the strong photon absorption.

We report on resonant magnetic soft X-ray scattering experiments on thin lanthanide films, which where carried out using a newly developed, fully UHV-compatible diffractometer that allows thin-film preparation *in situ* and scattering experiments at low temperatures. With thin Ho metal films of ≈15 atomic layers, absorption effects are substantially reduced and a quantitative characterisation of the resonant scattering process at the M_5 edge becomes feasible. Separating linear and circular dichroic terms in the scattering amplitude, we find magnetic scattering lengths of the order of $200r_o$ at resonance, while the effective X-ray penetration depth can be tuned down to ≈20 Å [3]. This opens interesting opportunities for the study of thin films and dilute systems; the huge enhancement allows the study of anti-ferromagnetic structures [4], finite-size effects [5] and even critical scattering in ultra-thin films. The tunable photon absorption across the resonance can be used for magnetic depth profiling, which was exploited to characterise the depth-dependent growth of anti-ferromagnetic domains across the ferromagnetic/anti-ferromagnetic phase transition in Dy metal films. Similar applications are expected in the case of actinide systems.

Acknowledgements

The work was supported by the BMBF, project 05KS1KEE/8, and the DFG, Sfb-290, TPA06.

REFERENCES

[1] Hannon, J.P., *et al*., *Phys. Rev. Lett.*, 61, 1245 (1988).
[2] Isaacs, E.D., *et al*., *Phys. Rev. Lett.*, 62, 1671 (1989).
[3] Ott, H., *et al*., *Phys. Rev. Lett.*, submitted (2004).
[4] Schüßler-Langeheine, C., *et al*., *J. Electr. Spectroscop. Relat. Phenom*., 114-116, 953 (2001).
[5] Weschke, E., *et al*., *Phys. Rev. Lett.*, submitted (2004).

LOCAL STRUCTURE STUDIES OF ^{115}Ce COMPOUNDS

M. Daniel[1,2], S-W. Han[1], C.H. Booth[1], A.L. Cornelius[2], E.D. Bauer[3], P.G. Pagliuso[3], J.L. Sarrao[3], J.D. Thompson[3], L. Morales[3], R.S. Kumar[2]
[1]Lawrence Berkeley National Laboratory, Berkeley, California 74720
[2]University of Nevada Las Vegas, Las Vegas, Nevada 89154
[3]Los Alamos National Laboratory, Los Alamos, New Mexico 87501

Abstract

Extended X-ray absorption fine structure (EXAFS) has been used to probe the local structure of various Ce-based heavy fermion compounds. In the Ce(Ir,Rh)In_5 compounds, our EXAFS measurements as a function of temperature from all edges indicate the local structure of all the samples under investigation is well ordered with no gross phase separation. The results of our investigation suggest that the anomalous specific heat behaviour observed in the low Rh doping range has some other explanation and some possibilities are discussed. In the $CeCoIn_{5-x}Sn_x$ series, our EXAFS fit results indicate that the dopant Sn atoms predominantly occupying the planar In(1) sites. These results are consistent with the quasi-two-dimensional electronic properties of $CeCoIn_5$ and will be discussed in relation to the observed bulk properties. Preliminary results on ^{115}Pu and ^{115}U compounds will also be presented.

NEPTUNIUM(V) AND PLUTONIUM(VI) INTERACTIONS WITH GOETHITE, HAUSMANNITE AND MANGANITE: A LOW-TEMPERATURE EXAFS STUDY

R.E. Wilson[1], D.A. Shaughnessy[3], P.A. Wilk[3], C.H. Booth[1], H. Nitsche[2]
[1]Department of Chemistry, University of California, Berkeley, CA
[2]Nuclear Sciences Division, Lawrence Berkeley National Laboratory, Berkeley, CA
[3]Lawrence Livermore National Laboratory, Chemical Biology and Nuclear Science Division

Abstract

The use of intense X-ray beams to study the surface complexes of actinides and metal oxide surfaces requires some caution with respect to beam promoted oxidation-reduction reactions. These reactions require consideration when dealing with the more redox-sensitive actinides, plutonium and neptunium. EXAFS experiments with TiO_2, goethite and Pu(VI) as well as with Np(V) aqueous solutions and Np(V)-manganese oxide sorption samples indicated that a beam-mediated or induced-redox transformation was occurring in these systems during data collection at room temperature.

In order to stop all redox reactions from occurring in the samples and to improve data quality, we developed a method for the freezing of wet transuranic samples at liquid helium temperatures. Using this method we have observed a plutonyl-goethite surface complex that is, during exposure to the beam, stable. Initial fits to the EXAFS spectra indicate a mixed Pu(V/VI) surface complex on the surface of goethite. Experiments with Np(V) on goethite show little or no reduction of the Np(V) on the surface of goethite during the course of the experiments at both 20 K and 300 K, in contrast to those experiments with Np(V) and Pu(VI) on manganese(II,III) containing minerals at room temperature that showed reduced Np(IV) and Pu(IV) species.

XAFS MEASUREMENT OF LANTHANIDES AND ACTINIDES ON BL11XU AT SPRING-8

H. Shiwaku[1], T. Yaita[2], Y. Okamoto[2], S. Suzuki[2], T. Harami[1], S. Inoue[3], T. Kudo[3], T. Tanida[3]
[1]Synchrotron Radiation Research Center, Japan Atomic Energy Research Institute
Mikazuki-cho, Sayo-gun, Hyogo 679-5148 Japan
[2]Department of Materials Science, Japan Atomic Energy Research Institute
Tokai-mura, Naka-gun, Ibaraki 319-1195, Japan
[3]Japan Synchrotron Radiation Research Institute
Mikazuki-cho, Sayo-gun, Hyogo 679-5198 Japan

Abstract

XAFS (X-ray absorption fine structure) measurement is widely used for structural analysis, since the measurement procedure is simple independent of materials (solid, liquid or gas). By using the high flux X-rays of a wide energy range generated from the synchrotron radiation (SR) the accuracy of structural analysis was improved. Also in structural analysis of lanthanides and/or actinides materials, XAFS is being accepted as one of the very effective methods.

Japan Atomic Energy Research Institute (JAERI) built an undulator beamline BL11XU at the third-generation SR facility SPring-8, and are performing improvement and advancements of the beamline for high-energy XAFS measurement. Then, since the high-energy XAFS measuring system using the undulator light source was established, we will report this system in this presentation.

The insertion device is an in-vacuum-type linear undulator with source characteristics of cycle length λu = 32 mm, periodicity N = 140 periods, tunable energy range about 6 ~ 70 keV using first, third and fifth harmonics X-ray, and linear polarisation. The flux of X-ray amounts to 1×10^{15} (photons/sec in 0.1% B.W.). The beamline was developed in order to perform high-energy and high-flux X-ray measurements. A double-crystal monochromator was improved from the water-cooled type diamond crystals to the liquid nitrogen circulation cooling type silicone crystals. Near liquid nitrogen temperature (63 K ~ 78 K) thermal linear expansion of silicon becomes small, and thermal conductivity is improved. Then heat load by irradiation of SR can be removed efficiently. As compared with before, the cryogenically-cooled monochromator provides 7.4 times higher flux intensity at 14.4 keV. In order to take out X-rays from low energy to high energy, a multi-crystal switching system was developed. Two sets of Si(111) crystals and Si(311) crystals were put in parallel. Only by translating one axis, crystals are exchangeable. It takes only five minutes to exchange and adjust the crystals under the condition of liquid nitrogen temperature and vacuum status. Using the cryogenically-cooled monochromator will vibrate the location of X-rays by shaking the liquid nitrogen, which flows through piping. Then, we used MOSTAB technique for stabilising the location of the incident X-ray.

Since BL11XU is the undulator beamline, a gap of the undulator is adjusted to obtain the strongest X-ray intensity for each energy step. It is combined with the angle of the monochromator in XAFS measurement. As an example of measurement, K absorption edge measurement of La dilute solution (La^{3+} in aqueous perchloric-acid solution) and uranium mineral samples were measured in transmission mode. Consequently, 0.1 mM solution and high-energy XAFS of U-K edge could be measured. The possibilities of the structural analysis of the lanthanides and actinides materials using the undulator SR beamline were proved.

WAVELET ANALYSIS OF EXTENDED X-RAY ABSORPTION FINE STRUCTURE SPECTRA

H. Funke[1], C. Hennig[1], A. Rossberg[1], A.C. Scheinost[1], M. Chukalina[2]
[1]Forschungszentrum Rossendorf, Institute of Radiochemistry
P.O. Box 510119, D-01314 Dresden, Germany
[1]The Rossendorf Beamline at ESRF
BM20, POB 220, F-38043 Grenoble Cedex, France
[2]Institute of Microelectronics Technology RAS
142432 Chernogolovka, Moscow District, Russia

Abstract

Wavelet transformation (WT) of EXAFS spectra provides radial distance resolution like the conventional Fourier transformation, but provides in addition resolution in k space. This information eases the discrimination of atoms by their elemental nature, especially if these atoms are at the same distance. The aim of this presentation is to investigate the use, the advantages and limitations of WT for EXAFS analysis in general and to apply this approach to solve short-range structures relevant for actinide environmental chemistry. We will briefly discuss the Morlet wavelet, which has specific advantages for EXAFS analysis, including the possibility to estimate parameter values optimised either for elemental (k-space) or for spatial (r-space) resolution.

The advantage of the method is demonstrated by three examples, where light and heavy backscatterers either are located at similar distances from the absorber atoms, or have similar path lengths due to multiple scattering phenomena.

In the first example, we show a series of U(VI)-carboxylate complexes. The Fourier transforms of uranyl acetate, formiate and glycolate all reveal a backscattering shell at ~3.75 Å. A subsequent wavelet analysis clearly distinguishes three different backscattering scenarios for this shell. For the uranyl acetate aqueous complex, the k-dependence indicates multiscattering interactions along the carboxylate group, suggesting formation of a bidentate complex. For uranyl glycolate, the k-dependence indicates an additional contribution from U atoms, suggesting a polynuclear, bidentate complex. For uranyl formiate, however, a strong splitting in both U-U and U-C paths may be interpreted as a combination of both uranyl formiate and hydrolysis species.

In the second example, we investigate the EXAFS spectra of aqueous uranyl carbonate complexes. Here, wavelet analysis can be used to discriminate the multiscattering resonances U-C-O in the equatorial uranyl plane from the single scattering path of the alkaline cations Sr or Ba at ~4.15 Å.

Third, using a spectrum of Zn-Al layered double hydroxide, we discriminate Al and Zn at a similar crystallographic position, in spite of destructive interference substantially reducing signal information. We discriminate not only the single scattering paths at ~3 Å, but also the focused multiple scattering paths at ~6 Å. Using this latter example, we demonstrate that high elemental (k-space) resolution and a high distance (r-space) resolution cannot be achieved simultaneously.

STRUCTURE OF A PLUTONIUM/SEQUESTERING AGENT COMPLEX BY SYNCHROTRON X-RAY DIFFRACTION

A.E.V. Gorden, D.K. Shuh, B.E.F. Tiedemann, K.N. Raymond
The Glenn T. Seaborg Center, Chemical Sciences Division
Lawrence Berkeley National Laboratory, Berkeley, CA and
Department of Chemistry, University of California, Berkeley, CA 94720

Abstract

Less than 25 plutonium complexes have been characterised by single-crystal X-ray diffraction and reported in the literature. A detailed evaluation of the structure and bonding of actinide co-ordinating ligands is important if new synthetic chelating ligands are to be designed for their selective co-ordination. Anticipating the small size of Pu crystals resulting from ligand systems of interest and handling considerations, we have developed procedures that utilise a system developed for structure determination of very small single crystals to use the Advanced Light Source (ALS) synchrotron to determine the solid-state structures of Pu complexes by X-ray diffraction (XRD). Using these methods, the Pu(IV)-[5LIO(Me-3,2-HOPO)]$_2$ complex is the first in a series of ligands to be characterised. This will aid in the generation of a library of such complexes on which to base the design of novel ligand systems and provides a benchmark for additional structural studies with actinides. This represents the first Pu(IV) hydroxypyridonate complex to be structurally characterised, the first Pu decorporation agent to be characterised by single crystal X-ray diffraction and the first Pu complex characterised through the use of a single crystal small molecule X-ray diffraction at a synchrotron radiation source.

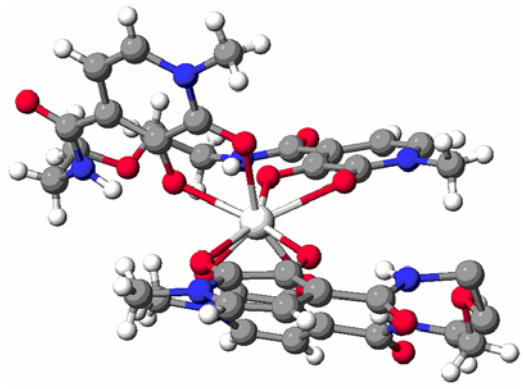

MICRO X-RAY ABSORPTION SPECTROSCOPY FOR ENVIRONMENTAL AND MATERIALS SCIENCE AT BEAMLINE 10.3.2

M.A. Marcus, A.A. MacDowell, R. Celestre, E. Domning,
A.A. Manceau, G. Morrison, H.A. Padmore, T. Miller
Advanced Light Source Division, MS2R0400, One Cyclotron Road,
Lawrence Berkeley National Laboratory, Berkeley, CA 94720 USA

Abstract

Beamline 10.3.2 at the ALS is a bend magnet line designed mostly for work on environmental problems involving heavy metal speciation and location. It offers a unique combination of X-ray fluorescence mapping, X-ray microspectroscopy and micro X-ray diffraction. The optics allow the user to trade spot size for flux in a size range of 5-17 m in an energy range of 3-17 keV. The focusing is done using a Kirkpatrick-Baez mirror pair to image a variable-size virtual source onto the sample. Thus, the user can reduce the effective size of the source, thereby reducing the spot size on the sample, at the cost of flux. This decoupling from the actual source also allows for some independence from source motion. The X-ray fluorescence mapping is done with a continuously scanning stage which avoids the time overhead incurred by step-and-repeat mapping schemes. The beamline layout and a science example are shown.

STRUCTURAL AND ELECTRONIC PROPERTIES OF $A_2Ti_2O_7$ (A=Sm, Gd, Ho AND Yb) PYROCHLORES FOLLOWING ION-BEAM IRRADIATION: A Ti 2p AND O 1s NEXAFS STUDY

P. Nachimuthu[1,2], S. Thevuthasan[3], W.J. Weber[3], V. Shutthanandan[3], Y. Zhang[3], D.K. Shuh[2], D.W. Lindle[1], G. Balakrishnan[4], D.M. Paul[4], E.M. Gullikson[2], R.C.C. Perera[2]

[1]Department of Chemistry, University of Nevada, Las Vegas, NV 89154

[2]Lawrence Berkeley National Laboratory, Berkeley, CA 94720

[3]Pacific Northwest National Laboratory, Richland, WA 99352

[4]Department of Physics, University of Warwick, Coventry, UK

Abstract

Pyrochlore is one of several candidate materials proposed for the immobilisation of actinide-rich wastes including plutonium and also has several potential technological uses. The pyrochlores under consideration for waste immobilisation have $A_2B_2O_7$ stoichiometry; where actinides and lanthanides are incorporated in the A-site, and Ti or Zr occupy the B-site. Near-edge X-ray absorption fine structure (NEXAFS) investigations of $A_2Ti_2O_7$ (A=Sm, Gd, Ho and Yb) single crystals were carried out prior to and following 2.0 MeV Au^{2+} ion beam (dose ~5.0×10^{14} Au^{2+}/cm^2) irradiation. Prior to irradiation, Ti L-edge NEXAFS shows that Ti^{4+} ions in $A_2Ti_2O_7$ occupy octahedral sites with a tetragonal distortion induced by the vacant 8a oxygen sites located in the ab plane adjacent to TiO_6 octahedron. The magnitude of tetragonal distortion in the TiO_6 octahedron varies depending on the ionic radius of the A^{3+} cation. The difference in the distortion between the $A_2Ti_2O_7$ (A=Sm, Gd, Ho and Yb) pyrochlores allows the determination of the relative disorder, which influences the radiation tolerance and oxygen ion conductivity of these materials. Ion beam irradiation leads to a phase transformation from the ordered pyrochlore structure (*Fd*3*m*) to the defect fluorite structure (*Fm*3*m*) and eventually to the amorphisation of $A_2Ti_2O_7$ (A=Sm, Gd, Ho and Yb).

STRUCTURAL INVESTIGATION OF THE EXTRACTED COMPLEXES OF Am(III) AND Ln(III) WITH CYANEX301 BY EXAFS

Guoxin Tian[1,2], Yongjun Zhu[2], Linfeng Rao[1]
[1]Glenn T. Seaborg Center, Lawrence Berkeley National Laboratory, Berkeley, CA 94720
[2]Institute of Nuclear and New Energy Technology, Tsinghua University, Beijing 102201

Abstract

Cyanex301, a dithiophosphinic acid, selectively extracts trivalent actinides [e.g. Am(III)] over trivalent lanthanides (Ln(III)) in solvent extraction. To understand the underlying principle governing the selectivity, the structures of the extracted complexes of Am(III) and Ln(III) in organic solvent solutions were investigated using EXAFS. The data show that the structure of the Am(III) complex is different from that of the Ln(III) complexes. The co-ordination number of Ln(III) in the complexes is 8 (seven sulphur atoms from four Cyanex301 molecules and one oxygen atom from a water molecule), suggesting the Ln(III) complex with Cyanex301 has one H_2O molecule with a molecular formula of $HLnL_4 \bullet H_2O$, where L stands for the anion of Cyanex301. On the contrary, the Am(III) complex with Cyanex301 does not contain H_2O with the molecular formula of $HAmL_4$, in which only the eight sulphur atoms from Cyanex301 co-ordinated to Am(III). The results suggest that the high selectivity of Cyanex301 in the extraction of An(III) over Ln(III) arises from the difference in the hydration state of the extracted complexes and thus their affinity to the organic phase.

The co-ordination bond lengths in the extracted complexes are also determined by EXAFS. As the atomic number increases from La(III), through Nd(III) to Eu(III), the bond lengths of Ln-O and Ln-S gradually decrease: Ln-O, 2.70, 2.56 and 2.50 Å; Ln-S, 3.01, 2.91 and 2.84 Å. The average Ln-P distances are 3.60 (La), 3.53 (Nd) and 3.46 Å (Eu). In comparison, the bond length of Am-S is 2.98 Å, and the average Am-P distance is 3.58 Å.

INITIAL RESULTS FROM INVESTIGATIONS OF URANIUM MATERIALS BY SOFT X-RAY SCANNING X-RAY TRANSMISSION MICROSCOPY (STXM)

T. Tyliszczak, P. Nachimuthu, T. Warwick, D.K. Shuh
Lawrence Berkeley National Laboratory, University of California, Berkeley, CA 94720

Abstract

The emergence of microspectroscopic and fluorescence-based techniques has permitted investigations of actinide materials at sources of soft X-ray synchrotron radiation. The investigation of prototypical uranium oxide particulate materials in the scanning transmission X-ray microscope (STXM) of the ALS-Molecular Environmental Science Beamline 11.0.2 under ambient pressure has been a recent development. Particles have been examined at the U thresholds below 2 keV for uranium imaging and spatially-resolved NEXAFS spectroscopy. Oxygen K edge spectra from the uranium oxides has also been obtained by spectromicroscopy techniques and have been collected as a function of polarisation for UO_3. The future prospects and potential for actinide STXM investigations will be presented.

The ALS and this work are supported by the Director, Office of Science, Office of Basic Energy Sciences, Division of Materials Sciences and the Division of Chemical Sciences, Geosciences, and Biosciences of the US Department of Energy at Lawrence Berkeley National Laboratory under Contract No. DE-AC03-76SF00098.

VALIDATING MOLECULAR DYNAMICS OF RADIATION DAMAGE IN ZIRCON

Messaoud Harfouche[1,2]**, Jean-Paul Crocombette**[3]**, François Farges**[1,2,4]
[1]Laboratoire des Géomatériaux and URA CNRS 2455, Université de Marne la Vallée, France
[2]Swiss Light Source, Institut Paul Scherrer, Villigen, Switzerland
[3]DEN-DMN-SRMP, Commissariat a l'Énergie Atomique, Saclay, France
[4]Dept. of Geological and Environmental Sciences, Stanford University, USA

Abstract

X-ray absorption fine structure spectroscopy (XAFS) at the Zr and Si K-edges, as well as the U and Th-L_{III} edges has been performed on various metamict zircons from Sri Lanka and compared to the information obtained by molecular dynamics (MD) thanks to *ab initio* XAFS calculations. The (green) zircon samples from Sri Lanka show an intermediate to fully metamict structure to X-ray diffraction. Experimental information show a loss of medium range structure at both edges and a decrease in zirconium co-ordination from 8 to 7, while Si's tetrahedral coordination is preserved. Despite the fact that this model implies a polymerisation of the Si network [1], we found that the previously reported shift in the Si K-edge as a function of polymerisation [2] could not be reproduced here, making it an impossibility to conclude on that aspect based on the Si K-edge information. Tetravalent actinides remain 8-co-ordinated, even in the metamict state [3]. In addition, the local structure around these actinides shows a significant distortion in the medium range structure, especially Th (when replacing Zr).

Molecular dynamics simulations [4] are in agreement with such observations. A bond valence analysis of the MD models, previously confirmed, was suitable for reliable self-consistent *ab initio* XAFS calculations (using FEFF8). The average calculated *ab initio* XAFS spectra match the experimental spectra of the metamict zircons from Sri Lanka surprisingly well. For instance, the Fourier Transforms of the Zr K-edge experiment and the simulation are quite identical. Also, the MD information for U in these simulations confirms the presence of a structural relaxation in the medium range environment of U to accommodate itself in the Zr site, as observed in the experiment.

Therefore, combining MD to XAFS is a useful tool to ascertain not only the pair potentials used in MD but also the way the cascade is simulated. On the other hand, MD brings a powerful outlook to the local structures probed by XAFS and shed light on the effect on disorder effects, among others, on the XAFS spectra.

REFERENCES

[1] Farges, F., "The Structure of Metamict Zircon: A Temperature-dependant EXAFS Study", *Physics and Chemistry of Minerals*, 20, 504-514 (1994).

[2] Li, *et al*. (1996).

[3] Farges, F., M. Harfouche, P-E. Petit, G.E. Brown, Jr., "Actinides in Earth Materials: The Importance of Natural Analogs", *2nd Euroconference/NEA Workshop on Speciation, Techniques, and Facilities for Radioactive Materials at Synchrotron Light Sources*, ESRF, Grenoble, Sept. 2000.

[4] Crocombette, J.P. and D. Ghaleb, "Modeling the Structure of Zircon ($ZrSiO_4$): Empirical Potentials, Ab-initio Electronic Structure", *Journal of Nuclear Materials*, 257, 282-286 (1998).

TETRAVALENT ACTINIDES IN HIGH PRESSURE/ HIGH TEMPERATURE GLASSES AND MELTS

Manuela Borchet[1], **Max Wilke**[1], **Christian Schmidt**[2], **François Farges**[3], **Alexandre Simionovici**[4]
[1]Institut fuer Geowissenschaften, Potsdam Universitaet, Germany
[2]GeoForschungsZentrum Potsdam, Germany
[3] Laboratoire des Géomatériaux, Université de Marne la Vallée, Marne la Vallée, France and Department of Geological and Environmental Sciences, Stanford University, USA
[4] ESRF, Grenoble, France and Laboratoire des Sciences de la Terre, ENS, Lyon, France

Abstract

In order to understand the geochemical properties of actinides in molten silicates that are the closest as possible to "real magmas", diamond anvil cells (DAC) are used to confine hydrous silicate melts under "high" pressure and temperatures (to 900°C and 10 kbars). The use of focused X-ray beam on third-generation synchrotron sources (such as available on ID22 at ESRF, Grenoble, France) makes possible the collection of the first *in situ* high P/T spectroscopy information on actinides in silicate melts exposed to extreme conditions, aimed to be close to these prevailing in magmatic chambers before eruptions.

Two sets of compositions were studied: sodium trisilicate (Na_2O-$3SiO_2$) and an haplorhyolite ($\sim(NaAlSi_3O_8)_{47}(KAlSi_3O_8)_{21}(SiO_2)_{32}$), doped with 1-3 wt.% of Th(IV) and U(VI). Initially, U was dissolved in the glass in air so the main form of U was originally uranyl. After a quick confinement inside the DAC, U is quickly reduced to U(IV) (because of the use of a reducing hydrogen-bearing (1-5%) nitrogen mixture to prevent the graphitisation of the diamonds at elevated temperatures). Indeed, a ~4 eV shift of the uranium L_{III} edge position was systematically observed above Tg. Redox apart, there is no drastic change in the local structure around tetravalent actinides in the NS3 melt, as compared to the relaxed anhydrous counterparts. In the U-bearing AOQ composition, however, uranium quickly precipitates as UO_2 in the melt. This result is consistent with earlier synthesis attempts using an albitic composition (Na_2O-Al_2O_3-$3SiO_2$ also with 1 wt.% U) under reduced oxygen fugacity conditions, which resulted in the nucleation of UO_2 in the quenched glass (resulting in an opaque, brownish-coloured glass). Surprisingly, the Th-bearing AOQ composition do not show any evidence of ThO_2 nucleation (nor the albitic glasses) but show a speciation around Th that is similar to that measured *in situ* in the high pressure/high temperature NS3 melt. Such an environment is typical of 7-co-ordinated Th, as found in natural titanite recently (see Farges, *et al*., these proceedings). Consequently, if tetravalent actinides are not highly sensitive to the presence of dissolved water, pressure (1 bar-8 kbars range) and temperature (20-700°C, including melting), U(IV) shows a much greater sensitivity to melt polymerisation than Th(IV). Finally, the water/melt partitioning has been studied and we found, in contrast to what expected, that U does not partition strongly onto the coexisting super-critical water but remains in the melt phase.

Ti, Cr, REEs IN BOROSILICATE MELTS: COMPARISON WITH QUENCHED GLASSES

François Farges[1,2], **Gordon E. Brown, Jr.**[2,3]
[1]Laboratoire des Géomatériaux, Université de Marne la Vallée, FRE CNRS 2455
Marne la Vallée, France
[2]Department of Geological and Environmental Sciences, Stanford University, USA
[3]Stanford Synchrotron Radiation Laboratory, Menlo Park, USA

Abstract

The local environments around Ti, Cr and several light rare-earth elements (Ce, Nd, La and Pr) was examined in a number of complex borosilicate glasses that were synthesised at Pacific Northwest National Laboratories as analogues of waste-form glasses that are candidates for the long-term storage of Pu and other trivalent transuranic elements. In these glasses, Ce is used as a surrogate for Pu. We have also used EXAFS to study a waste-form glass that mimics the R7T7 composition (i.e. the 27-oxide composition except artificial actinides) used in France for nuclear waste storage. Highly charged cations such as Ti, Cr and REEs are suspected to enhance nucleation in their host glasses which must be minimised for safe disposal of transuranic elements over thousands of years.

We have studied Ti, Cr and REE cations in these glass samples at temperatures up to 1 500 K to determine if the melt structure undergoes rearrangement prior to quenching to a glass. *In situ* X-ray absorption fine structure (XAFS) spectroscopy experiments were performed to 1 250°C. We used a heating loop modified to collect XAFS spectra *in situ* to 1 300°C [1]. Experiments were performed in air. Ti and Cr K-edge XAFS data was collected on the 4-3 beamline, whereas that for REEs was collected at their L_3 edges. Because of the large overlapping in energies between the K and L_3 edges, only X-ray absorption fine structure (XANES) data was collected [2].

Examination of the high-resolution XANES spectra for Ti shows a significant co-ordination change of Ti (from ~5 to ~4.5), which was not observed on pure silicate glass/melts systems [1] exposed to similar conditions. However, a loss of a feature in the main edge crest can also be observed, which we attributed to the higher motions of network modifiers third neighbours above melting. A similar process was also observed around Cr, which remains trivalent and octahedrally co-ordinated (although quite distorted as compared to ruby and emerald model compounds) in the melt. No evidence of other redox states of Cr could be evidenced in the melts. In contrast, Ce changes drastically its redox from IV to III upon melting and the process is reversible. La and Pr seem much less affected by melting. Nd shows intriguing new features in the melt that are not observed in the melt. This local structure information around these highly charged cations provides, not only the first direct *in situ* speciation measurements around these cations in melts, but also can be compared to that obtained for silicate systems.

REFERENCES

[1] Farges, F., G.E. Brown, Jr., A. Navrotsky, H. Gan and J.J. Rehr, "Coordination Chemistry of Ti(IV) in Silicate Glasses and Melts. III. Glasses and Melts Between 293 and 1650 K", *Geochimica and Cosmochimica Acta*, 60, 3055-3065 (1996).

[2] Farges, F., G.E. Brown, Jr., "In-situ, High-temperature XAFS Studies of the Coordination Chemistry of High-valent Cations in Molten Silicates", *1997 SSRL Activity Report* (Proposal #2336Mp) (1997).

ON THE CO-ORDINATION OF TETRAVALENT ACTINIDES IN SILICATE GLASSES AND MELTS: THE "TITANITE" VIEW

François Farges[1-3], **Messaoud Harfouche**[1,2], **Manuel Munoz**[1,4], **Max Wilke**[4], **Gordon E. Brown, Jr.**[3,5]
[1]Laboratoire des Géomatériaux and URA CNRS 2455, Université de Marne la Vallée, France
[2]Swiss Light Source, Institut Paul Scherrer, Villigen, Switzerland
[3]Dept. of Geological and Environmental Sciences, Stanford University, USA
[4]Université de Grenoble, France
[5]Institut fuer Geowissenschaften, Potsdam Universitaet, Germany
[6]Stanford Synchrotron Research Laboratory, Menlo Park, USA

Abstract

The local structure around 0.05-1 wt.% Th and U in various silicate glasses and melts was examined thanks to X-ray absorption fine structure spectroscopy at the L_{III} edges. Silicate glasses include fully polymerised anhydrous and hydrous glasses (up to 6 wt.% water dissolved). They were synthesised up to 6 kbars pressure at 1 000°C in an internally heated high-pressure vessel (Institut für Geowissenschaft, Hannover, Germany). X-ray absorption fine structure experiments were performed *in situ* from 290 to 1 250 K and at 1 bar air pressure. We used a modified version of the heating loop furnace to work in the fluorescence mode. Data was collected on the 4-3 and 11-2 beamlines at SSRL (Stanford, USA) with Si(220) double-crystals monochromators.

The spectra for U(VI) shows the reminiscence of uranyl moieties in the melt. No changes in composition, melt polymerisation can be observed, suggesting that the glass is a good picture of the *in situ* melt. The same conclusions were reached for Th(IV). However, in agreement with previous past studies on Th in melt, the average Th-O distance (~ 2.36 Å) is "in-between" that for 6- and 8-co-ordinated Th. Despite disorder effects were accounted for, such average shorter Th-O distance suggests that the average Th co-ordination in most silicate glasses is 7 on the average. To decipher between a mixing model (i.e. 6-co-ordinated and 8-co-ordinated Th in half-and-half proportions) and the presence of 7-co-ordinated moieties in glass and melts around Th, special attention was given to titanite ($CaTiSi_2O_5$). In nature, titanite often contains significant amounts of Th (up to 5 000 ppm). The analysis of the Th XAFS-L_{III} edge in various natural, non-metamict titanites clearly indicates that Th substitutes for Ca, which is 7-co-ordinated in that structure. The average Th-O distance in titanite is 2.36-2.37 Å. Therefore, we suggest that 7-co-ordinated environments exist around natural tetravalent actinides such as Th. The local structure around Th in these titanites is very close to that found in silicate glasses and melts, and because no evidence of site mixing is found, we also propose that Th(IV) occurs in glasses and melts as 7-coordinated environments, as in Th-bearing natural titanite. This model would explain why titanites are always enriched in Th than U in nature. Consequently, the ionic radius usually used for modelling Th(IV) in melts to predict chemical properties should be reconsidered to a significantly lower values. Also, Th makes bonds in the glass and the melt that are stronger than previously taught, making it less sensitive to thermal expansion or chemically more durable.

Appendix 1

ORGANISING COMMITTEE

Organising Committee

J. Bargar (USA)
G. Bernhard (Germany)
G.E. Brown, Jr. (USA)
S. Lequien (France)
T. Reich (Germany)
A. Scheinost (Germany)
D.K. Shuh (USA)
E. Simoni (France)
L. Soderholm (USA)
C. Nordborg (France)

International Scientific Committee

P.G. Allen (USA)
J. Bargar (USA)
G. Bernhard (Germany)
G.E. Brown, Jr. (USA)
C.H. Booth (USA)
D.L. Clark (USA)
S.D. Conradson (USA)
C. Den Auwer (France)
M.A. Denecke (Germany)
N.M. Edelstein (USA)
I. Grenthe (Sweden)
G. Kaindl (Germany)
K. Kemner (USA)
T. Fanghänel (Germany)
D.I. Kochubey (Russia)
G.H. Lander (Germany)
S. Lequien (France)
F. Livens (UK)
C. Madic (France)
H. Nitsche (USA)
T. Reich (Germany)
A.M. Scheidegger (Switzerland)
A. Scheinost (Germany)
L. Soderholm (USA)
D.K. Shuh (USA)
B. Sitaud (France)
E. Simoni (France)
J. Tobin (USA)
T. Yaita (Japan)
Z. Yoshida (Japan)

Appendix 2

LIST OF PARTICIPANTS

FRANCE

Dr. Christophe DEN AUWER
CEA Marcoule
DEN/DRCP/SCPS/LCAM
Atalante
F-30207 Bagnols-sur-Cèze Cedex

Tel: +33-466796253
Fax: +33-466796325
Eml: christophe.denauwer@cea.fr

Dr. Stephane LEQUIEN
LPS UMR 9956 CEA-CNRS
CEA/Saclay
F-91191 Gif-sur-Yvette Cedex

Tel: +33-169082848
Fax: +33-169086923
Eml: stephane.lequien@cea.fr

Dr. Bruno SITAUD
Synchroton SOLEIL
L'Orme des Merisiers
Saint-Aubin – BP 48
F-91192 Gif-sur-Yvette Cedex

Tel: +33-169359622
Fax: +33-169359456
Eml: bruno.sitaud@synchrotron-soleil.fr

GERMANY

Dr. Melissa A. DENECKE
Forschungszentrum Karlsruhe
Institute for Nuclear Waste Management
P.O. Box 3640
D-76021 Karlsruhe

Tel: +49-7247-82-5536
Fax: +49-7247-82-3927
Eml: melissa@ine.fzk.de

Prof. Thomas FANGHÄNEL
Forschungszentrum Karlsruhe
Institute for Nuclear Waste Management
P.O. Box 3640
D-76021 Karlsruhe

Tel: +49-7247-82-2230
Fax: +49-7247-82-4308
Eml: fanghaenel@ine.fzk.de

Dr. Harald FUNKE
Forschungszentrum Rossendorf
CRG-ROBL
ESRF Sector 21
BP 220
F-38043 Grenoble Cedex, France

Tel: +33-476882339
Fax: +33-476882505
Eml: funke@esrf.fr

Dr. Christoph HENNIG
Forschungszentrum Rossendorf
ROBL-CRG
ESRF Sector 21
BP 220
F-38043 Grenoble Cedex, France
Tel: +33-476882005
Fax: +33-476882505
Eml: hennig@esrf.fr

Prof. Tobias REICH
Johannes Gutenberg-Universität Mainz
Institute of Nuclear Chemistry
Fritz-Strassmann-Weg 2
D-55128 Mainz
Tel: +49-61313925250
Fax: +49-61313924510
Eml: tobias.reich@uni-mainz.de

Dr. André ROSSBERG
Forschungszentrum Rossendorf
ROBL-CRG
ESRF Sector 21
BP 220
F-38043 Grenoble Cedex, France
Tel: +49-476882847
Fax: +33-476882505
Eml: rossberg@esrf.fr

Dr. Andreas C. SCHEINOST
Forschungszentrum Rossendorf
CRG-ROBL
ESRF Sector 21
BP 220
F-38043 Grenoble Cedex, France
Tel: +33-476882463
Fax: +33-476882505
Eml: scheinost@esrf.fr

Dr. Eugen WESCHKE
Freie Universität Berlin
Institut für Experimentalphysik
Arnimallee 14
D-14195 Berlin
Tel: +49-30-838-56161
Fax: +49-30-838-56560
Eml: eugen.weschke@physik.fu-berlin.de

JAPAN

Atsushi IKEDA
Research Lab. for Nuclear Reactors
Tokyo Institute of Technology
2-12-1, O-okayama
Meguro-ku, Tokyo 152-8550
Tel: +81-29-282-5167
Fax: +81-29-282-6723
Eml: aikeda@nr.titech.ac.jp

Hideaki SHIWAKU
Synchrotron Radiation Research Center
Japan Atomic Energy Research Institute
Mikazuki-cho, Sayo-gun
Hyogo 679-5148
Tel: +81-791-58-2701
Fax: +81-791-58-2740
Eml: shiwaku@spring8.or.jp

Dr. Tsuyoshi YAITA
Japan Atomic Energy Research Institute
Department of Materials Science
Tel: +81-29-282-5167
Fax: +81-29-282-6723
Eml: yaita@mummy.tokai.jaeri.go.jp

RUSSIAN FEDERATION

Dr. Kirill E. IVANOV
Russian Research Centre
"Kurchatov Institute"
I.V. Kurchatov Square 1
123182 Moscow

Tel: +7-095-196-9252
Fax: +7-095-882-5804
Eml: ivanov@ignph.kiae.ru

SWEDEN

Prof. Gunnar SKARNEMARK
Chalmers University of Technology
Department of Nuclear Chemistry
S-41296 Göteborg

Tel: +46-707535034
Fax: +46-317722931
Eml: Gunnar.skarnemark@chem.chalmers.se

SWITZERLAND

Dr. Rainer DÄHN
Paul Scherrer Institut
Laboratory for Waste Management
CH-5232 Villigen PSI

Tel: +41-56-310-2175
Fax: +41-56-310-2821
Eml: rainer.daehn@psi.ch

Marika VESPA
Paul Scherrer Institut
Laboratory for Waste Management
CH-5232 Villigen PSI

Tel: +41-563102966
Fax: +41-563102821
Eml: marika.vespa@psi.ch

UNITED KINGDOM

Prof. Robert G. DENNING
University of Oxford
Inorganic Chemistry
South Parks Road, OX1 3QR

Tel: +44-1865-272631
Fax: +44-1865-272690
Eml: bob.denning@chem.ox.ac.uk

UNITED STATES OF AMERICA

Dr. Patrick ALLEN
Lawrence Livermore National Laboratory
P.O. Box 808
Livermore, CA 94551

Tel: (925) 423-8955
Fax: (925) 423-0372
Eml: allen42@llnl.gov

Dr. John BARGAR
SSRL MS 69
SLAC
2575 Sand Hill Road
Menlo Park, CA 94025

Tel: (650) 926-4949
Fax: (650) 926-3600
Eml: bargar@slac.stanford.edu

Dr. Corwin BOOTH
Lawrence Berkeley National Laboratory
MS 70A1150
One Cyclotron Road
Berkeley, CA 94720
Tel: (510) 486-6079
Fax: (510) 486-5596
Eml: CHBooth@lbl.gov

Prof. Gordon BROWN, Jr.
Dept. of Geological and Env. Sciences
Stanford University
Stanford, CA 94305-2115
Tel: (650) 723-9168
Fax: (650) 725-2199
Eml: Gordon@pangea.stanford.edu

Kathleen BROWER
Lawrence Berkeley National Laboratory
MS 939R0200
One Cyclotron Road
Berkeley, CA 94720
Tel: (510) 486-6386
Fax: (510) 486-7752
Eml: KHBrower@lbl.gov

Jerome BUCHER
Lawrence Berkeley National Laboratory
MS 70A1150
One Cyclotron Road
Berkeley, CA 94720
Tel: (510) 486-7167
Fax: (510) 486-5596
Eml: JJBucher@lbl.gov

Patricia BUTLER
Lawrence Berkeley National Laboratory
MS 939R0200
One Cyclotron Road
Berkeley, CA 94720
Tel: (510) 486-5984
Fax: (510) 486-7752
Eml: PAButler@lbl.gov

Jeff CATALANO
Dept. of Geological and Env. Sciences
Stanford University
Stanford, CA 94305-2115
Tel: (650) 723-7513
Fax: (650) 725-2199
Eml: catalano@pangea.stanford.edu

Dr. Steve CONRADSON
Los Alamos National Laboratory
P.O. Box 1663
Los Alamos, NM 87545
Tel: (505) 667-9584
Fax: (505) 667-8021
Eml: conradson@lanl.gov

Dr. Million DANIEL
Lawrence Berkeley National Laboratory
MS 70A1150
One Cyclotron Road
Berkeley, CA 94720
Tel: (510) 486-5377
Fax: (510) 486-5596
Eml: DMillion@lbl.gov

Lynne DORY
Lawrence Berkeley National Laboratory
MS 70A1150
One Cyclotron Road
Berkeley, CA 94720
Tel: (510) 486-5587
Fax: (510) 486-5596
Eml: LADory@lbl.gov

Norman EDELSTEIN
Lawrence Berkeley National Laboratory
MS 70A1150
One Cyclotron Road
Berkeley, CA 94720
Tel: (510) 486-5624
Fax: (510) 486-5596
Eml: NMEdelstein@lbl.gov

Dr. Anne E. V. GORDEN
UCB/LBNL
MS 70A1150
One Cyclotron Road
Berkeley, CA 94720
Tel: (510) 642-2516
Fax. (510) 486-5283
Eml: agorden@uclink.berkeley.edu

DR. Huijian JIANG
Lawrence Berkeley National Laboratory
MS 70A1150
One Cyclotron Road
Berkeley, CA 94720
Tel: (510) 486-5141
Fax: (510) 486-5596
Eml: HJiang@lbl.gov

Dr. Shelly KELLY
Environmental Research Division
Argonne National Laboratory
Argonne, IL 60439
Tel: (630) 252-7376
Fax: (630) 252-9793
Eml: skelly@anl.gov

Dr. Kenneth KEMNER
Environmental Research Division
Argonne National Laboratory
Argonne, IL 60439
Tel: (630) 252-1163
Fax: (630) 252-9793
Eml: kemner@anl.gov

Dr. Wayne LUKENS
Lawrence Berkeley National Laboratory
MS 70A1150
One Cyclotron Road
Berkeley, CA 94720
Tel: (510) 486-4305
Fax: (510) 486-5596
Eml: WWLukens@lbl.gov

Dr. Matthew MARCUS
Lawrence Berkeley National Laboratory
MS 2R0400
One Cyclotron Road
Berkeley, CA 94720
Tel: (510) 486-7604
Fax: (510) 486-7696
Eml: MAMarcus@lbl.gov

Dr. Ponnusamy NACHMUTHU
Lawrence Berkeley National Laboratory
MS 2R0400
One Cyclotron Road
Berkeley, CA 94720
Tel: (510) 486.5377
Fax: (510)486-4550
Eml: PNachimuthu@lbl.gov

Dr. Erik NELSON
Lawrence Livermore National Laboratory
P.O. Box 808
Livermore, CA 94551
Tel: (925) 422.2186
Fax: (925)423-0372
Eml: nelson87@llnl.gov

Dr. Hans NILSSON
SKB/LBNL
MS 70A1150
One Cyclotron Road
Berkeley, CA 94720
Tel: (510) 486-6612
Fax: (510) 486-5596
Eml: HJNilsson@lbl.gov

Prof. Heino NITSCHE
UCB/LBNL
MS 70R0319
One Cyclotron Road
Berkeley, CA 94720
Tel: (510) 486-5615
Fax: (510) 486-7444
Eml: hnitsche@lbl.gov

Dr. Wendy REED
Lawrence Berkeley National Laboratory
MS 70A1150
One Cyclotron Road
Berkeley, CA 94720
Tel: (510) 486-6612
Fax: (510) 486-5596
Eml: WAReed@lbl.gov

Prof. Richard REEDER
Dept. of Geoscience
SUNY, Stony Brook
Stony Brook NY 11794
Tel: (631) 632-8208
Fax: (631) 632.8240
Eml: rjreeder@notes.cc.sunysb.edu

Joe ROGERS
SSRL
SLAC
2575 Sand Hill Road
Menlo Park, CA 94025
Tel: (650) 926-3088
Fax: (650) 926-3600
Eml: JRogers@slac.stanford.edu

Dr. David SHUH
Lawrence Berkeley National Laboratory
MS 70A1150
One Cyclotron Road
Berkeley, CA 94720
Tel: (510) 486-6937
Fax: (510) 486-5596
Eml: DKShuh@lbl.gov

Dr. Lynda SODERHOLM
Chemistry Division
Argonne National Laboratory
Argonne, IL 60439
Tel: (630) 252-4364
Fax: (630) 252-9289
Eml: LS@anl.gov

Dr. Guoxin TIAN
Lawrence Berkeley National Laboratory
MS 70A1150
One Cyclotron Road
Berkeley, CA 94720
Tel: (510) 486-5141
Fax: (510) 486-5596
Eml: gtian@lbl.gov

Dr. James TOBIN
Lawrence Livermore National Laboratory
P.O. Box 808
Livermore, CA 94551
Tel: (925) 422-7247
Fax: (925) 423-7040
Eml: Tobin1@llnl.gov

Dr. Tolek TYLISZCZAK
Lawrence Berkeley National Laboratory
MS 6-200
One Cyclotron Road
Berkeley, CA 94720

Tel: (510) 486-5188
Fax: (510) 495-2067
Eml: TTyliszczak@lbl.gov

Dr. Glenn WAYCHUNAS
Lawrence Berkeley National Laboratory
MS 70-0120
One Cyclotron Road
Berkeley, CA 94720

Tel: (510) 495-2224
Fax: (510) 486-7152
Eml: gawaychunas@lbl.gov

Richard WILSON
Lawrence Berkeley National Laboratory
MS 70A1150
One Cyclotron Road
Berkeley, CA 94720

Tel: (510) 486-5561
Fax: (510) 486-7444
Eml: REWilson@lbl.gov

Dr. Joseph WONG
Lawrence Livermore National Laboratory
P.O. Box 808
Livermore, CA 94551

Tel: (925) 423-6305
Fax: (925) 424-4737
Eml: wong10@llnl.gov

OECD PUBLICATIONS, 2 rue André-Pascal, 75775 PARIS CEDEX 16
Printed in France.